2022年度　学位論文

Study on QGP bulk property based on relativistic resistive magneto-hydrodynamics

(相対論的電磁流体に基づくクォーク・グルーオンプラズマの物性研究)

名古屋大学大学院理学研究科
素粒子宇宙物理学専攻

学籍番号 462001086

中村幸輝

2022年12月07日

Abstract

The protons and neutrons consist of quarks and gluons which are the elementary particles in the standard model. The strong interaction between quarks and gluons is described by quantum chromodynamics (QCD). In our living energy scale, the quarks and gluons are confined in hadrons such as protons, neutrons, and π mesons. However, under extreme condition such as high temperature and/or density, quarks and gluons are deconfined from hadrons, and form the quark-gluon plasma (QGP) phase, due to the property of the QCD, asymptotic freedom.

For production of the QGP on the earth, a series of high-energy heavy-ion collisions have been performed. In 2000 at Relativestic Heavy Ion Collider (RHIC) at Brookhaven National Laboratory high-energy heavy-ion collisions started. At that time only relativistic hydrodynamic model succeeded in explaining strong elliptic flow. The success of relativistic hydrodynamics reached the conclusion that the QGP created at RHIC is not weakly interacting gas but strongly interacting plasma. Thus, the present target of high-energy heavy-ion collisions is the quantitative understanding of QGP bulk properties, which is advanced from the search for the existence of QGP.

Furthermore, the production of ultraintense electromagnetic fields in high-energy heavy-ion collisions has come into spotlight. In fact, the highest intensity of the magnetic fields in our universe may be reached. For example, the value of the magnetic fields becomes $|eB| \sim 10^{15}$ T at $\sqrt{s_{\rm NN}} = 200$ GeV Au-Au collisions. The study of the interaction between the QGP and ultraintense electromagnetic fields can address to electric and magnetic transport properties of QGP.

In this thesis, we consider relativistic resistive magneto-hydrodynamics (RRMHD) as a description of the dynamics of the QGP coupling with electromagnetic fields. We develop a numerical simulation code of RRMHD for analysis of high-energy heavy-ion collisions. The verification of our numerical code is performed in several benchmark tests not only in the Cartesian coordinates but also in the Milne coordinates which are suitable for description of high-energy heavy-ion collisions.

Next we apply our developed RRMHD model to analysis on high-energy heavy-ion collisions at RHIC. In particular, we focus on the collective flow of charged hadrons. We discuss the electrical conductivity dependence of the collective flow in Au-Au and Cu-Au collisions. We confirm that the dissipation associated with Ohm's law plays an important role in the directed flow of hadrons in the Cu-Au collision systems. Furthermore, we find that the charge-dependent anisotropic flow is sensitive to the initial electromagnetic fields and electrical conductivity of the medium. The charge-dependent directed and elliptic flows are approximately proportional to electrical conductivity of the QGP. We conclude that the charge-dependent anisotropic flow is a good probe of the initial electromagnetic fields and electrical conductivity of the QGP.

Contents

1 Introduction **1**
- 1.1 Quantum chromodynamics and nuclear matter . . . 1
  - 1.1.1 QCD phase diagram . . . 2
- 1.2 High-energy heavy-ion collisions . . . 3
- 1.3 Outline of this Thesis . . . 6

2 High-Energy Heavy-Ion Collisions **7**
- 2.1 Phenomenology of high-energy heavy-ion collisions . . . 7
  - 2.1.1 Kinematics . . . 7
  - 2.1.2 Collision geometry . . . 8
  - 2.1.3 Particle production and anisotropic flow . . . 10
- 2.2 The standard description of dynamics in collision process . . . 13
  - 2.2.1 Initialization models . . . 14
  - 2.2.2 Hydrodynamic expansion . . . 15
  - 2.2.3 Hadronization . . . 15
  - 2.2.4 Hadronic cascades . . . 16

3 Erectromagnetic fields in Heavy-Ion Collisions **17**
- 3.1 Computation of electromagnetic field . . . 17
  - 3.1.1 Collision energy dependence . . . 18
- 3.2 Evolution of electromagnetic field . . . 19
  - 3.2.1 Pre-equilibrium stage evolution . . . 19
  - 3.2.2 Equilibrium-stage evolution . . . 20

4 Relativistic Hydrodynamics **23**
- 4.1 Relativistic hydrodynamic equations . . . 23
  - 4.1.1 local rest frame . . . 23
  - 4.1.2 Tensor decomposition . . . 24
- 4.2 Relativistic ideal hydrodynamics . . . 27
  - 4.2.1 Relativistic hydrodynamic equation in the Milne coordinates . . . 28
  - 4.2.2 Bjorken flow in high-energy heavy-ion collisions . . . 29

5 Relativistic Resistive Magneto-Hydrodynamics **31**
- 5.1 Basic equations . . . 31
- 5.2 Magnetized Bjorken flow . . . 32
- 5.3 The longitudinal expansion with acceleration in relativistic resistive magneto-hydrodynamics . . . 33

6 Numerical procedure **39**
6.1 Metric . . . 39
6.2 Constraint equations . . . 39
6.3 Basic equations . . . 40
6.4 Stiff part . . . 42
6.5 Primitive recovery . . . 42
6.6 Numerical algorithm . . . 43

7 Test problem **44**
7.1 Shock tube test problem . . . 44
7.2 Large amplitude circularly polarized Alfvén wave . . . 45
7.3 Self-similar current sheet . . . 46
7.4 Cylindrical explosion . . . 47
7.5 Rotor test . . . 48
7.5.1 Minkowski coordinates . . . 49
7.5.2 Milne coordinates . . . 50
7.6 Magnetized Bjorken flow . . . 51
7.7 Accelerating longitudinal expansion . . . 52
7.8 Short summary . . . 56

8 Application to Heavy-Ion collsions **57**
8.1 Initial conditions . . . 57
8.1.1 medium . . . 57
8.1.2 The initial electromagnetic field . . . 60

9 Numerical results **64**
9.1 Relativistic resistive magneto-hydrodynamic expansion . . . 64
9.1.1 Fluid velocity . . . 64
9.1.2 Dissipation measure . . . 66
9.1.3 The freezeout hypersurface . . . 67
9.2 The elliptic flow . . . 68
9.3 The directed flow . . . 69
9.4 Charge-dependent flow . . . 71
9.4.1 Charge distribution on the freezeout hypersurface . . . 71
9.4.2 The velocity profile of the freezeout hypersurface . . . 73
9.4.3 The charge-dependent elliptic flow . . . 74
9.4.4 The charge-dependent directed flow . . . 75

10 Summary **79**

Chapter 1

Introduction

This thesis aims to study the impact of electromagnetic response of quark-gluon plasma (QGP) in high-energy heavy-ion collisions. The investigation of electromagnetic response to physical observables can access the QGP bulk properties such as electrical conductivity. In this chapter, we introduce the basics of quantum chromodynamics which describes the dynamics of quarks and gluons in Sec. 1.1, and recent topics in high-energy heavy-ion collisions in Sec. 1.2. The outline of this thesis is shown in Sec. 1.3.

1.1 Quantum chromodynamics and nuclear matter

Quarks and gluons are elementary particles constituting the nucleons such as neutrons and protons. The dynamics of the quarks and gluons follow the theory of strong interactions described by quantum chromodynamics (QCD). In the standard model, the QCD is explained by a non-Abelian gauge theory with SU(3) group [1–3]. According to the QCD, quarks are fermions with color charge. The color charges have three degrees of freedom which are called red, green, and blue based on the analogy of the primary colors of human visual perception. The gluons are gauge bosons that intermediate the strong force between particles with color charge. The quarks also have flavor degrees of freedom and there are six quarks with different flavors: Up, down, and strange quarks are called as the light flavor quarks, and charm, bottom, and top quarks are called as the heavy flavor quarks. The net quark number which is difference of the number of quarks and anti-quarks of each flavor is conserved in the strong interactions.

However, in nature, the particles must have neutral color charges. In the low energy scale, the quarks and gluons are confined in color-neutral compound particles, known as hadrons. Then, quarks and gluons can not be detected solely. There are mainly two color-neutral hadrons: Meson composed of a quark and anti-quark, and baryon composed of three quarks of different color charges. The baryon number is conserved in the interactions among the hadrons due to the net quark number being conserved. The baryon chemical potential, namely the chemical potential associated with the baryon numbers, dictates the net number density of the quarks in the thermal equilibrium state. On the other hand, on a high-energy scale, the QCD predicts that quarks and gluons are deconfined from hadrons at high temperature or/and baryon density. It is caused by asymptotic freedom as the important characteristic feature of

the QCD [4,5]. The coupling constant of QCD becomes smaller at higher energy scale or smaller length scale due to the asymptotic freedom. Such a state is called as quark-gluon plasma (QGP) [6–8]. These conditions can be achieved in the early universe, the first microsecond after the Big Bang, which suggests that the entire universe was once a large QGP. In the present age, the QGP-like phase may be contained in supermassive celestial bodies such as neutron stars. High-energy heavy-ion collisions are the only way to produce similarly extreme conditions in the laboratory.

1.1.1 QCD phase diagram

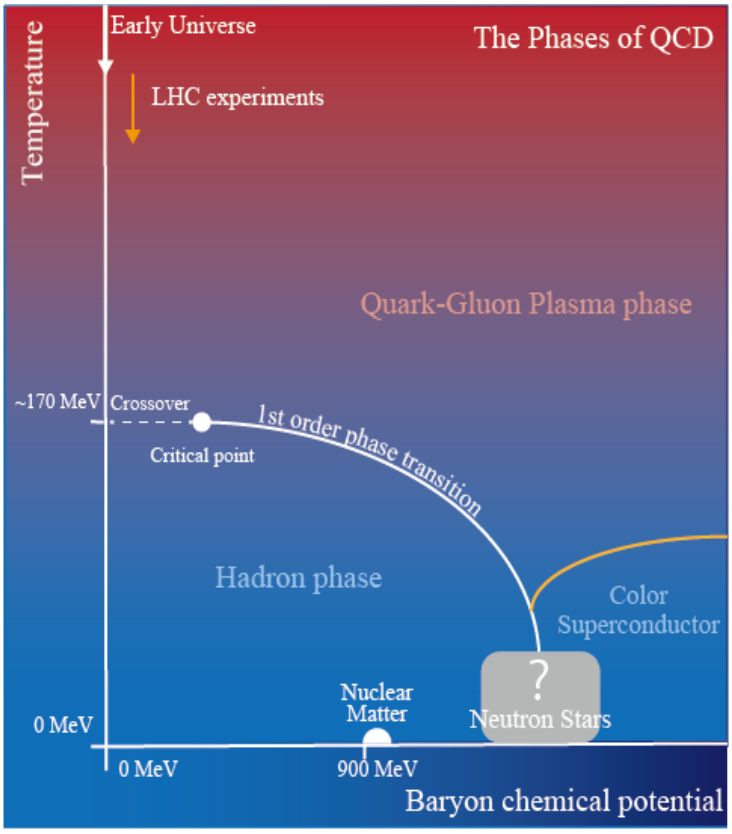

Figure 1.1: The schematic view of the QCD phase diagram.

In this subsection, we review the schematic overview of the QCD phase diagram. In Fig. 1.1, we draw the schematic view of the QCD phase diagram. According to conventions, the QCD phase diagram is drawn as a function of temperature T and baryon chemical potential μ_B which quantifies net baryon number density. For example, the positive μ_B represents the more number of baryons than that of anti-baryons. The predictions of the lattice QCD calculations indicate that the crossover phase transition from the hadron phase to the QGP phase occurs at zero baryon chemical potential [9–13]. The study of several effective theories suggests the existence of a critical point at a finite μ_B [14–18]. The first order phase transition line is terminated at the critical point at some (T, μ_B). However, the current experimental evidence for the existence of the QCD critical point is not obtained with conclusive results.

The equation of state calculated by the lattice QCD at zero μ_B calculations connect to the system's various thermodynamic variables such as temperature, chemical potential, and pressure. At sufficiently high-energy collisions, the baryon chemical potential is vanishing and it may be approximately zero. Temperature and chemical potential of hot and dense matter created in high-energy heavy-ion collisions pass the various trajectories on the QCD phase diagram. Higher energy collisions have a larger temperature and a smaller baryon chemical potential at the beginning. Thus, the created medium in high-energy heavy-ion collisions carries the information of the QCD equation of state on these trajectories. On the other hand, smaller energy collisions have a larger baryon chemical potential. Then, beam energy scanning is possible to explore the QCD phase diagram [19, 20]. The finite chemical potential $\mu_B \neq 0$ is difficult to study by the lattice QCD calculation because of the sign problem [21, 22]. However, in this region, the phase structure has been investigated by effective theories. The analyses of effective theories suggest the existence of the color superconductivity phase at high baryon density and low temperature [23–26].

1.2 High-energy heavy-ion collisions

Currently, the high-energy heavy-ion collider experiments are operated at the Relativistic Heavy Ion Collider (RHIC) of Brookhaven National Laboratory and the Large Hadron Collider (LHC) of the European Laboratory for Particle Physics (CERN). In the laboratory, two nuclei are accelerated to almost the speed of light and are collided with each other to produce the fireball with extremely high temperature above $T \sim 200$ MeV.

One of the purposes of high-energy heavy-ion collisions is the exploration of the QCD phase diagram. At RHIC, production of the strongly interacting QGP was succeeded, which was achieved by measurement of key observables and theoretical interpretation to them [27–30]. In the non-central collisions, the overlapping area of the two nuclei forms the almond shape. As the hydrodynamics flow is induced by the pressure gradient, a larger flow is created in the direction with respect to the shorter axis of the almond shape than that in the direction with respect to the longer axis. As a result, the elliptic flow coefficient v_2 becomes finite. Because of the success to the explain the experimental data such as the radial flow and elliptic flow by relativistic hydrodynamics [31–37], One reached the conclusion that the QGP created at RHIC is not weakly interacting gas but strongly coupled plasma. The electromagnetic probe is also important as a signature of the production of the QGP: the thermal photon spectra as a thermometer of the created medium [38–43], the invariant spectra of the dileptons [38, 40, 44, 45]. The suppression of heavy meson is useful to estimate the temperature of the QGP produced at high-energy heavy-ion collisions such as J/ψ suppression [46–50]. The signature of the achievement of the thermal equilibrium state is the strangeness enhancement [51–55].

At the same time, the lower bound for the dimensionless ratio of shear viscosity to entropy density is evaluated to be $\eta/s = 1/4\pi$ by AdS/CFT correspondence [56]. This is called the Kovton-Son-Starinets (KSS) bound. In the QCD matter, the ratio of the shear viscosity to entropy density takes a minimum value near the critical temperature [57]. The transport coefficients of the QCD matter are investigated by

the Lattice QCD calculations [58–61] and the analysis of Boltzmann equation [62, 63]. This situation triggered the construction and development of relativistic viscous hydrodynamic models [64–67]. The many model parameters in the initialization model of hydrodynamics and the transport coefficients is strongly correlated to many observables in high-energy heavy-ion collisions. This causes difficulty in the interpretation of the results of the phenomenological model of high-energy heavy-ion collisions. In this situation, model-to-data comparison with Bayesian analysis plays an important role in the evaluation of QGP bulk properties such as shear and bulk viscosities and the charge diffusion constant [68–74]. Thus, the present purpose of high-energy heavy-ion collisions is the quantitative study of QGP bulk properties, which is advanced from the search for the existence of QGP.

Recently, electromagnetic fields produced in high-energy heavy-ion collisions are focused. In high-energy heavy-ion collisions, ultraintense electromagnetic fields are produced by two colliding nuclei. The magnitude of the magnetic field reaches the highest in our universe, e.g., $|eB| \sim 10^{15}$ T for $\sqrt{s_{\rm NN}} = 200$ GeV Au-Au collisions [75–79]. The intensity of the magnetic field in the transverse plane becomes large approximately linearly with the center of mass collisions energy ($\sqrt{s_{\rm NN}}$) [80–82]. The correspondence electric field in the transverse plane is also enhanced by a Lorentz factor of colliding nuclei. Such extremely intense electromagnetic fields may be changed the dynamics of the created matter. It results that the hadron distribution detected in high-energy heavy-ion collider deviates. Actually, the charge-dependent anisotropic flow coefficients are observed in LHC and RHIC [83–85]. In the theoretical study, the role of the Lorentz force and Coulomb force has been investigated under some approximations [86, 87]. The investigation of the effect of the magnetic field based on the reduced-magneto-hydrodynamics (MHD) has been studied [88]. Furthermore, analyses of high-energy heavy-ion collisions based on relativistic ideal magneto-hydrodynamics (MHD) also has been performed [89, 90] where electrical conductivity of the created medium is assumed to be infinite. However, experimental conclusive evidence of the existence of ultraintense electromagnetic fields has not been obtained yet.

Furthermore, in the presence of the ultraintense electromagnetic fields, it supposes the novel quantum phenomena such as chiral magnetic effect (CME) [91] and chiral magnetic wave (CMW) [92]. In the strong electromagnetic fields, the strongly interacting deconfined system has non-trivial topological configurations of the color fields. Once, coupled to quarks, these configurations are characterized by a non-zero winding number. It leads to an excess of quarks of a given chirality, well known as the chiral anomaly. As a result, the violation of parity occurs on an event-by-event basis, but it clearly conserves after taking an event average. In the strong magnetic field, it originates the separation of oppositely charged particles with respect to the reaction plane. Since the massless quarks have fixed chirality corresponding to the helicity, and particles tend to align their magnetic moments along the magnetic field, an excess of u-quarks are carried to the direction of the magnetic field and d-quarks are carried to the opposite direction of the magnetic field. After taking event averages, since the parity is conserved, the moving of u-quarks and d-quarks cancels each other. Even though, these effects are reflected to the multiparticle correlations, as proposed in Ref [93]. Such a phenomenon is called CME and it is currently explored by different experimental collaborations at RHIC and the LHC [94–96]. The CME and CMW

signals have been investigated in also iso-bar collision experiments, Zr-Zr and Ru-Ru collisions at RHIC [97,98]. There are no conclusive results of evidence of the existence of the CME and CMW. The investigation of initial electromagnetic fields can address to the detailed discussion of such phenomena.

One of the possibilities for the extension of these studies is the construction of the hydrodynamic model including the electromagnetic response of the QGP medium such as the finite electrical conductivity. In terms of the ideal MHD, the magnetic field is frozen in a plasma element. Then, the evolution of the magnetic field is controlled by the dynamics of created medium. On the other hand, in the relativistic magneto-hydrodynamics (RMHD) with finite electrical conductivity, well known as relativistic resistive magneto-hydrodynamics (RRMHD), the coupling of the electromagnetic fields with created medium becomes weak. In this case, the diffusion of the magnetic field into the vacuum becomes faster than that of the ideal case. Therefore, the effect of electromagnetic fields on hadron distribution may be corrected by the value of the electrical conductivity of the QGP medium. The real QGP may have finite electrical conductivity. In the lattice study of the QCD, the electrical conductivity of the QGP medium is estimated as $\sigma \sim (5.8 \pm 2.9)/\hbar c$ fm^{-1} at temperature $T = 250$ MeV. This value is 10^3 times larger than that of Cu nucleus ($T \sim 20°$C). However, the QGP medium is poor conductive matter in the time scale of the cooling of the QGP medium in high-energy heavy-ion collisions ($\tau_\sigma \sim \frac{1}{\sigma} \sim 10^2$ fm $\gg \tau_f \sim 10$ fm). Then, the ideal approximation of relativistic MHD is not suitable. Furthermore, since, in the ideal approximation, the electric field vanishes in the fluid comoving frame, the electric charge distribution induced by the electromagnetic fields produced by two colliding nuclei can not be precisely estimated. This point becomes more important in the asymmetric collision system such as Cu-Au collisions than that of the symmetric collision system such as Au-Au collisions. The impact of the electrical conductivity on the charge-dependent directed flow has been estimated by focusing on the electric flux in Cu-Au collisions [99]. In this estimate [99], the charge-dependent directed flow is proportional to electrical conductivity of the QGP medium. Thus, the resistive extension of the relativistic ideal MHD model for high-energy heavy-ion collisions is important to evaluate the electrical conductivity of the QGP medium in high-energy heavy-ion collisions.

In this thesis, we develop RRMHD simulation code in the Milne coordinates for high-energy heavy-ion collisions in Chap. 6 [100]. We verify the correctness and robustness of our code by performing several numerical tests which are common test problems for relativistic ideal MHD and RRMHD not only the Cartesian coordinates but also the Milne coordinates in Chap. 7. We also propose the test problem of longitudinal expansion with an acceleration of relativistic resistive magneto-hydrodynamics in Chap. 7. The semi-analytic solution to this problem is shown by mimicking the electromagnetic configuration and fluid velocity in high-energy heavy-ion collisions [101]. We apply this solution as a test problem of RRMHD in the Milne coordinates. Furthermore, we construct the RRMHD model and apply it to high-energy heavy-ion collisions, Au-Au and Cu-Au collisions ($\sqrt{s_{\rm NN}} = 200$ GeV) in Chap. 8 [102]. Numerical results are shown in Chap. 9. We investigate the directed flow of charged π in Au-Au and Cu-Au collisions and reveal the role of the dissipation associated with Ohm's law. We also study the charge-dependent anisotropic flow of charged hadrons in Au-Au and Cu-Au collisions. We found that the charge-dependent anisotropic flow is approximately

proportional to the electrical conductivity of the QGP medium. The comparison of our results with STAR experimental data [84] shows the possibility of the incomplete electromagnetic response of the QGP medium [103, 104]. We conclude that the charge-dependent anisotropic flow is appropriate to detect the electromagnetic response of the QGP medium in high-energy heavy-ion collision experiments.

1.3 Outline of this Thesis

This thesis is organized as in Fig. 1.2. First, we show the basics of kinematics, observable, and current understanding of the collective dynamics in high-energy heavy-ion collisions in Chap. 2. Next, we review the basics of relativistic hydrodynamics in Chap. 4 and relativistic magneto-hydrodynamics in Chap. 5. In Chap. 6, we construct and explain the numerical model of our RRMHD simulation code [100]. We verify our numerical code using several test problems in Chap. 7 [100]. Next, we introduce the newly constructed RRMHD model for high-energy heavy-ion collisions in Chap. 8 [102]. Finally, we analyze the hadron distribution produced by our RRMHD model and calculate the anisotropic flow and charge-dependent anisotropic flow in Chap. 9 [102, 105]. We show the impact of the electromagnetic response of the QGP medium on these observables.

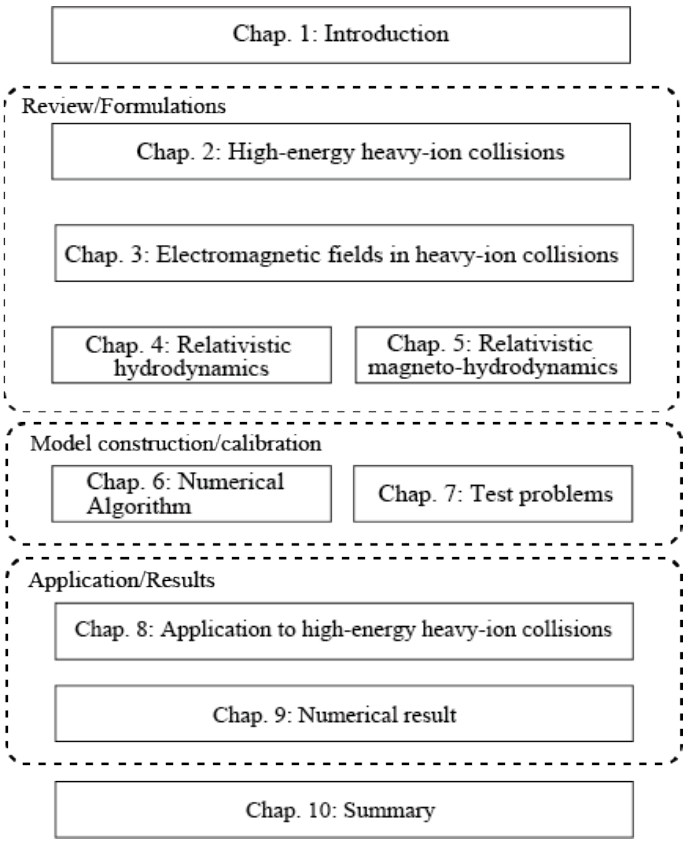

Figure 1.2: Outline of this thesis.

Chapter 2

High-Energy Heavy-Ion Collisions

2.1 Phenomenology of high-energy heavy-ion collisions

In experiments, the observables are related to the particle spectra or momentum distributions. The detected final hadrons carry important information about the bulk property and/or the collective dynamics of the created matter. The final state of the thermalized matter, which is cooled down with collective dynamics, is reflected in the hadron distribution. This indicates that the hadron distribution is sensitive to the collective flow of the matter. On the other hand, the photons and leptons, which are called as electromagnetic probes, serve the information on the inside of the matter since they pass through the created matter with weekly interaction. The number of hadrons (multiplicity), the momentum, and those with identified hadrons are measured in high-energy heavy-ion collisions.

2.1.1 Kinematics

To consider the momenta of measured hadrons, we introduce useful coordinates. The axis parallel to the impact parameter is defined as x-direction. The beam axis crossing the midpoint of the impact parameter vector is defined as z-direction. The x-z plane is defined as a reaction plane. The axis of the normal to the reaction plane is identified as y-direction. The x-y plane is called as the transverse plane. The direction of the z-axis is the longitudinal direction. We also define the momentum of each hadron in the Cartesian coordinates as $p^\mu = (E, p^x, p^y, p^z)$ where $E = \sqrt{m_i^2 + \sum_{\alpha=1}^{3} (p^\alpha)^2}$ with m_i being the mass of the hadron species i. Another set of variables (p_T, y, ϕ) usefully expresses the momentum,

$$E = m_\mathrm{T} \cosh y, \tag{2.1}$$

$$p^z = m_\mathrm{T} \sinh y, \tag{2.2}$$

$$p^x = p_\mathrm{T} \cos\phi, \tag{2.3}$$

$$p^y = p_\mathrm{T} \sin\phi, \tag{2.4}$$

where $p_\mathrm{T} = \sqrt{(p^x)^2 + (p^y)^2}$ is the transverse momentum, and $m_T = \sqrt{m_i^2 + p_\mathrm{T}^2}$ is the transverse mass. The symbol y, not to be confused as the y in the Cartesian

coordinates, defined as rapidity,

$$y = \tanh^{-1}(p^z/E) \tag{2.5}$$
$$= \frac{1}{2}\ln\left(\frac{E+p^z}{E-p^z}\right). \tag{2.6}$$

The angle ϕ is the azimuthal angle of the momentum vector in the transverse plane relative to the x-axis. Those variables are useful to understand the collective dynamics of the medium expanding in the longitudinal direction. However, the measurement of $m_{\rm T}$ and y needs to identify the particle species in order to determine the mass of hadrons. In the analyses of experimental data, we also use the set of variables $(p_{\rm T}, \eta, \phi)$ which does not need particle identification,

$$|\boldsymbol{p}| = p_{\rm T}\cosh\eta, \tag{2.7}$$
$$p^z = p_{\rm T}\sinh\eta, \tag{2.8}$$

where $|\boldsymbol{p}|^2 = \sum_{\alpha=1}^{3}(p^\alpha)^2$. The pseudorapidity η can be written by,

$$\eta = \tanh^{-1}(p_z/|\boldsymbol{p}|), \tag{2.9}$$
$$= \frac{1}{2}\ln\left(\frac{|\boldsymbol{p}|+p_z}{|\boldsymbol{p}|-p_z}\right), \tag{2.10}$$
$$= -\ln[\tan(\theta/2)], \tag{2.11}$$

where it only depends on the polar angle θ of the momentum vector relative to the beam axis. The rapidity and pseudorapidity are approximately equal in the ultrarelativistic limit, $p \gg m$. Then, the Lorentz invariant volume element is transformed as $d^3p/E = p_{\rm T}dp_{\rm T}d\phi dy/E = (p/E^2)p_{\rm T}dp_{\rm T}d\phi d\eta$. The Lorentz invariant momentum distribution of hadrons is written by,

$$E\frac{d^3N(\boldsymbol{p})}{d^3p} = \frac{dN(y,p_{\rm T},\phi)}{p_{\rm T}dp_{\rm T}d\phi dy} = \frac{E}{p}\frac{dN(\eta,p_{\rm T},\phi)}{p_{\rm T}dp_{\rm T}d\phi d\eta}. \tag{2.12}$$

2.1.2 Collision geometry

The important observables such as momentum distributions and the correlation among particles are affected by the collision geometry. In the statistical analyses of the experimental data, we need to classify the events using the observables which are related to the collision geometry.

Centrality

The most important collision geometry in heavy-ion collisions, which determines the global configuration of the created matter, is the impact parameter of the collision. In heavy-ion collisions, the events include not only central collisions but also peripheral collisions. In Fig. 2.1, the left picture represents the central collision, and the right picture represents the peripheral collision. At the most central collision, the impact parameter is almost zero. Most of the nucleons inside two colliding nuclei participate in the collision. On the other hand, in the peripheral collision, only the nucleon in the

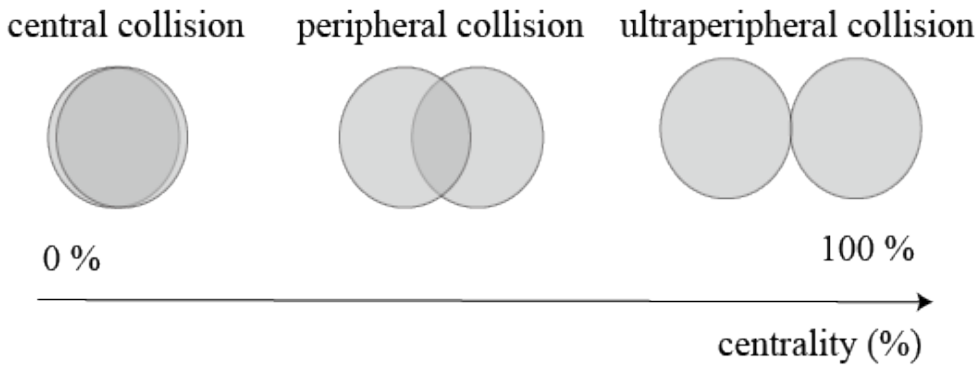

Figure 2.1: The schematic expression of the centrality in terms of collision geometry. The left picture shows the collision geometry of central collisions. The central collisions have the impact parameter which is almost zero. The center picture represents peripheral collisions with a finite impact parameter. The right picture expresses the ultraperipheral collisions. In ultraperipheral collisions, the impact parameter is almost same as the radius of nucleus.

overlapping area of the two colliding nuclei, with an almond shape in the transverse plane, participates in the collision. The participating nucleons are called participants. The other nucleons outside the overlapping area pass through the forward and backward rapidity. These nucleons are called spectators. In high-energy heavy-ion collisions, the impact parameter cannot be directly measured in the experiments, but it is strongly correlated with the multiplicity of hadrons $N_{\rm ch}$ or the total transverse energy $E_{\rm T}$. The multiplicity and the transverse energy are large with a small impact parameter (central collision). In the experiments, we classify the events of different impact parameters as centrality (%). The most central collision is denoted as 0%. The most peripheral collision is indicated as 100%. In Tab. 2.1, we show the event averaged charged particle multiplicity density per-unit pseudorapidity $\langle dN_{ch}/d\eta \rangle$ and the number of participants $\langle N_{\rm part} \rangle$ for each centrality in the ALICE experiments [106]. The clear correlation between centrality and these observables is experimentally observed. The $\langle dN_{ch}/d\eta \rangle$ and $\langle N_{\rm part} \rangle$ decrease with increasing the centrality %.

Table 2.1: The event averaged charged-particle multiplicity at midrapidity and the average number of participants for the centrality bins [106]

Centrality %	$\langle dN_{ch}/d\eta \rangle$	$\langle N_{\rm part} \rangle$
0-5	1601 ± 60	382.8 ± 3.1
5-10	1294 ± 49	329.7 ± 4.6
10-20	966 ± 37	260.5 ± 4.4
20-30	649 ± 23	186.4 ± 3.9
30-40	426 ± 15	128.9 ± 3.3
40-50	261 ± 9	85.0 ± 2.6
50-60	149 ± 6	52.8 ± 2.0
60-70	76 ± 4	30.0 ± 1.3
70-80	35 ± 2	15.8 ± 0.6

2.1.3 Particle production and anisotropic flow

Anisotropic flow coefficients

One of the important observables to extract the collective dynamics of the created medium is the azimuthal anisotropic flow coefficients v_n. To quantify the transverse momentum anisotropy, we define the azimuthal anisotropic flow coefficients v_n as a Fourier series as a function of azimuthal angle,

$$\frac{dN}{d\phi} \propto 1 + 2\sum_{n=1}^{\infty} v_n \cos[n(\phi - \Psi_n)], \tag{2.13}$$

where the event-plane angle Ψ_n is the corresponding phase and the flow coefficient v_n is defined as the magnitude of nth-order anisotropy,

$$v_n = \frac{\int d\phi \cos[(n(\phi - \Psi_n)] \frac{dN}{d\phi}}{\int d\phi \frac{dN}{d\phi}}. \tag{2.14}$$

The v_1, v_2, and v_3 are called as "the directed flow", "the elliptic flow", and "the triangular flow", respectively. The non-zero v_1 means the hadrons are emitted in one direction. It is very small since the total transverse momentum cancels out in symmetric collision systems such as Au-Au and Pb-Pb collisions. On the other hand, in asymmetric systems such as Cu-Au collisions, the directed flow becomes more important since the pressure gradient in the transverse plane is the strongest with respect to the direction of the center of Cu nucleus in Cu-Au collisions. The elliptic flow v_2 becomes large in the non-central collisions because of the geometrical origin of two colliding nuclei. The higher anisotropic flow coefficients have been also discussed in Ref. [107–111].

Elliptic flow

As shown in Fig. 2.2, the nuclei collide with impact parameter b along the x-axis, creating the almond-shaped overlapping area. In this area, the QGP medium forms.

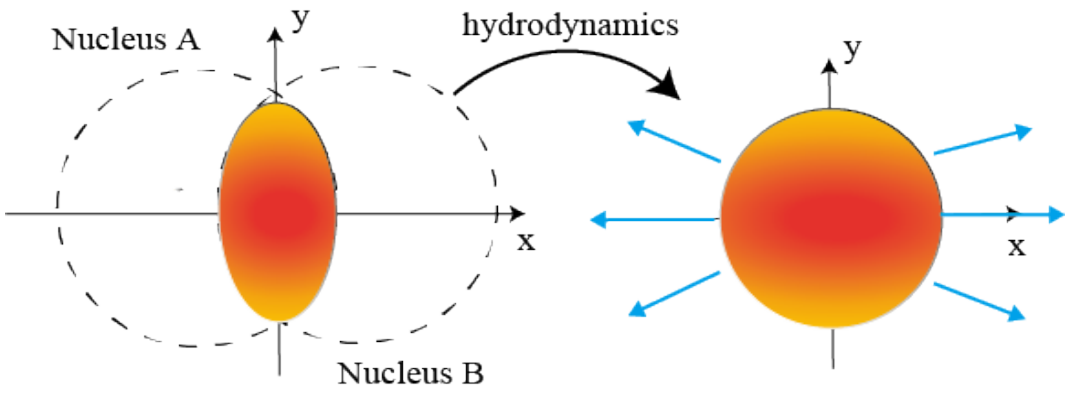

Figure 2.2: The schematic view of different contributions to the elliptic flow.

This shape induces a strong pressure gradient along the x-axis compared to y-axis. In the hydrodynamical evolution, the medium expands anisotropically by this pressure gradient. The fluid strongly expands in the direction of the shorter axis of the almond shape. This anisotropic expansion is reflected to the momentum distribution of emitted hadrons. The momentum distribution of the hadrons has elliptic azimuthal anisotropy in the transverse plane. The elliptic flow coefficient is defined as,

$$v_2 = \langle \cos[2(\phi - \Psi_2)] \rangle. \tag{2.15}$$

In the experiments, the elliptic azimuthal anisotropy of the momentum space of hadrons is observed [34, 112, 113]. The hydrodynamics successfully explained the behavior of the elliptic azimuthal momentum anisotropy measured in high-energy heavy-ion collisions [114–121]. This result has reached the conclusion that the QGP is not a weekly interacting gas but a strongly interacting plasma.

Directed flow

The directed flow is quantified the coefficient v_1 defined as,

$$v_1 = \langle \cos[\phi - \Psi] \rangle. \tag{2.16}$$

In symmetric collisions, the directed flow is exactly zero at central rapidity. On the other hand, as shown in the orange arrow in Fig. 2.3, in forward and backward rapidity regions, the directed flow is finite due to the tilted source of directed flow explained in details in Sec. 8. At RHIC energy, the spectator has the positive (negative) directed flow at the forward (backward) rapidity region, resulting from the deflection of the spectators during the collision. On the other hand, the produced matter has the opposite sign-directed flow of spectators for $-4 < \eta < 4$ and for the centrality $0 - 80\%$ both for Au-Au and Cu-Cu collisions [122–124]. Since the medium at the backward rapidity region is strongly affected by nucleus A compared with nucleus B, the shape of the medium is tilted in the reaction plane as shown in Fig. 2.3. As a consequence of it, the medium flow along with orange arrow in Fig. 2.3. The directed flow has

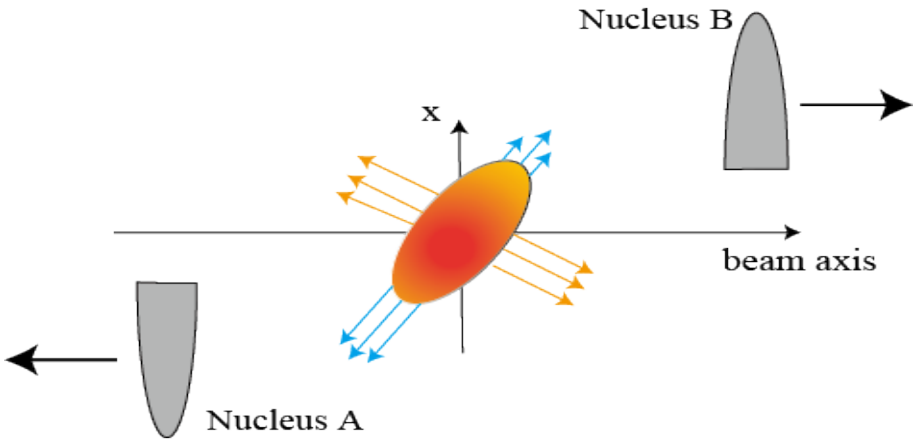

Figure 2.3: The schematic view of different contributions to the directed flow. The blue arrow denotes the asymmetric density gradient of the initial pressure of the fluid due to the difference of the two colliding nuclei. It is vanishing in symmetric collision systems. The orange arrow represents the tilted source of the directed flow.

a positive value in the backward rapidity region and a negative value in the forward rapidity region. A significant measurement of the directed flow is the large negative value of the directed flow coefficient even in collision at $\sqrt{s_{\rm NN}} = 200$ GeV Au-Au collisions. Another important subject is the system size dependence of the directed flow coefficient. The coefficient of the directed flow is the same for both Au-Au and Cu-Cu collisions.

In asymmetric collision systems such as Cu-Au collisions, the directed flow is a more important quantity to extract the collective dynamics of the QGP matter due to the asymmetric shape of the matter with respect to the impact parameter [99, 125, 126]. The strongest pressure gradient is induced since the volume of Cu nucleus is smaller than that of Au nucleus. The medium is strongly accelerated to the direction of the center of Cu nucleus. As a result, the momentum parallel to the impact parameter of hadrons becomes large. Then, the directed flow becomes finite even at $\eta = 0$ in Cu-Au collisions. In Cu-Au collisions, the non-zero value of the directed flow is observed at $\eta = 0$ [127–129]. Furthermore, the electric field is produced by the two colliding nuclei due to the differences in the charge of the nuclei. It induces charge differences in the directed flow,

$$\Delta v_n = v_n(h^+) - v_n(h^-), \tag{2.17}$$

where $h^\pm$ denotes the positively or negatively charged hadrons. Early estimates of the charge differences of the directed flow are obtained by [99],

$$\Delta v_1 \sim -\frac{\pi\sigma\tau}{N_{\rm tot}} \frac{Z_{\rm Au} - Z_{\rm Cu}}{2}, \tag{2.18}$$

where σ is the electrical conductivity, τ is a proper time of the evolution of the hydrodynamics and $N_{\rm tot}$ is the total number of charged particles. We have also defined that the $Z_{\rm Au/Cu}$ is the number of electric charges inside the Au/Cu nucleus. Then, the difference in the directed flow is an important probe of the electromagnetic response of the QGP medium due to be proportional to electrical conductivity.

2.2 The standard description of dynamics in collision process

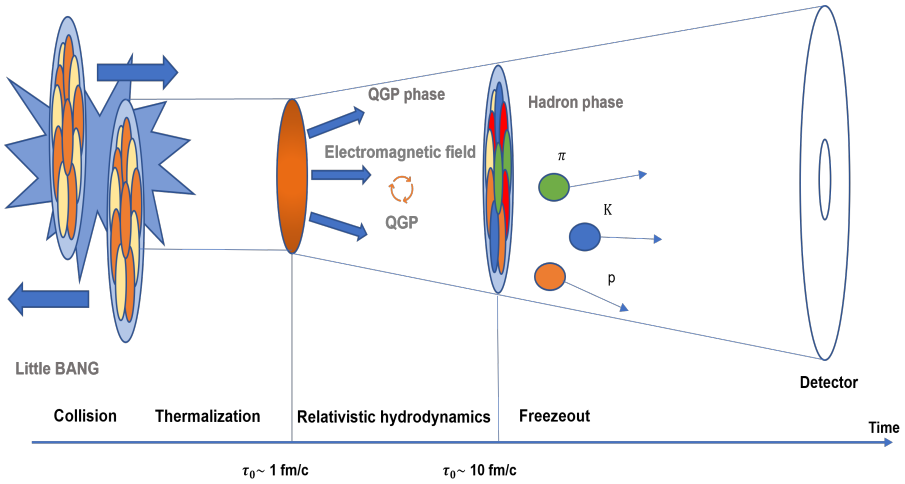

Figure 2.4: The schematic picture of the standard description of high-energy heavy-ion collisions.

There are several dynamical models to describe the processes of high-energy heavy-ion collisions [62, 64–67, 130–132]. The state of the matter is completely different at each stage through the process of high-energy heavy-ion collisions. From the initial color grass condensate to the final non-interacting hadrons, the variety of the behavior of the QCD matter can be observed. To describe such an evolution QCD matter with quite different processes, state-of-the-art dynamical models combine the initial state models, hydrodynamic simulation, and hadronic cascade models. In this section, let us review the dynamics of the whole process of high-energy heavy-ion collisions.

As shown in Fig. 2.4, the created matter starts from a thin area between two colliding nuclei because of the Lorentz contraction. It expands to the longitudinal direction at almost speed of light. To capture the feature of such expansion of the matter, the Milne coordinates (τ, x, y, η_s) are useful, where τ is proper time and η_s is space rapidity. The transformation from the Cartesian coordinates to the Milne coordinates is given by,

$$\tau = \sqrt{t^2 - z^2}, \tag{2.19}$$

$$x_M = x_C, \tag{2.20}$$

$$y_M = y_C, \tag{2.21}$$

$$\eta_s = \tan^{-1}(z/t) = \frac{1}{2}\ln\left(\frac{t+z}{t-z}\right). \tag{2.22}$$

Its inverse transformation is written by,

$$t = \tau\cosh(\eta_s), \tag{2.23}$$

$$z = \tau\sinh(\eta_s). \tag{2.24}$$

The initial state of high-energy heavy-ion collisions is described by a color-glass condensate picture. This medium instantaneously thermalized with $\tau \lesssim 1$ fm/c. There are developed various models to investigate this initial state [133–137].

After the thermalization, the system has achieved the local thermal equilibrium state. The hydrodynamic evolution may be adopted in this stage. This evolution produces the collective flow of the created plasma. The initial spatial anisotropy is converted to the momentum anisotropy of the final hadronic matter by the hydrodynamic expansion.

Since the temperature of the produced matter becomes lower because of the hydrodynamic expansion, the microscopic picture of the matter is gradually transitioned from quarks and gluons to hadrons. The mean-free path of hadronic matter becomes larger than that in the partonic matter and the system size. In this stage, the description of the hadronic system is described as hadronic gases rather than hydrodynamics. The switching from hydrodynamic picture to hadronic particle picture is executed on the isothermal hypersurface at $T = T_{\rm sw} \sim 150$ MeV. The dynamics of the created hadronic gas is described by the kinetic theory where hadronic decay and scattering with each other. This procedure is called a hadronic cascade, or hadronic afterburner.

2.2.1 Initialization models

Hydrodynamics well describes the spacetime evolution of the QGP medium, but not well understood how it forms. Some other physical processes must take into account for the construction of the initial energy density profile immediately after the collisions. The system takes a short time $\tau \sim 1$ fm to begin the hydrodynamic expansion. The hydrodynamic equations are differential equations and require an initial condition.

The simplest phenomenological model of the initial condition of the high-energy heavy-ion collisions is the Glauber model [133, 134]. The experimental multiplicity of hadrons is fitted with the number density of the participant nucleons and the number density of the binary nucleon collisions. In ideal hydrodynamics, the final multiplicity of the hadrons is proportional to the entropy density on the freezeout hypersurface where hydrodynamics is terminated. Since the entropy current is conserved by the ideal hydrodynamics evolution, the final entropy density corresponds to the initial entropy density. In the Glauber model, the initial entropy density in the transverse plane at the collision point is determined by the local density of nucleons in the two colliding nuclei. This local nucleon density is calculated as the thickness function,

$$T_{\rm A/B}(x,y) = \int dz \rho_{\rm nucleus}(x,y,z), \tag{2.25}$$

$$\rho_{\rm nucleus}(x,y,z) = \frac{\rho_0}{1+\exp\left(\frac{r-R}{a}\right)}, \tag{2.26}$$

where $\rho_{\rm nucleus}$ is well known as Woods-Saxon distribution, ρ_0 is a nucleon density at center of the nucleus, R is a radius of the nucleus, and a is a surface thickness. The participant density is calculated by the $T_{\rm A/B}$ multiplied by the probability of the collisions at each transverse position. The binary nucleon collision density is proportional to $T_A T_B$. In the conventional Glauber model, the initial entropy density is parametrized as a function of the participant density $n_{\rm part}$ and the binary nucleon collision density $n_{\rm coll}$.

Another initial model, which is often compared with the Glauber models, is the color-glass-condensate (CGC) model based on the CGC picture [135–137]. In sufficiently high-energy collisions, the matter of the early stage is described by the production of soft gluons. This picture successfully explained well experimental results in higher collision energy such as Pb-Pb collisions ($\sqrt{s_{\rm NN}} = 2.76$ and 5.02 TeV) at the LHC. Recently, with the development of bayesian analysis of the model-to-data comparison for high-energy heavy-ion collisions, the model of the connecting Glauber model to CGC-based initial condition by one parameter has been investigated [68, 69].

2.2.2 Hydrodynamic expansion

After the production of the matter forms a local thermal equilibrium condition of quarks and gluons, the hydrodynamic description is applicable to describe the spacetime evolution of the produced matter. The initial spatial anisotropy is converted to the final momentum distribution mainly by the hydrodynamics expansion of the QGP in this stage. This expansion is determined by the bulk properties and the transport coefficients of the QGP such as value of transport coefficients, and the constitutive equation with transport coefficients. The details of the relativistic hydrodynamic framework are introduced in Chap. 4.

In high-energy heavy-ion collisions, the radial expansion in the transverse plane is induced by the finite size of the colliding nuclei. The final emitted hadrons are boosted by this expansion. As a result, the mean transverse momentum $\langle p_{\rm T} \rangle$ increases. Besides, the initial almond shape of the energy density profile is converted to the final momentum elliptic anisotropy by the hydrodynamic expansions. This effect is reflected to the observed strong elliptic flow coefficient v_2.

Recently, electromagnetic fields produced by two colliding nuclei also have been discussed. In the hydrodynamic evolution, Maxwell's stress force affects the expansion of the thermalized matter. The possibility of the change of the elliptic flow and directed flow is suggested in Refs. [88, 138]. In the RMHD framework, such dynamics depends on the modeling of Ohm's law and the value of electrical conductivity. As a further discussion, the incomplete electromagnetic response of the QGP medium is also reflected to the dynamics of the medium [103, 104]. This indicates that relaxation time of electric current plays an important role in the dynamics of the QGP medium. The details of the framework of RMHD are introduced in Chap. 5.

2.2.3 Hadronization

The outputs of the hydrodynamics are the fluid flow, temperature, and density on the freezeout hypersurface. To evaluate the observables using these outputs, we should convert these fluid variables to the hadron distribution. With given hydrodynamic variables on a freezeout hypersurface Σ_f, the spectrum of a hadrons i can be represented with Cooper-Frye prescription [139],

$$E\frac{d^3N_i}{dp^3} = \frac{g_i}{(2\pi)^2}\int_{\Sigma_f} d^3\sigma_\mu p^\mu f(p,x), \tag{2.27}$$

where g_i is a degree of freedom of hadron i, and $d^3\sigma^\mu$ is a surface element of the freezeout hypersurface Σ_f. Here, the produced hadron gas is sufficiently dilute gas,

and the interaction among hadrons can be ignored. Thus, the distribution function can be assumed to be the one-particle distribution function. The distribution function $f(p, x)$ gives the momentum distribution of hadrons at the position x of a freezeout hypersurface element.

In the ideal hydrodynamics, the local momentum distribution is obtained by the Bose-Einstein distribution or Frmi-Dirac distribution,

$$f(p, x) = \frac{1}{e^{\beta(p^\mu u_\mu - \mu_i)} \pm 1}, \tag{2.28}$$

where $\beta = 1/T$ is the inverse temperature, μ_i is a chemical potential of the hadrons, and u_μ is a four-velocity of the fluid. The statistical sign of the denominator is $+1$ for fermions and -1 for bosons. The energy-momentum tensor of ideal hydrodynamics is reproduced by the above distribution function of the hadrons in kinetic theories.

2.2.4 Hadronic cascades

Hadronic cascades describe the spacetime evolution of the hadronic gas. The hadronic gas is taken to be the finite number of classical particles. In cascade models, hadrons decay or scatter with each other. Every pair of hadrons is tested whether they scatter with each other. Two hadrons scatter with each other if the distance between them is smaller than the radius determined by the total cross-section of the two hadrons. For elastic scattering, the momentum of the hadrons is changed. For inelastic scattering, new hadrons are created instead of the original hadrons. The decay is performed by removing parent particles and producing daughter particles at a randomly sampled time with its decay rate. There are several models of hadronic cascades which have been adopted in high-energy heavy-ion collisions such as UrQMD [140–142], JAM [143, 144], and SMASH [145, 146].

Chapter 3

Erectromagnetic fields in Heavy-Ion Collisions

In high-energy heavy-ion collisions, ultraintense electromagnetic fields are produced by two colliding nuclei. The magnitude of the magnetic field reaches the highest in our universe, e.g., $|eB| \sim 10^{15}$ T for $\sqrt{s_{\rm NN}} = 200$ GeV Au-Au collisions [75–79]. In this chapter, we review the property of electromagnetic fields in high-energy heavy-ion collisions.

3.1 Computation of electromagnetic field

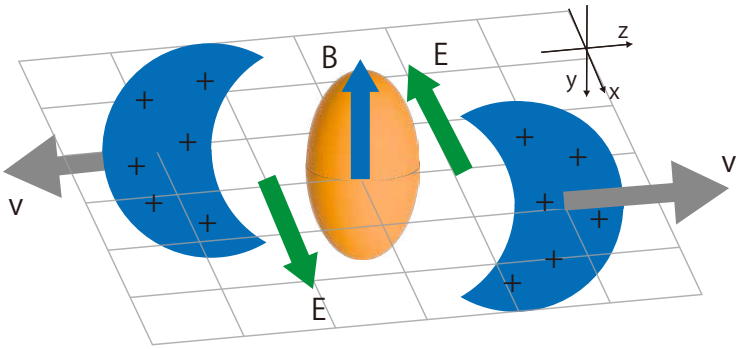

Figure 3.1: The schematic view of heavy-ion collision with electromagnetic fields produced by colliding nuclei.

As shown in Fig. 3.1, two colliding nuclei produce electromagnetic fields. According to Biot-Savart law, the running charged particles induces the magnetic fields around particles. In heavy-ion collisions, the magnetic fields produced by two colliding nuclei reinforce each other in the reaction area. Let us consider Au-Au collisions ($\sqrt{s_{NN}} = 200$ GeV) at fixed impact parameter b. If we approximate the nucleus to be point-charged particles, we get the magnetic field strength by naively applying the Biot-Savart law,

$$-eB_y \sim 2Z_{\rm Au}\gamma\frac{e^2}{4\pi}v_z\left(\frac{2}{b}\right)^2 \sim 10m_\pi^2 \sim 10^{15} - 10^{16}\ {\rm T}, \tag{3.1}$$

where $v_z = \sqrt{1-(2m_N/\sqrt{s_{\rm NN}})} \sim 0.99995$ (m_N is a nucleon mass) is the velocity of the nucleus, $\gamma = 1/\sqrt{1-v_z^2} \sim 100$ is the Lorentz factor of the nucleus, and $Z_{\rm Au} = 79$ is the charge number of the gold nucleus. The left-hand side has the minus sign because the magnetic field is facing the $(-y)$-direction as shown in Fig. 3.1. It is sufficiently larger than the square of mass of electrons, m_e^2 and light flavor quarks, m_u^2 and m_d^2, to be capable to induce the significant quantum phenomena. It is also larger than the magnetic field of neutron stars including the magnetars which may have a surface magnetic field of the order of $10^{10}-10^{12}$ T. One can expect that such a large magnetic field may affect the important results on the evolution of QGP matter produced in high-energy heavy-ion collisions. Precisely, in order to discuss the effect of electromagnetic fields beyond this early estimate, we need to consider the knowledge of the proton and neutron distributions in a nucleus. For this subject, we can take the Woods-Saxon distributions as nucleon distributions. In real high-energy heavy-ion collisions, since the proton distribution may fluctuate from one nucleus to another, the electromagnetic fields may also fluctuate event by event basis [80–82]. In early estimate Eq. (3.1), we apply the Biot-Sarvart law. Furthermore, we need to replace the Biot-Savart law with the full relativistic Liénard-Wiechert potentials which include the retarded effect,

$$e\boldsymbol{E}(t,r) = \frac{e^2}{4\pi}\sum_n Z_n \frac{\boldsymbol{R}_n - R_n\boldsymbol{v}_n}{(R_n - \boldsymbol{R}_n\cdot\boldsymbol{v}_n)^3}(1-v_n^2), \tag{3.2}$$

$$e\boldsymbol{B}(t,r) = \frac{e^2}{4\pi}\sum_n Z_n \frac{\boldsymbol{R}_n \times \boldsymbol{v_n}}{(R_n - \boldsymbol{R}_n\cdot\boldsymbol{v}_n)^3}(1-v_n^2), \tag{3.3}$$

where the summation is over all the charged particles inside colliding nuclei, Z_n is the charge number of the nth particle, $\boldsymbol{R_n} = \boldsymbol{r} - \boldsymbol{r}_n$ is the relative position of the field point $\boldsymbol{r}$ to the source point $\boldsymbol{r}_n$ of the nth particle, and $\boldsymbol{v}_n$ is the velocity of nth particle at the retarded time $t_n = t - |\boldsymbol{r} - \boldsymbol{r}_n|$.

3.1.1 Collision energy dependence

The magnitude of electromagnetic fields at LHC energy is around 14 times larger than that at RHIC energy. Naively, they hold the linear dependence on the collision energy,

$$e\cdot\text{Field} \propto \sqrt{s_{\rm NN}} f(b/R_{\rm A}), \tag{3.4}$$

where $R_{\rm A}$ is a radius of the nucleus and $f(b/R_{\rm A})$ is a universal function. Actually, a more general form of Eq. (3.4) is obtained from Eqs. (3.2) and (3.3). As the fields at $t = 0$ fm are mainly caused by spectators and participants which has velocity $v_z = \sqrt{1-(2m_{\rm N}/\sqrt{s_{\rm NN}})} \sim 1$, the electric and magnetic fields at $t = 0$ in the transverse plane is written by,

$$e\boldsymbol{E}_\perp \sim \frac{e^2}{4\pi}\frac{\sqrt{s_{\rm NN}}}{2m_{\rm N}}\sum_n \frac{\boldsymbol{R_{n\perp}}}{R_{n\perp}^3}, \tag{3.5}$$

$$e\boldsymbol{B}_\perp \sim \frac{e^2}{4\pi}\frac{\sqrt{s_{\rm NN}}}{2m_{\rm N}}\sum_n \frac{\boldsymbol{e}_{nz}\times\boldsymbol{R_{n\perp}}}{R_{n\perp}^3}, \tag{3.6}$$

where $\boldsymbol{e}_{nz}$ is the unit vector in z-direction depending on whether the nth charged particles is in two colliding nuclei and $\boldsymbol{R}_{n\perp}$ is the transverse position of the nth charged particle which is independent of $\sqrt{s_{\rm NN}}$, and $R_{n\perp} = |\boldsymbol{R}_{n\perp}|$. For the event-averaged magnetic field $e\langle B_y\rangle$, the following form is approximately written by,

$$e\langle B_y\rangle \propto \frac{\sqrt{s_{\rm NN}}}{2m_{\rm N}}\frac{Z}{A^{2/3}}\frac{b}{2R_{\rm A}}m_\pi^2, \text{ for } 0 < b < 2R_{\rm A}. \tag{3.7}$$

We note that the event-averaged electric field vanishes, $\langle eE_x\rangle = 0$, since the electric field produced by two colliding nuclei is canceled out each other at $\boldsymbol{r} = \boldsymbol{0}$ fm, $\eta_s = 0$ and $t = 0$ fm in the symmetric collisions. Then, the electric field can contribute only to event-by-event fluctuations.

3.2 Evolution of electromagnetic field

3.2.1 Pre-equilibrium stage evolution

After high-energy heavy-ion collisions, the produced partonic matter mainly consists of gluons and remains in a far-from-equilibrium state. This created partonic matter evolves toward a thermal equilibrium state and the production of quarks and anti-quarks pairs occurs during this process. Although the evolution of partonic matter in a far-from-equilibrium state has not been understood extensively, the phenomenological studies found that the timescale of the achievement of the thermalization is very shorter than the total lifetime of the QGP phase [147–150]. Once the thermal equilibrium is locally achieved, the bulk evolution of the partonic matter is described by relativistic hydrodynamics. One of the transport coefficients of the hydrodynamics characterized electromagnetic response, namely, the electrical conductivity has been numerically investigated by using lattice QCD calculations. The electrical conductivity σ makes the QGP matter sensitive to electromagnetic fields and which in turn strongly influences the time evolution of electromagnetic fields. To the evolution of electromagnetic fields in the QGP phase, we need to consider the interaction between QGP matter and electromagnetic fields. Then, we will discuss the evolution of electromagnetic fields in the QGP phase next subsection. In this subsection, we will focus on the stage before the thermal equilibrium (we call this stage the "pre-equilibrium stage").

The partonic matter in the pre-equilibrium stage is expected to have lower conductivity than in the QGP stage. We ignore the response of the matter to the electromagnetic fields in this stage for simplicity. The contribution to electromagnetic fields obtains from the charged particles in mainly spectators and participants. The spectators move far away from the collision region. The remnants move much slower than the spectators. They become more important than the spectators and make the decay of electromagnetic fields slow down. The timescale of diffusion of the magnetic field because of the spectators is estimated as,

$$t_{\rm B} \sim R_{\rm A}/(\gamma v_z) \sim \frac{2m_N}{\sqrt{s_{\rm NN}}}R_{\rm A}, \tag{3.8}$$

which is one-half the time that one proton path through the nucleus. The lifetime is very short for high collision energy $\sqrt{s_{\rm NN}}$. For Au-Au collisions at $\sqrt{s_{\rm NN}} = 200$ GeV,

the lifetime is $t_B \sim 0.065$ fm, while for Pb-Pb collisions at $\sqrt{s_{\rm NN}} = 2.76$ TeV, the lifetime is $t_B \sim 0.005$ fm. When $t \sim t_{\rm B}$, we can approximate the time evolution of the event-averaged magnetic field in the pre-equilibrium stage,

$$\langle eB_y(t)\rangle \sim \frac{\langle eB_y(0)\rangle}{(1+t^2/t_{\rm B}^2)^{3/2}}. \tag{3.9}$$

This relation works well for peripheral collision which has large impact parameter b and high collision energy $\sqrt{s_{\rm NN}}$. The Eq. (3.9) represents that for $t \gg t_{\rm B}$ the magnetic field evolves fast,

$$\langle eB_y(t)\rangle \sim \frac{t_{\rm B}^3}{t^3}. \tag{3.10}$$

However, if at that time $t_{\rm B}$ the QGP has been already created in high-energy heavy-ion collisions, the electromagnetic response of the QGP medium will significantly affect the time evolution of the electromagnetic fields.

3.2.2 Equilibrium-stage evolution

In the estimate of electromagnetic fields, we have ignored the electromagnetic response of the partonic matter produced by the colliding nuclei. This assumption is justified only in the pre-equilibrium stage where the system is gluon dominated but becomes less justified as the system evolves with quarks and anti-quarks pairs created.

In fact, the QGP has finite electrical conductivity according to the theoretical and lattice QCD studies. At a very high temperature which is enough to justify the perturbative QCD, the perturbative study gives that the electrical conductivity of the QGP medium is $\sigma \sim 6T/e^2$ [63]. The lattice QCD calculation with $N_f = 0$ found that $\sigma \sim 7C_{em}T$ [151] at $1.5T_c < T < 3T_c$ with T_c is the deconfinement temperature. Another quenched lattice QCD calculation using staggered fermions found that $\sigma \sim 0.4C_{em}T$ [152]. Recent quenched lattice QCD simlation using Wilson fermions revealed that $\sigma \sim (1/3)C_{em}T - C_{em}T$ [153–155] for $T_c < T < 3T_c$. The lattice simulation with two flavored dynamical Wilson fermions found that $\sigma \sim 0.4C_{em}T$ at $T \sim 250$ MeV [156]. Another lattice QCD calculation using three flavored fermions found that $\sigma \sim 0.1C_{em}T - 0.3C_{em}T$ for $T_c < T < 2T_c$ [157, 158]. In these simulations, the electromagnetic vertex parameter $C_{em} = \sum_f q_f$ with q_f the charge of the quark corresponding flavor f. For example, $C_{em} = (5/9)e^2$ if u and d quarks are considered while $C_{em} = (2/3)e^2$ if u, d, and s quarks are taken. We note that the value of the temperature T_c is different in $N_f = 0$ and $N_f \neq 0$ cases; if $N_f = 0$ we have $T_c = 270$ MeV while if we take $N_f = 2 + 1$ we get $T_c \sim 170$ MeV.

Now let us discuss how the electrical conductivity σ influences the time evolution of the electromagnetic fields in the QGP phases stage which we call to "equilibrium stage". In this subsection, we will consider the evolution of electromagnetic fields based on magneto-hydrodynamics. Maxwell equations are written by,

$$\boldsymbol{\nabla} \times \boldsymbol{E} = -\partial_t \boldsymbol{B}, \tag{3.11}$$

$$\boldsymbol{\nabla} \times \boldsymbol{B} = \partial_t \boldsymbol{E} + \boldsymbol{J}, \tag{3.12}$$

where $\boldsymbol{J}$ is the electric current. We deal with the QGP as being locally charge-neutral with finite electrical conductivity. Then, $\boldsymbol{J}$ is the sum of the external electric current

and the electric current induced by Ohm's law,

$$\boldsymbol{J} = \sigma(\boldsymbol{E} + \boldsymbol{v} \times \boldsymbol{B}) + \boldsymbol{J}_{\rm ext}, \tag{3.13}$$

where $\boldsymbol{v}$ is the fluid velocity of QGP and $\boldsymbol{J}_{\rm ext}$ is the external current induced by the motion of protons which comes from mainly spectators. Substituting Eq. (3.13) into Eqs. (3.11) and (3.11), we can obtain following Maxwell equations as,

$$\partial_t \boldsymbol{B} = \boldsymbol{\nabla} \times \boldsymbol{v} \times \boldsymbol{B} + \frac{1}{\sigma}\left(\nabla^2 \boldsymbol{B} - \partial_t^2 \boldsymbol{B} + \boldsymbol{\nabla} \times \boldsymbol{J}_{\rm ext}\right), \tag{3.14}$$

$$\partial_t \boldsymbol{E} + \partial_t \boldsymbol{v} \times \boldsymbol{B} = \boldsymbol{v} \times (\boldsymbol{\nabla} \times \boldsymbol{E}) + \frac{1}{\sigma}\left(\nabla^2 \boldsymbol{E} - \partial_t^2 \boldsymbol{E} - \partial_t \boldsymbol{J}_{\rm ext}\right), \tag{3.15}$$

where we have used Gauss's law for the magnetic field and the electric field $\boldsymbol{\nabla} \cdot B = 0$ and $\boldsymbol{\nabla} \cdot E = 0$. The first terms on the right-hand sides of Eqs. (3.14) and (3.15) are called as the convection term, while the other terms are called as "diffusion terms".

If we set to $\boldsymbol{v} = 0$, the Eq. (3.14) reduces to,

$$\partial_t \boldsymbol{B} = \frac{1}{\sigma}\left(\nabla^2 \boldsymbol{B} - \partial_t^2 \boldsymbol{B} + \boldsymbol{\nabla} \times \boldsymbol{J}_{\rm ext}\right). \tag{3.16}$$

One can solve this equation using the method of Green's function [78, 81, 159–162]. In these studies, the solution of this equation shows that the presence of the conducting medium can make the decay of the magnetic field significantly slow down. This is explained as the consequence of the Faraday induction. A circular electric current in the medium is induced by a fast decaying external magnetic field. In turn, this circular electric current causes a magnetic field that compensates for the decaying external magnetic field.

For late times, the external current $\boldsymbol{J}_{\rm ext}$ from the spectators can be neglected. If $\sigma \gg 1/t_c$ where t_c is the time scale which characterized the electromagnetic fields strongly changes, the second-order time derivative of the field term can be neglected. In this assumption, Eq. (3.16) becomes,

$$\partial_t \boldsymbol{B} = \frac{1}{\sigma}\nabla^2 \boldsymbol{B}. \tag{3.17}$$

This describes the diffusion of the magnetic field and the time scale of the diffusion of the magnetic field is determined by,

$$t_D = L^2 \sigma, \tag{3.18}$$

where L is the characteristic length of the system. If we consider $L = 10$ fm which corresponds to the radius of nucleus and $\sigma = 0.3 C_{EM} T \sim 6$ MeV at $T \sim 300$ MeV, the diffusion time becomes about $t_D \sim 3$ fm. However, as mentioned in Ref. [78], in this case the assumption $\sigma \gg 1/t_c \sim 1/t_D$ is not satisfied. We need to solve Eq. (3.16) instead of Eq. (3.17) to discuss more realistic evolution of electromagnetic fields.

If we consider $\boldsymbol{v} \neq \boldsymbol{0}$ case and the magnetic Renolds number $R_m = LV\sigma \gg 1$, which quantifies the ratio of the convection term over the diffusion term, we can approximately take only the convection terms in Eqs. (3.14) and (3.15). This corresponds to the ideal limit of MHD. The equations are given by,

$$\partial_t \boldsymbol{B} = \boldsymbol{\nabla} \times \boldsymbol{v} \times \boldsymbol{B}, \tag{3.19}$$

$$\boldsymbol{E} = -\boldsymbol{v} \times \boldsymbol{B}. \tag{3.20}$$

It is well-known that Eq. (3.19) leads to frozen in theorem for completely conducting plasma. Namely, the magnetic lines are frozen in the plasma elements. More precisely the magnetic flux inside a closed loop defined by plasma elements is conserved as constant. Then, the diffusion of the magnetic field is caused by the expansion of the QGP. To discuss the consequence of Eqs. (3.19) and (3.20), for simplicity, we assume an initial Gaussian transverse entropy density profile for the QGP medium,

$$s(x,y) = s_0 \exp\left(-\frac{x^2}{2a_x^2} - \frac{y^2}{2a_y^2}\right), \tag{3.21}$$

where $a_{x,y}$ are the root-mean-square widths of the Gaussian function. They are taken to be the order of the one or two times nucleus radii. For example, for Au-Au collisions at RHIC, $a_x \sim a_y \sim 3$ fm for $b = 0$ fm, and $a_x \sim 2$ fm, $a_y \sim 3$ fm for $b = 10$ fm. Under the assumption of the Bjorken longitudinal expansion, the longitudinal velocity is given by,

$$v_z = \frac{z}{t}. \tag{3.22}$$

One can solve the ideal transverse hydrodynamic equations and obtain [163],

$$v_x = \frac{c_s^2}{a_x^2} xt, \tag{3.23}$$

$$v_y = \frac{c_s^2}{a_y^2} yt, \tag{3.24}$$

where $c_s = \sqrt{\partial P/\partial e}$ is the sound velocity. Substituting Eqs. (3.23) and (3.24) into Eq. (3.19), we can solve analytically and we can obtain the time dependence of the magnetic field. If we focus on the central region in transverse plane, the $B_y(t, \boldsymbol{r} = 0)$ is written by,

$$B_y(t, \mathbf{0}) = \frac{t_0}{t} \exp\left(-\frac{c_s^2}{2a_x^2}(t^2 - t_0^2)\right) B_y(0, \mathbf{0}). \tag{3.25}$$

This is the consequence of the frozen-in theorem because the areas of the cross-section of the QGP medium expand as $\frac{t}{t_0} \exp\left(\frac{t^2 - t_0^2}{2a_x^2}\right)$ in $x - z$ plane. Namely, the total flux across the reaction plane keeps constant. If we set to $a_x \sim a_y \sim 3$ fm and $c_s^2 \sim 1/3$, we find from Eq. (3.25) that for $t \lesssim 5$ fm $B_y(t)$ evolves approximately as $B_y(t) \propto \frac{t_0}{t} B_y(t_0)$ which corresponds to the magnetized Bjorken flow explained in Subsection 5.2 and is much slower than the $1/t^3$-type decay in the insulating case in the last Subsection 3.2.1.

To explore the discussion beyond these treatments, we need to solve the most general Maxwell equations with the hydrodynamic equation. In this paper, we construct the relativistic resistive magneto-hydrodynamic model for high-energy heavy-ion collisions. The details of our model are introduced in Sec. 6 and 8.

Chapter 4

Relativistic Hydrodynamics

Consider a certain stage after the collision, the system reaches local thermal equilibrium. If the mean free path of the constituent particles is sufficiently shorter than the length of the characterizing systems, later stages of the evolution are described by relativistic hydrodynamics. In this Chapter, We will give an overview of the relativistic hydrodynamic framework.

4.1 Relativistic hydrodynamic equations

The hydrodynamic equations describe the space-time evolution of macroscopic variables such as thermodynamic variables under an assumption of local thermalization. The coupled partial differential equations consist of the energy-momentum conservation law,

$$\partial_\mu T^{\mu\nu} = 0, \tag{4.1}$$

and the conservation of charges,

$$\partial_\mu N_i^\mu = 0 \quad (i = 1, 2, \cdots, n), \tag{4.2}$$

where $T^{\mu\nu}$ is the energy-momentum tensor and N^μ is the charge current vector and d_μ is a covariant derivative. In the point of view the classical field theory, these continuity equations are derived from Noether's theorem. Equation (4.1) is given when the Lagrangian is invariant under the translation of the space-time. In the electrodynamics in which Lagrangian has U(1) gauge symmetry, the conservative charge corresponds to electric charge. The net baryon number is conserved from the U(1) gauge symmetry of the QCD. In this chapter, we ignore the interaction between the QCD matter and electromagnetic fields. We consider the only net baryon number as a conserved charge ($n = 1$).

4.1.1 local rest frame

We assume the local thermal equilibrium at each space point. This means that a reference of frame of the space-time point (x^μ) exists and thermodynamics to fluids

in a small volume element around the x^μ is satisfied. Let us introduce the fluid four-velocity,

$$u^\mu = (\gamma(x), \gamma(x)\boldsymbol{v}(x)) \tag{4.3}$$

$$u^\mu u_\mu = -1, \tag{4.4}$$

and a projection tensor $\Delta^{\mu\nu} = g^{\mu\nu} - u^\mu u^\nu$. We define the local rest frame (LRF) as,

$$u^\mu_{LRF} = (-1, 0, 0, 0), \quad \Delta^{\mu\nu}_{LRF} = \mathrm{diag}(0, 1, 1, 1). \tag{4.5}$$

In high-energy heavy-ion collisions, the mass of particles is not conserved. Then, we cannot define the local rest frame using the flow of mass. Usually, one defines the local rest frame using the flow of the energy density (Landau frame) or the charge density (Eckart frame). In the landau frame [164], the four-velocity is defined as there are no the energy leak current vector,

$$T^\mu_\nu u^\nu_L = e u^\mu_L, \tag{4.6}$$

where e is an energy density. On the other hand, in the Eckart frame [165], one defines the four-velocity,

$$u^\mu_E = \frac{N^\mu}{\sqrt{N^\alpha N_\alpha}} \tag{4.7}$$

4.1.2 Tensor decomposition

One can perform tensor-decomposition for the energy-momentum tensor $T^{\mu\nu}$ and the charge current vector N^μ and any kind of Lorentz tensors. The charge current vector N^μ can be decomposed by the fluid-four velocity and the space-like vector as,

$$N^\mu = n u^\mu + V^\mu, \tag{4.8}$$

where,

$$n = N^\mu u_\mu, \quad \text{(charge density)} \tag{4.9}$$

$$V^\mu = \Delta^{\mu\nu} N_\nu. \quad \text{(charge diffusion vector)} \tag{4.10}$$

The first term in Eq. 4.9 is a time-like component which is parallel to u^μ, whereas the second term is a space-like component in a transverse to u^μ. In the same way, the energy-momentum tensor $T^{\mu\nu}$ can be decomposed in the time-like component and the space-like component for each index,

$$T^{\mu\nu} = e u^\mu u^\nu - (p + \Pi)\Delta^{\mu\nu} + W^\mu u^\nu + W^\nu u^\mu + \pi^{\mu\nu}. \tag{4.11}$$

Here we defined some variables,

$$e = u_\mu T^{\mu\nu} u_\nu, \quad \text{(energy density)} \tag{4.12}$$

$$p_{\mathrm{tot}} = p + \Pi = -\frac{1}{3}\Delta_{\mu\nu} T^{\mu\nu}, \quad \text{(total pressure)} \tag{4.13}$$

$$W^\mu = \Delta^\mu_\alpha T^{\alpha\beta} u_\beta, \quad \text{(energy leak current vector)} \tag{4.14}$$

$$\pi^{\mu\nu} = T^{\langle\mu\nu\rangle} \quad \text{(shear-stress tensor)} \tag{4.15}$$

where p is a thermodynamic pressure, Π is bulk pressure, and Angle brackets denote fir any second-rank tensor,

$$A^{\langle\mu\nu\rangle} = \Delta^{\mu\nu}_{\alpha\beta} A^{\alpha\beta}, \tag{4.16}$$

$$\Delta^{\mu\nu\alpha\beta} = \left[\frac{1}{2}(\Delta^{\mu\alpha}\Delta^{\nu\beta} + \Delta^{\nu\alpha}\Delta^{\mu\beta}) - \frac{1}{3}\Delta^{\mu\nu}\Delta^{\alpha\beta}\right]. \tag{4.17}$$

This tensor becomes symmetric for two indices and transverse to u^μ and u^ν. In the LRF, the energy-momentum tensor and charge current vector are written by,

$$T^{\mu\nu}_{LRF} = \begin{pmatrix} e & W^1 & W^2 & W^3 \\ W^1 & p_{\rm tot} + \pi^{11} & \pi^{12} & \pi^{13} \\ W^2 & \pi^{21} & p_{\rm tot} + \pi^{22} & \pi^{23} \\ W^3 & \pi^{31} & \pi^{32} & p_{\rm tot} + \pi^{33} \end{pmatrix}, \tag{4.18}$$

$$N^\mu = \left(n, V^1, V^2, V^3\right), \tag{4.19}$$

where $\pi^{11} + \pi^{22} + \pi^{33} = 0$ from the traceless condition for the shear-stress tensor.

The derivative operator ∂_μ can also be decomposed as,

$$\partial_\mu = u^\mu (u^\nu \partial_\nu) + \Delta^\nu_\mu \partial_\nu. \tag{4.20}$$

Here we define the time-like component of the derivative operator $D := u^\mu \partial_\mu$ and the space-like component $\nabla_\mu := \Delta^\nu_\mu \partial_\nu$. The time component of the gradient D represents the derivative with respect to the proper time of the fluid element. The space component ∇_μ denotes a spatial derivative in the local rest frame where the derivative operator is written by,

$$\partial_\mu = \left(D, \nabla_1, \nabla_2, \nabla_3\right). \tag{4.21}$$

The derivative D corresponds to the Lagrangian derivative of the non-relativistic hydrodynamics $D/Dt = \partial_t + \mathbf{v} \cdot \nabla$,

$$D = \gamma \left(\partial_t + \mathbf{v}\right) \tag{4.22}$$

$$= \gamma \frac{D}{Dt}. \tag{4.23}$$

Using these operators, one is able to perform the tensor decomposition for the velocity gradient tensor $\partial^\mu u^\nu$:

$$\partial^\mu u^\nu = \frac{1}{2} D(u^\mu u^\nu) + u^{[\mu} D u^{\nu]} + \frac{1}{3}\Delta^{\mu\nu}\theta + \sigma^{\mu\nu} + \omega^{\mu\nu} \tag{4.24}$$

where we have defined the tensors,

$$\theta := \partial_\alpha u^\alpha, \quad \text{(expansion)} \tag{4.25}$$

$$\sigma^{\mu\nu} := \partial^{\langle\mu} u^{\nu\rangle} = \nabla^{(\mu} u^{\nu)} - \frac{1}{3}\Delta^{\mu\nu}\theta, \quad \text{(shear)} \tag{4.26}$$

$$\omega^{\mu\nu} := \nabla^{[\mu} u^{\nu]}. \quad \text{(vorticity)} \tag{4.27}$$

The round and square brackets denote the highlight symmetric and anti-symmetric indices. The first and second terms in Eq. (4.24) are the symmetric and asymmetric

space-time components, respectively. The third term denotes the trace of the space-space components. The fourth and fifth terms represent the symmetric and asymmetric parts of the space-space components. The tensor $\omega^{\mu\nu}$ is called the kinematic vorticity tensor. The tensor $\sigma^{\mu\nu}$, which is called the shear tensor, is a trace-free symmetric part of the derivative of four-velocity. The scalar θ is an expansion rate of the fluid elements which is described by,

$$\theta = \frac{D(\gamma\delta V)}{\gamma\delta V}, \tag{4.28}$$

where $\gamma\delta V$ is the volume of the fluid element observed in the local rest frame. These tensors are satisfied with the following relations,

$$\omega^{(\mu\nu)} = \sigma^{[\mu\nu]} = 0, \tag{4.29}$$
$$\sigma^{\mu}_{\mu} = 0, \tag{4.30}$$
$$\omega^{\mu\nu}u_{\nu} = \sigma^{\mu\nu}u_{\nu} = 0, \tag{4.31}$$
$$\omega^{\mu\nu}\Delta_{\mu\nu} = 0, \tag{4.32}$$
$$\sigma_{\mu\nu}\Delta^{\mu\nu} = 0. \tag{4.33}$$

We can take the local rest frame to vanish some components of the currents. In the Landau frame, the energy leak current in the local rest frame vanishes,

$$W^{\mu} = u_{\alpha}\Delta^{\mu}_{\beta}T^{\alpha\beta} = e\Delta^{\mu}_{\alpha}u^{\alpha} = 0. \tag{4.34}$$

On the other hand, in the Eckart frame, there is no charge diffusion current,

$$V^{\mu} = \Delta^{\mu}_{\alpha}N^{\alpha} = n\Delta^{\mu}_{\alpha}u^{\alpha} = 0. \tag{4.35}$$

One can find the relation between the Landau frame and the Eckart frame,

$$u^{\mu}_{L} = u^{\mu}_{E} + \frac{W^{\mu}}{e+p}, \tag{4.36}$$
$$u^{\mu}_{E} = u^{\mu}_{L} + \frac{V^{\mu}_{L}}{n}. \tag{4.37}$$

In high-energy heavy-ion collisions, a fluid consists of mainly the gluons in the early stage of collisions. As a result, there is only energy and momentum for gluonic fluid as a conserved quantity. Then, in this thesis, we take the Landau frame.

One can define the invariant vector under the transformation of the frame,

$$\nu^{\mu} = W^{\mu} - \frac{e+p}{n}V^{\mu}, \tag{4.38}$$

where nu^{μ} is a heat current vector. The relativistic hydrodynamic equations consist of 6 equations. On the other hand, 15 unknowns exist, $e, p, n, \Pi, \nu^{\mu}, \pi^{\mu\nu}$ and u^{μ}. To close the system of partial differential equations, one is required to reduce the number of unknowns or to provide additional equations.

4.2 Relativistic ideal hydrodynamics

In this section, we consider the assumption that $\pi^{\mu\nu}, \Pi$ and ν^μ are ignored. This assumption implies that the system is close enough to a thermal equilibrium state, and the local value of the energy-momentum tensor and charged current are determined by the thermal equilibrium values. This approximation is called the ideal hydrodynamic approximation.

The energy-momentum tensor and the charged current are written by,

$$T^{\mu\nu} = eu^\mu u^\nu - p\Delta^{\mu\nu}, N^\mu = nu^\mu. \tag{4.39}$$

In the local rest frame, $T^{\mu\nu}$ and N^μ become,

$$T^{\mu\nu} = \begin{pmatrix} e & 0 & 0 & 0 \\ 0 & p & 0 & 0 \\ 0 & 0 & p & 0 \\ 0 & 0 & 0 & p \end{pmatrix}, \tag{4.40}$$

$$N^\mu = \begin{pmatrix} n, & 0, & 0, & 0 \end{pmatrix}. \tag{4.41}$$

The parallel and perpendicular components of the hydrodynamic equations with respect to u^μ are written by,

$$\begin{aligned} 0 &= u_\nu \partial_\mu T^{\mu\nu} && (4.42)\\ &= De + e\theta + e(\partial_\mu u^\mu)u^\nu + pu_\nu u^\mu(\partial_\mu u^\nu) && (4.43)\\ &= De + (e+p)\theta. && (4.44) \end{aligned}$$

and

$$\begin{aligned} 0 &= \Delta^\alpha_\nu \partial_\mu T^{\mu\nu} && (4.45)\\ &= (e+p)Du^\alpha + \nabla^\alpha p. && (4.46) \end{aligned}$$

The first law of the thermodynamics is written by,

$$\begin{aligned} e + p &= Ts + \mu n, && (4.47)\\ de &= Tds + \mu dn. && (4.48) \end{aligned}$$

We can derive the entropy current conservation,

$$\begin{aligned} 0 &= De + (e+p)\theta \\ &= T(Ds + s\theta) + \mu(Dn + n\theta) \\ &= T(Ds + s\theta) \\ &= \partial_\mu(s^\mu). && (4.49) \end{aligned}$$

where we defined the entropy current $s^\mu = su^\mu$. We used Eq. (4.2) when we derived the third equality. As we derive Eq. (4.49), in the relativistic ideal hydrodynamics, the entropy current is conserved.

4.2.1 Relativistic hydrodynamic equation in the Milne coordinates

In high-energy heavy-ion collisions, the fluid strongly expands with respect to the beam axis. The boundary of the fluid at the high space rapidity region rapidly moves along the beam axis with a high velocity that is close to light speed. The relativistic hydrodynamic simulation is numerically unstable and has less accuracy of the calculation near the boundaries. Usually, to avoid these problems, we take the expanding coordinates, so-called the Milne coordinates (τ, x, y, η_s). We have introduced that $\tau = \sqrt{t^2 - z^2}$ is longitudinal proper time and $\eta_s = \frac{1}{2}\ln\frac{t+z}{t-z}$ is space rapidity. Actually, at the LHC and RHIC, the system has approximately invariant under the Lorentz boost transformation with respect to the beam axis [166–172]. If the one-dimensional relativistic hydrodynamic equation is invariant under the Lorentz transformation, there is the analytic solution, which is Bjorken's scaling solution [173] explained in the next Subsection 4.2.2.

In the Milne coordinates, the transformation of the four-velocity from the Cartesian coordinates to the Milne coordinates is represented by,

$$u^\tau = \cosh(\eta_s)u^t - \sinh(\eta_s)u^z, \tag{4.50}$$

$$u^{\eta_s} = \frac{1}{\tau}\left(-\sinh(\eta_s)u^t + \cosh(\eta_s)u^z\right). \tag{4.51}$$

The x and y-components of the four-velocity are invariant under this transformation. The three-velocity v^i is related to the four-velocity $u\mu$,

$$u^\mu = (u^\tau, u^x, u^y, u^{\eta_s}) = \gamma(1, v^x, v^y, v^{\eta_s}), \tag{4.52}$$

where $\gamma = \sqrt{1 - (v^x)^2 - (v^y)^2 - \tau^2(v^{\eta_s})^2}$ is Lorentz factor in the Milne coordinates. The transformation of the three-velocity from the Cartesian coordinates to the Milne coordinates is given by,

$$v^{\eta_s} = \frac{1}{\tau}\frac{-\sinh\eta_s + v^z\cosh\eta_s}{\cosh\eta_s - v^z\sinh\eta_s}, \tag{4.53}$$

$$u^i/u^\tau = \frac{u^i/u^t}{\cosh\eta_s - v^z\sinh\eta_s}, (i = x, y). \tag{4.54}$$

In the Milne coordinates, the metric tensor takes the form,

$$ds^2 = g^{\mu\nu}dx_\mu dx_\nu = -d\tau d\tau + dx^2 + dy^2 + \frac{1}{\tau^2}d\eta_s^2. \tag{4.55}$$

Then, the non-zero Christoffel symbols are derived by,

$$\Gamma^{\eta_s}_{\eta\tau} = \Gamma^{\eta}_{\tau\eta} = \frac{1}{\tau}, \tag{4.56}$$

$$\Gamma^{\tau}_{\eta\eta} = \tau. \tag{4.57}$$

Here, one can derive the hydrodynamic equation (4.1) and (4.2) in the Milne coordinates,

$$\partial_\tau(\tau N^\tau) + \partial_i(\tau N^i) + \partial_{\eta_s}(\tau N^{\eta_s}) = 0, \tag{4.58}$$
$$\partial_\tau(\tau T^{\tau j}) + \partial_i(\tau T^{ij}) + \partial_{\eta_s}(\tau T^{\eta_s j}) = 0, \tag{4.59}$$
$$\partial_\tau(\tau T^{\tau\eta_s}) + \partial_i(\tau T^{i\eta_s}) + \partial_{\eta_s}(\tau T^{\eta_s\eta_s}) = -2T^{\tau\eta_s}, \tag{4.60}$$
$$\partial_\tau(\tau T^{\tau\tau}) + \partial_i(\tau T^{i\tau}) + \partial_{\eta_s}(\tau T^{\eta_s\tau}) = -\tau^2 T^{\eta_s\eta_s}. \tag{4.61}$$

The source terms appear in the energy-momentum conservation law. This represents the fact that the τ and η_s-components of the four-momentum, p^τ and p^{η_s}, are not conserved quantities.

4.2.2 Bjorken flow in high-energy heavy-ion collisions

Here, we introduce the Bjorken's scaling solution [173]. In this subsection, we assume Lorentz boost invariance of the fluid flow. We consider the (1+1)-dimensional Euler equations,

$$(\partial_\tau + v^{\eta_s}\partial_{\eta_s})(\tau e) = -\frac{\tau(e+p)}{u^\tau}\partial_\mu u^\mu + \tau^2(e+p)(u^{\eta_s})^2 - p, \tag{4.62}$$
$$(\partial_\tau + v^{\eta_s}\partial_{\eta_s})v^{\eta_s} = -\frac{1}{(u^\tau)^2(e+p)}\left(\frac{1}{\tau^2}\partial_{\eta_s}p + v^{\eta_s}\partial_\tau p\right) + \tau(v^{\eta_s})^3 - \frac{2}{\tau}v^{\eta_s}. \tag{4.63}$$

In the Cartesian coordinates, the four-velocity, which is invariant under the Lorentz boost transformation, is given by,

$$u^\mu = (\cosh(\eta_s), 0, 0, \sinh(\eta_s)). \tag{4.64}$$

In the Milne Coordinates, the four-velocity becomes simply,

$$u^\mu = (1, 0, 0, 0), \tag{4.65}$$

from Eqs. (4.53) and (4.54). Substituting Eq. (4.65) into Eqs. (4.62) and (4.63), Eular equations reduces to,

$$\partial_\tau e + \frac{e+p}{\tau} = 0, \tag{4.66}$$
$$\partial_{\eta_s} p = 0. \tag{4.67}$$

The second equation becomes,

$$\partial_{\eta_s} T = 0, \tag{4.68}$$

from the thermodynamic relation $dp = sdT + nd\mu$. Using Eq. 4.48, the first equation is reduces,

$$\partial_\tau s + \frac{s}{\tau} = 0. \tag{4.69}$$

From this equation, the entropy is determined by,

$$s\tau = s\tau_0 = const. \tag{4.70}$$

If we take EoS $p = \kappa e$, the evolution of the other thermodynamic quantities is obtained,

$$e = e_0 \left(\frac{\tau_0}{\tau}\right)^{1+\kappa}, \tag{4.71}$$

$$T = T_0 \left(\frac{\tau_0}{\tau}\right)^{\kappa}. \tag{4.72}$$

This relation leads to the initial energy density at the system achieved thermal equilibrium in the high-energy heavy-ion collisions,

$$e_{0,\mathrm{Bj}} = \frac{1}{\pi R^2 \tau_0} \frac{dE_\mathrm{T}}{dy}, \tag{4.73}$$

where R is a system radius, E_T is internal energy, and y is rapidity. If we set to be the initial roper time $\tau_0 = 1$ fm, the initial energy density is estimated 5.5 GeV/fm. This value is enough to reach the QGP phases.

Chapter 5

Relativistic Resistive Magneto-Hydrodynamics

5.1 Basic equations

The conservation laws for the charged current N^μ and for the total energy-momentum tensor of the plasma $T^{\mu\nu}$ in the dynamics of the whole system, are written by,

$$\nabla_\mu N^\mu = 0, \tag{5.1}$$
$$\nabla_\mu T^{\mu\nu} = 0, \tag{5.2}$$

where ∇_μ is the covariant derivative. The electromagnetic fields follow Maxwell equations,

$$\nabla_\mu F^{\mu\nu} = -J^\nu, \tag{5.3}$$
$$\nabla_\mu {}^\star F^{\mu\nu} = 0, \tag{5.4}$$

where $F^{\mu\nu}$ is a Faraday tensor and ${}^\star F^{\mu\nu} = \frac{1}{2}\epsilon^{\mu\nu\rho\sigma}F_{\rho\sigma}$ is it's dual tensor, with $\epsilon^{\mu\nu\rho\sigma} = (-g)^{-1/2}[\mu\nu\rho\sigma]$, $g = \det(g_{\mu\nu})$ and $[\mu\nu\rho\sigma]$ is a completely anti-symmetric tensor. Here we take the metric $\eta^{\mu\nu} = \mathrm{diag}(-1, 1, 1, 1)$ in the Minkowski space-time. If the magnetization and polarization effects are ignored, the energy-momentum tensor of the electromagnetic fields is known to be,

$$T_f^{\mu\nu} = F^{\mu\lambda}F_\lambda^\nu - \frac{1}{4}g^{\mu\nu}F^{\lambda\kappa}F_{\lambda\kappa}, \tag{5.5}$$

and this tensor follows $\nabla_\mu T_f^{\mu\nu} = J_\mu F^{\mu\nu}$, from Maxwell equations. The total energy-momentum tensor is the sum of the contribution of matter and electromagnetic fields $T^{\mu\nu} = T_m^{\mu\nu} + T_f^{\mu\nu}$. The conservation law of the total system Eq. (5.2) gives,

$$\nabla_\mu T_m^{\mu\nu} = -J_\mu F^{\mu\nu}. \tag{5.6}$$

In the ideal limit of the relativistic viscous hydrodynamics and the local equilibrium condition, the energy-momentum tensor and the charge current of fluids are written by,

$$N^\mu = \rho_B u^\mu, \tag{5.7}$$
$$T_m^{\mu\nu} = (e + p)u^\mu u^\nu + pg^{\mu\nu}, \tag{5.8}$$

where u^μ ($u^\mu u_\mu = -1$) is a single fluid four-velocity, ρ_B is the baryon number density, $e = T_m^{\mu\nu} u_\mu u_\nu$ is energy density and $p = \frac{1}{3}\Delta_{\mu\nu} T_m^{\mu\nu}$ is pressure of the fluid. We have introduced the projection tensor $\Delta_{\mu\nu} = g_{\mu\nu} + u_\mu u_\nu$. The Faraday tensor and its dual tensor can be rewritten as,

$$F^{\mu\nu} = u^\mu e^\nu - u^\nu e^\mu + \epsilon^{\mu\nu\lambda\kappa} b_\lambda u_\kappa, \tag{5.9}$$

$$^\star F^{\mu\nu} = u^\mu b^\nu - u^\nu b^\mu - \epsilon^{\mu\nu\lambda\kappa} b_\lambda u_\kappa, \tag{5.10}$$

where,

$$e^\mu = F^{\mu\nu} u_\nu, \ (e^\mu u_\mu = 0), \tag{5.11}$$

$$b^\mu = {}^\star F^{\mu\nu} u_\nu, \ (b^\mu u_\mu = 0), \tag{5.12}$$

are the electric fields and magnetic fields measured in the comoving frame of the fluid. We introduce electric fields E^i and magnetic fields B^i as measured in the laboratory frame. We also define the electric and magnetic fields,

$$e^\mu = (\gamma v_k E^k, \gamma E^i + \gamma \epsilon^{ijk} v_j B_k), \tag{5.13}$$

$$b^\mu = (\gamma v_k B^k, \gamma B^i - \gamma \epsilon^{ijk} v_j E_k), \tag{5.14}$$

where γ is the Lorentz factor of the fluid velocity and v^i is the fluid three-velocity. The projections of $\nabla_\mu T_m^{\mu\nu} = -J_\mu F^{\mu\nu}$ along the perpendicular and parallel directions with respect to u^μ are given by,

$$(e+p) D u^\alpha + (\nabla^\alpha + u^\alpha D) p = g^\alpha_\nu F^{\nu\lambda} J_\lambda - u^\alpha e^\lambda J_\lambda, \tag{5.15}$$

$$De + (e+p)\Theta = e^\lambda J_\lambda, \tag{5.16}$$

where $D = u^\mu \nabla_\mu$ and $\Theta = \nabla_\mu u^\mu$. Equations (5.15) and (5.16) correspond to the equation of motion and energy equation, respectively. They are auxiliary equations that are not solved in our numerical code. But they are useful for the discussion of Bjorken flow in resistive medium, shown in Secs. 7.6 and 7.7. Using the thermodynamic relation $de = Tds + \mu dn$, the entropy production in RRMHD is derived as,

$$T \partial_\mu s^\mu = J^\mu e_\mu, \tag{5.17}$$

where $s^\mu = s u^\mu$ is an entropy current. Since the system of equations Eqs.(5.1)-(5.4) is closed by Ohm's law, we adopt the simplest form of it [174]. In the covariant form, Ohm's law is written by,

$$J^\mu = \sigma F^{\mu\nu} u^\nu + q u^\mu, \tag{5.18}$$

where σ is electrical conductivity and $q = -J^\mu u_\mu$ is electric charge density of the fluid in the comoving frame. When we take ideal limit ($\sigma \to \infty$) of Ohm's law, Eq. (5.18) reduces,

$$e^\mu = 0. \tag{5.19}$$

5.2 Magnetized Bjorken flow

We consider the relativistic boost invariant flow in direction of the z-direction of an ideal magnetized fluid. In magnetized Bjorken flow [175], we assume that the fluid follows

the ultra-relativistic ideal gas EoS, p = e/3. The fluid pressure and energy density are constant in the transverse x-y plane and independent from the space rapidity η_s. The fluid velocity is taken to be a longitudinal boost invariant form $v_z = z/t$, leading to a four-velocity $u^\mu = (\cosh\eta_s, 0, 0, \sinh\eta_s)$. In the Milne coordinate, the fluid four-velocity becomes simply $u^\mu = (1, 0, 0, 0)$ and the comoving derivative and the expansion rate become $D = \partial_\tau$ and $\Theta = 1/\tau$, respectively. The transverse MHD assumes the magnetic field $b^\mu = (0, b^x, b^y, 0)$ orthogonal to the fluid four velocity $u^\mu b_\mu = 0$. In this assumption, one derives from the energy conservation equation Eq. (5.2) [175],

$$\partial_\tau\left(e + \frac{b^2}{2}\right) + \frac{e + p + b^2}{\tau} = 0, \tag{5.20}$$

where $b^2 = b^\mu b_\mu$. However, under the infinite electrical conductivity, Eq. (5.16) reduces,

$$\partial_\tau e + \frac{e + p}{\tau} = 0. \tag{5.21}$$

Then, the evolution equation of the magnetic field is obtained as,

$$\partial_\tau b + b/\tau = 0. \tag{5.22}$$

One derives the analytic solution of these equations by adopting the ultra-relativistic ideal gas EoS, $p = e/3$,

$$e(\tau) = e_0\left(\frac{\tau_0}{\tau}\right)^{4/3}, \tag{5.23}$$

$$b(\tau) = b_0\frac{\tau_0}{\tau}, \tag{5.24}$$

where τ_0 is initial time, e_0 is initial energy density and b_0 is initial magnetic field.

5.3 The longitudinal expansion with acceleration in relativistic resistive magneto-hydrodynamics

We show the longitudinal expansion with acceleration in RRMHD, which is proposed in Ref. [101]. This is a resistive extension of the magnetized Bjorken flow [175]. In this problem, we do not assume the boost invariant flow. However, we suppose that the fluid velocity keeps parallel to the longitudinal direction while the transverse flow is neglected. All the fluid quantities are uniform in the transverse plane. Let us parametrize the four-velocity in (1+1)D as follows:

$$u^\mu = \gamma(1, 0, 0, v_z) = (\cosh Y, 0, 0, \sinh Y), \tag{5.25}$$

where Y is the rapidity and $v_z = \tanh Y$. In the Milne coordinates, u^μ is rewritten by,

$$\begin{aligned} u^\mu &= \left(\cosh(Y - \eta_s), 0, 0, \frac{1}{\tau}\sinh(Y - \eta_s)\right) \\ &= \bar{\gamma}\left(1, 0, 0, \frac{1}{\tau}\bar{v}\right), \end{aligned} \tag{5.26}$$

where $\bar{\gamma} = \cosh(Y - \eta_s)$ and $\bar{v} = \tanh(Y - \eta_s)$. Under this parameterization, the comoving derivative and the expansion rate are given by,

$$D = \bar{\gamma}\left(\partial_\tau + \frac{1}{\tau}\bar{v}\partial_{\eta_s}\right), \tag{5.27}$$

$$\Theta = \bar{\gamma}\left(\bar{v}\partial_\tau Y + \frac{1}{\tau}\partial_{\eta_s} Y\right). \tag{5.28}$$

Then, Eq. (5.16) becomes,

$$(\tau\partial_\tau + \bar{v}\partial_{\eta_s})e + (e+p)(\tau\bar{v}\partial_\tau Y + \partial_{\eta_s} Y) = \bar{\gamma}^{-1}\tau e^\lambda J_\lambda, \tag{5.29}$$

and Eq. (5.15) in the case of $\alpha = \eta_s$ gives,

$$(e+p)Du^{\eta_s} + (\nabla^{\eta_s} + u^{\eta_s}D)p = F^{\eta_s\lambda}J_\lambda - u^{\eta_s}(e^\lambda J_\lambda). \tag{5.30}$$

Here, the derivative of u and p can be calculated as,

$$Du^{\eta_s} = \frac{1}{\tau^2}\bar{\gamma}^2(\tau\partial_\tau + \bar{v}\partial_{\eta_s})Y, \tag{5.31}$$

$$(\nabla^{\eta_s} + u^{\eta_s}D)p = \frac{1}{\tau^2}\bar{\gamma}^2(\tau\bar{v}\partial_\tau + \partial_{\eta_s})p. \tag{5.32}$$

By substituting Eqs. (5.31) and (5.32) into Eq. (5.30), we obtain,

$$\begin{aligned}(e+\quad p)\quad & (\tau\partial_\tau + \bar{v}\partial_{\eta_s})Y + (\tau\bar{v}\partial_\tau + \partial_{\eta_s})p \\ = \quad & \tau^2\bar{\gamma}^{-2}[F^{\eta_s\lambda}J_\lambda - u^{\eta_s}e^\lambda J_\lambda].\end{aligned} \tag{5.33}$$

The four-vectors of the electric and magnetic fields are on the transverse plane, and they are perpendicular to each other,

$$\begin{aligned}e^\mu &= (0, e^x, 0, 0), \\ b^\mu &= (0, 0, b^y, 0).\end{aligned} \tag{5.34}$$

Then, Eqs. (5.29) and (5.33) are reduced to,

$$(\tau\partial_\tau + \bar{v}\partial_\eta)e + (e+p)(\tau\bar{v}\partial_\tau Y + \partial_\eta Y) = \bar{\gamma}^{-1}\tau\sigma e_x^2, \tag{5.35}$$

$$(e+p)(\tau\partial_\tau + \bar{v}\partial_{\eta_s})Y + (\tau\bar{v}\partial_\tau + \partial_{\eta_s})p = \bar{\gamma}^{-1}\tau\sigma e^x b^y. \tag{5.36}$$

From the above assumption in Eqs. (5.26) and (5.34), Maxwell equations are written by,

$$\begin{aligned}\partial_\tau\left[\left(u^\tau b^y + \frac{1}{\tau}e_x u_{\eta_s}\right)\right] + \partial_{\eta_s}\left[\left(u^{\eta_s}b^y - \frac{1}{\tau}e_x u_\tau\right)\right] \\ + \frac{1}{\tau}\left[\left(u^\tau b^y + \frac{1}{\tau}e_x u_{\eta_s}\right)\right] = 0,\end{aligned} \tag{5.37}$$

$$\begin{aligned}\partial_\tau\left[\left(u^\tau e^x + \frac{1}{\tau}b_y u_{\eta_s}\right)\right] + \partial_{\eta_s}\left[\left(u^{\eta_s}e^x - \frac{1}{\tau}b_y u_\tau\right)\right] \\ + \frac{1}{\tau}\left[\left(u^\tau e^x + \frac{1}{\tau}b_y u_{\eta_s}\right)\right] = -\sigma e_x.\end{aligned} \tag{5.38}$$

In Ref. [101], in order to solve these equations, we can take the following Ansatz:

$$e_x(\tau,\eta_s) = -h(\tau,\eta_s)\sinh(Y-\eta_s), \tag{5.39}$$
$$b_y(\tau,\eta_s) = h(\tau,\eta_s)\cosh(Y-\eta_s). \tag{5.40}$$

Under this Ansatz, Eqs. (5.37) and (5.38) give,

$$\partial_\tau h(\tau,\eta_s) + \frac{h(\tau,\eta_s)}{\tau} = 0, \tag{5.41}$$
$$\partial_{\eta_s} h(\tau,\eta_s) + \sigma\tau h(\tau,\eta_s)\sinh(\eta_s - Y) = 0, \tag{5.42}$$

and the solution of Eq. (5.41) is found,

$$h(\tau,\eta_s) = \frac{c(\eta_s)}{\tau}, \tag{5.43}$$

where $c(\eta_s)$ is an arbitrary function. By substituting Eq. (5.43) into Eq. (5.42), we obtain,

$$\sinh(Y-\eta_s) = \frac{1}{\sigma\tau}\frac{\partial_{\eta_s}c(\eta_s)}{c(\eta_s)}, \tag{5.44}$$
$$\cosh(Y-\eta_s) = \sqrt{1+\left(\frac{1}{\sigma\tau}\frac{\partial_{\eta_s}c(\eta_s)}{c(\eta_s)}\right)^2}. \tag{5.45}$$

Then, the fluid rapidity, four-velocity, and electromagnetic fields can be written as,

$$Y = \eta_s + \sinh^{-1}\left(\frac{1}{\sigma\tau}\frac{\partial_{\eta_s}c(\eta_s)}{c(\eta_s)}\right), \tag{5.46}$$
$$u^\tau = \sqrt{1+\left(\frac{1}{\sigma\tau}\frac{\partial_{\eta_s}c(\eta_s)}{c(\eta_s)}\right)^2}, \tag{5.47}$$
$$u^{\eta_s} = \frac{1}{\sigma\tau^2}\frac{\partial_{\eta_s}c(\eta_s)}{c(\eta_s)}, \tag{5.48}$$
$$e_x(\tau,\eta_s) = \frac{1}{\sigma\tau^2}\frac{\partial c(\eta_s)}{\partial\eta_s}, \tag{5.49}$$
$$b_y(\tau,\eta_s) = \frac{c(\eta_s)}{\tau}\times\sqrt{1+\left(\frac{1}{\sigma\tau}\frac{\partial_{\eta_s}c(\eta_s)}{c(\eta_s)}\right)^2}. \tag{5.50}$$

Following to Ref. [101], we take the form of the arbitrary function $c(\eta_s)$ as,

$$c(\eta_s) = c_0\cosh(\alpha\eta_s), \tag{5.51}$$

with the arbitrary parameters α and c_0.

In Ref. [101], they split the conservation equation Eqs. (5.35) and (5.36) into two ordinary differential equations (ODEs) with a given initial condition $e(\tau_0,0) = e_0$. The combination of Eqs. (5.35) and (5.36) with ideal gas EoS $p = \kappa e$ are obtained as,

$$\partial_\tau e(\tau,\eta_s) + \frac{1+\kappa}{\tau}A(\tau,\eta_s)e(\tau,\eta_s) = B(\tau,\eta_s), \tag{5.52}$$
$$\partial_{\eta_s} e(\tau,\eta_s) + H(\tau,\eta_s)e(\tau,\eta_s) = G(\tau,\eta_s), \tag{5.53}$$

where $\kappa = 1/3$ and,

$$A(\tau, \eta_s) = \left(\frac{\partial_{\eta_s} Y(\bar{v} - \kappa) - (\kappa - 1)\tau\bar{v}\partial_\tau Y}{\kappa(\bar{v}^2 - 1)} \right), \tag{5.54}$$

$$B(\tau, \eta_s) = \frac{\sigma(e_x b_y \bar{v} - \kappa e_x^2)}{\kappa\bar{\gamma}(\bar{v}^2 - 1)}, \tag{5.55}$$

$$H(\tau, \eta_s) = \frac{1}{\kappa}((1+\kappa)(\tau\partial_\tau Y + \bar{v}\partial_{\eta_s} Y)) - (1+\kappa)\bar{v}A(\tau, \eta_s), \tag{5.56}$$

$$G(\tau, \eta_s) = \frac{(\sigma\tau)e_x b_y}{\bar{\gamma}\kappa} - \tau\bar{v}B(\tau, \eta_s). \tag{5.57}$$

We numerically solve Eqs. (5.52) and (5.53) to obtain the profile and evolution of energy density. First, we solve Eq. (5.52) as an ODE to find out the τ-dependence of the function e, keeping constant as the variable η_s. Then, we solve Eq. (5.53) with the solution of Eq. (5.52) in each τ as an initial condition of the ODE. As a result, we get numerically the profile of the energy density as the solution of the ODEs.

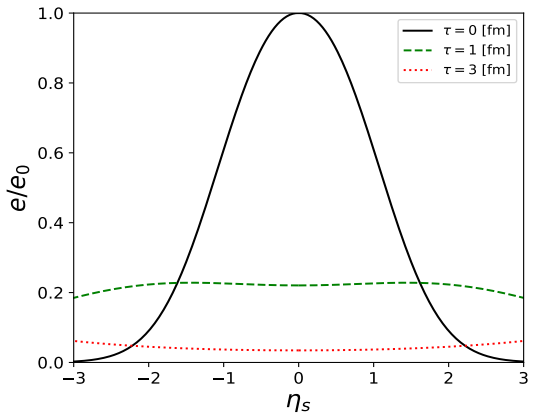

Figure 5.1: (color online) The energy density of the fluid is displayed as a function of τ in the magnetized Bjorken flow.

Figure 5.1 shows the energy density as a function of η_s at $\tau = const.$. The black solid, green dashed, and red dotted lines show the energy density at $\tau = 0.5, 1$ and 3 fm. The energy density expands to the forward and backward rapidity regions. Qualitatively, the energy density takes the form of the Gaussian function when the QGP medium is produced. At late time, the energy density profile becomes a plateau. It is in agreement with Ref. [176]. Figure 5.2 (a) shows the magnetic field in the co-moving frame as a function of η each time. At an early time when the QGP medium is formed, the sum of the magnetic fields created by the colliding nuclei exists. The magnetic field increases with rapidity at a fixed proper time and decreases with increasing proper time in all rapidity regions. Figure 5.2 (b) represents the electric field in the co-moving frame as a function of η each time. At the central rapidity, after the QGP medium is created, the electric field is zero and no external electric field is left on average. However, in the forward and backward rapidity regions, the electric field becomes large since it is produced by the close nucleus at all proper times. In all rapidity regions, the electrical field decays with the proper time.

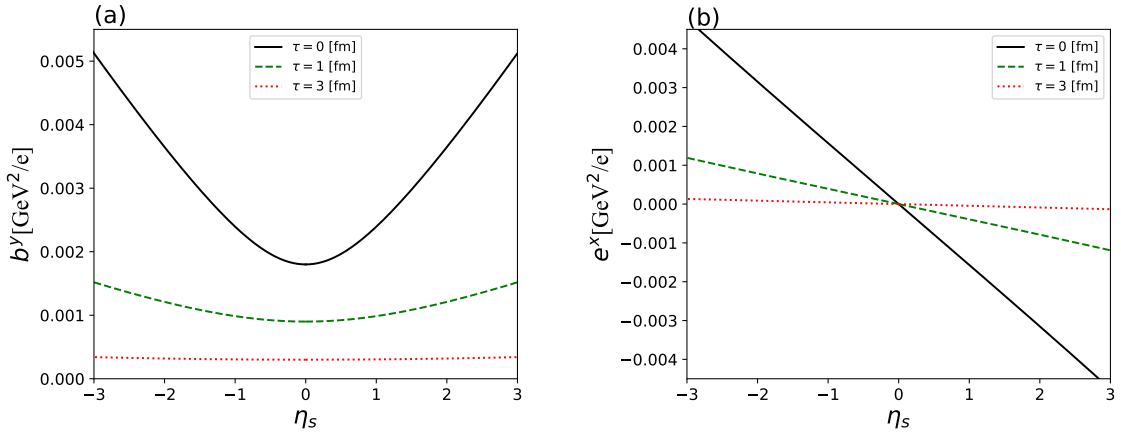

Figure 5.2: (color online) We display (a) the magnetic field component b^y and (b) the electric field component measured in the comoving frame e^x, respectively. The blue solid, red long dashed-dotted and black dashed lines show the numerical results at $t = 0.5, 1.0$, and 3 fm, respectively. The blue, red, and black dotted lines show the semi-analytic solutions of the Eqs. (5.52) and (5.53) at $t = 0.5, 1.0$ and 3.0 fm, respectively.

In Fig. 5.3, the proper time dependence of the energy density in terms of τ for several values of rapidities is shown. As the medium expands to the forward and backward rapidity regions, the energy density rapidly decays. At an early time, the energy density at the forward rapidity region $\eta_s = 2$ increases until $\tau = 0.8$ fm. After that, the energy density decreases with the proper time. The decay of the energy density in the resistive case is faster than the ideal case Eq. (5.23). Figure 5.4 (a) shows the magnetic field as a function of τ for several values of rapidities is shown. The magnetic field decay with the proper time in all rapidities. Different from the electric field, the magnetic field has a non-zero value at the central rapidity. In Fig. 5.4 (b), the time evolution of the electric field for several values of rapidities is illustrated. The electric field decay with the proper time and is a very small value at a late time compared with the magnetic field.

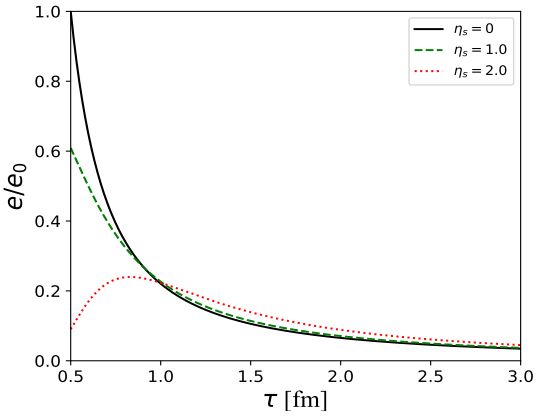

Figure 5.3: (color online) The energy density of the fluid is displayed as a function of τ in the magnetized Bjorken flow.

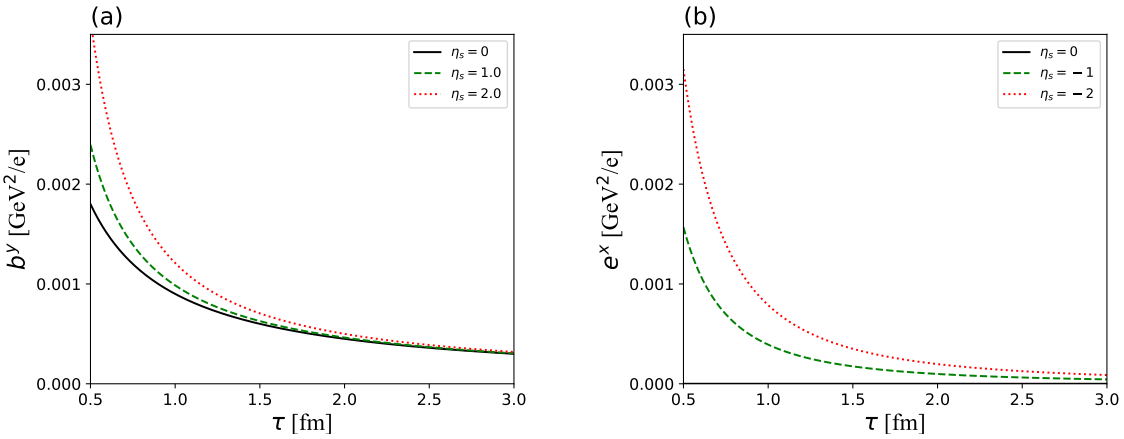

Figure 5.4: (color online) We display (a) the magnetic field component b^y and (b) the electric field component measured in the comoving frame e^x, respectively. The blue solid, red long dashed-dotted and black dashed lines show the numerical results at $t = 0.5, 1.0$, and 3 fm, respectively. The blue, red, and black dotted lines show the semi-analytic solutions of the Eqs. (5.52) and (5.53) at $t = 0.5, 1.0$ and 3.0 fm, respectively.

Chapter 6

Numerical procedure

We now represent governing equations of the RRMHD in a suitable form for numerical calculation. This chapter is based on the associated paper of this thesis [100].

6.1 Metric

We split the spacetime into 3 + 1 components by space-like hypersurface defined as the iso-surfaces of a scalar time function t and assume a metric of the form,

$$ds^2 = -dtdt + g_{ij}dx^i dx^j. \tag{6.1}$$

Since we consider only the Cartesian and the Milne coordinates in this paper, the metric tensor is taken to be $g_{ij} = 0$ $(i \neq j)$. We will take the Cartesian (t, x, y, z) coordinates in Secs. 7.1, 7.2, 7.3, 7.4 and 7.5.1. The Milne (τ, x, y, η_s) coordinates will be considered in Secs. 7.5.2, 7.6 and 7.7, where $\tau := \sqrt{t^2 - z^2}$ is the longitudinal proper-time and $\eta_s := \frac{1}{2}\ln\frac{t+z}{t-z}$ is the space rapidity. We note that in the Cartesian coordinates, the three metric takes $g_{ij} = \mathrm{diag}\{1, 1, 1\}$, with $\sqrt{-g} = 1$, whereas in the Milne coordinates, $g_{ij} = \mathrm{diag}\{1, 1, \tau^2\}$, with $\sqrt{-g} = \tau$. In both coordinates, $\partial_j g_{ik} = 0$, source terms of space-components in conservative equations vanish. However, in the Milne coordinates, where $g_{33} = \tau^2$, the source terms for the energy conservative equation include a non-zero term proportional to $\frac{1}{2}\partial_0 g_{33} = \tau$.

6.2 Constraint equations

Maxwell equations include two Gauss's law,

$$\partial_i(\sqrt{-g}E^i) = \sqrt{-g}q, \tag{6.2}$$

$$\partial_i(\sqrt{-g}B^i) = 0. \tag{6.3}$$

Though Maxwell equations keep that these constraints are satisfied at all time steps, simple integration of Maxwell equations in numerical simulation in a not well-designed scheme does not preserve these conditions because of the numerical error. It leads to unphysical oscillation and numerical simulation crashes in the end for the multi-dimensional calculations. For this reason, a number of numerical techniques are introduced to avoid this problem. In this model, we employ the GLM method to guarantee

these conditions [177–179]. The main idea is that one extends the system by introducing two variables, ψ, and ϕ as the deviation from constraints. One modifies a system of equations to decay or carry the deviation ψ and ϕ out of the computational region by relatively high-speed waves.

For GLM method, we rewrite the Eqs. (5.3) and (5.4) as,

$$\nabla_\nu(F^{\mu\nu} + g^{\mu\nu}\psi) = -\kappa n^\mu \psi + J^\mu, \tag{6.4}$$
$$\nabla_\nu({}^\star F^{\mu\nu} + g^{\mu\nu}\phi) = -\kappa n^\mu \phi, \tag{6.5}$$

where ψ and ϕ are new scalar potentials and κ is a positive constant. In the Cartesian coordinates, we get the telegraph equation for $\boldsymbol{\nabla}\cdot\boldsymbol{E} - q$ and $\boldsymbol{\nabla}\cdot\boldsymbol{B}$,

$$\partial_t^2(\boldsymbol{\nabla}\cdot\boldsymbol{E} - q) + \kappa\partial_t(\boldsymbol{\nabla}\cdot\boldsymbol{E} - q) - \partial_i\partial^i(\boldsymbol{\nabla}\cdot\boldsymbol{E} - q) = 0, \tag{6.6}$$
$$\partial_t^2(\boldsymbol{\nabla}\cdot\boldsymbol{B}) + \kappa\partial_t(\boldsymbol{\nabla}\cdot\boldsymbol{B}) - \partial_i\partial^i(\boldsymbol{\nabla}\cdot\boldsymbol{B}) = 0. \tag{6.7}$$

Consequently, $\boldsymbol{\nabla}\cdot\boldsymbol{E} - q$ and $\boldsymbol{\nabla}\cdot\boldsymbol{B}$ propagate at the speed of light and diffuse exponentially over a timescale $1/\kappa$. In the form of the metric Eq. (6.1), timelike normal vector is taken to be a simple form, $n_\mu = (-1, \mathbf{0})$. The modified divergence free equation of $\boldsymbol{B}$ and the Faraday law is written by,

$$\partial_t(\sqrt{-g}\phi) + \partial_i(\sqrt{-g}B^i) = -\sqrt{-g}\kappa\phi, \tag{6.8}$$
$$\partial_t(\sqrt{-g}B^j) + \partial_i[\sqrt{-g}(\epsilon^{ijk}E_k + g^{ij}\phi)] = 0. \tag{6.9}$$

Also, the modified Gauss's law and Ampere's law are expressed as,

$$\partial_t(\sqrt{-g}\psi) + [\partial_i(\sqrt{-g}E^i) - \sqrt{-g}q] = -\sqrt{-g}\kappa\psi, \tag{6.10}$$
$$\partial_t(\sqrt{-g}E^j) - \partial_i[\sqrt{-g}(\epsilon^{ijk}B_k + g^{ij}\psi)] = -\sqrt{-g}J^j. \tag{6.11}$$

The electric charge density conservation law is obtained by,

$$\partial_t(\sqrt{-g}q) + \partial_i(\sqrt{-g}J^i) = 0. \tag{6.12}$$

6.3 Basic equations

Let us introduce a conservative form which is appropriate for numerical integration of the equations of motion Eqs. (5.1)-(5.2), (6.4)-(6.5) and (6.12),

$$\partial_0\left(\sqrt{-g}\,\boldsymbol{U}\right) + \partial_i\left(\sqrt{-g}\,\boldsymbol{F}^i\right) = \sqrt{-g}\,(\boldsymbol{S}_e + \boldsymbol{S}_s), \tag{6.13}$$

where $\boldsymbol{U}, \boldsymbol{F}^i$, $\boldsymbol{S}_e$ and $\boldsymbol{S}_s$ are the set of conservative variables, fluxes, source terms which is explicitly solved, and source term of stiff part, respectively. These variables have the following components,

$$\boldsymbol{U} = \begin{pmatrix} D \\ \Pi_j \\ \varepsilon \\ B^j \\ E^j \\ q \\ \psi \\ \phi \end{pmatrix}, \quad \boldsymbol{F}^i = \begin{pmatrix} Dv^i \\ T^i_j \\ \Pi^i \\ \epsilon^{jik}E_k + g^{ij}\psi \\ -\epsilon^{jik}B_k + g^{ij}\phi \\ J^i \\ E^i \\ B^i \end{pmatrix},$$

$$\boldsymbol{S_e} = \begin{pmatrix} 0 \\ \frac{1}{2}T^{ik}\partial_j g_{ik} \\ -\frac{1}{2}T^{ik}\partial_0 g_{ik} \\ 0 \\ -qv^i \\ 0 \\ 0 \\ 0 \end{pmatrix}, \quad \boldsymbol{S_s} = \begin{pmatrix} 0 \\ 0 \\ 0 \\ 0 \\ -J_c^i \\ 0 \\ -\kappa\psi \\ -\kappa\phi \end{pmatrix}, \tag{6.14}$$

where the total momentum Π^i, the stress tensor T_{ij} and the total energy density ε are obtained by,

$$D = \gamma\rho, \tag{6.15}$$
$$\Pi_i = (e+p)\gamma^2 v_i + \epsilon_{ijk}E^j B^k, \tag{6.16}$$
$$T_{ij} = (e+p)\gamma^2 v_i v_j + (p+p_{\rm em})g_{ij} - E_i E_j - B_i B_j, \tag{6.17}$$
$$\varepsilon = (e+p)\gamma^2 - p + p_{\rm em}, \tag{6.18}$$
$$J_c^i = \sigma e^i, \tag{6.19}$$

where the electromagnetic energy density $p_{\rm em}$ is written by $p_{\rm em} = \frac{1}{2}(E^2 + B^2)$. We employ the operator splitting method for time integration. Then equation (6.13) can be split into two equations as,

$$\partial_0\left(\sqrt{-g}\,\boldsymbol{U}\right) + \partial_i\left(\sqrt{-g}\,\boldsymbol{F}^i\right) = \sqrt{-g}\boldsymbol{S}_e, \tag{6.20}$$
$$\partial_0\left(\sqrt{-g}\,\boldsymbol{U}\right) = \boldsymbol{S}_s. \tag{6.21}$$

Equation (6.20) can be integrated in time in an explicit manner, while equation (6.21) becomes stiff for large σ and κ. The one-dimensional discretization of Eq. (6.20) can be written by,

$$\boldsymbol{U}_i^{n+1} = \boldsymbol{U}_i^n - \frac{\Delta t}{\Delta x}(\boldsymbol{f}_{i+1/2} - \boldsymbol{f}_{i-1/2}) + \boldsymbol{S}_e\Delta t, \tag{6.22}$$

where Δx is the grid spacing and $\boldsymbol{f}$ is the numerical flux. The subscript i represents the grid point, $x = i\Delta x$, and the subscript n shows the number of the time step, $t = n\Delta t$.

We need to interpolate the primitive variables on the cell surface from those of the cell center to evaluate the numerical flux. We take a second-order accurate scheme for this reconstruction [180] given by,

$$\boldsymbol{P}_{i+1/2}^n = \boldsymbol{P}_i^n + \delta\boldsymbol{P}_i^n/2, \tag{6.23}$$

$$\delta\boldsymbol{P}_i^n = \begin{cases} \mathrm{sign}(\delta\boldsymbol{P}_{i+1/2})\min(|\delta\boldsymbol{P}_{i+1/2}|/2, 2|\delta\boldsymbol{P}_{i+1}|, 2|\delta\boldsymbol{P}_i|) \\ \qquad \text{if} \quad \mathrm{sign}(\Delta\boldsymbol{P}_{i+1})\mathrm{sign}(\Delta\boldsymbol{P}_i) > 0, \\ 0 \quad \text{otherwise}, \end{cases} \tag{6.24}$$

where $\delta\boldsymbol{P}_{i+1/2} = \boldsymbol{P}_{i+1} - \boldsymbol{P}_{i-1}$, $\delta\boldsymbol{P}_{i+1} = \boldsymbol{P}_{i+1} - \boldsymbol{P}_i$, and $\delta\boldsymbol{P}_i = \boldsymbol{P}_i - \boldsymbol{P}_{i-1}$. Then, the numerical flux is calculated by using the Harten-Lax-van Leer (HLL) method [181] given by,

$$\boldsymbol{f}_{i+1/2} = \frac{\lambda^+\boldsymbol{F}(\boldsymbol{U}_{i+1}^n) - \lambda^-\boldsymbol{F}(\boldsymbol{U}_i^n) + \lambda^+\lambda^-(\boldsymbol{U}_{i+1}^n - \boldsymbol{U}_i^n)}{\lambda^+ - \lambda^-}, \tag{6.25}$$

where λ^+ and λ^- denote the maximum and minimum characteristic speeds of the system, respectively. We compute them by the speed of light for simplicity. We employ an analytic method to solve equation (6.21), which is shown in the next subsection in detail. This procedure can avoid the numerical time step becoming too much small.

6.4 Stiff part

In this subsection, we explain how to solve stiff part (6.21), which contains Ampere's law and equations of ϕ and ψ. For Ampere's law, we divide the stiff relaxation equation (6.21) into the perpendicular and parallel directions with respect to v^i and we redefine $E'^i = \sqrt{-g}E^i$ and $B'^i = \sqrt{-g}B^i$,

$$\partial_t(E'^i_\parallel) = -\sigma\gamma[E'^i_\parallel - (E'^k v_k)v^i], \tag{6.26}$$

$$\partial_t(E'^i_\perp) = -\sigma\gamma(E'^i_\perp + \epsilon^{ijk}v_j B'_k), \tag{6.27}$$

where $E'^i_\perp$ denotes a perpendicular direction of the electric field and $E'^i_\parallel$ represents the parallel direction of the electric field. Here, v^i, γ are taken to be constant during small time steps Δt. The solutions of the initial value problem for these relaxation equations are written by,

$$E'^i_\parallel = E'^i_{0\parallel}\exp\{-\sigma\gamma t\}, \tag{6.28}$$

$$E'^i_\perp = E^{*i}_\perp + (E'^i_{0\perp} - E^{*i}_\perp)\exp(-\sigma t/\gamma), \tag{6.29}$$

where $E^{*i}_\perp = -\epsilon^{ijk}v_j B'_k$ and suffix 0 denotes the initial value of E'^i.

For ψ and ϕ, we can integrate the equation (6.21) as

$$\psi' = \psi'_0\exp(-\kappa t), \tag{6.30}$$

$$\phi' = \phi'_0\exp(-\kappa t), \tag{6.31}$$

where, $\psi' = \sqrt{-g}\psi$, $\phi' = \sqrt{-g}\phi$, and suffix 0 expresses the initial value of ψ' and ϕ'.

6.5 Primitive recovery

In our numerical code, we should calculate primitive variables $\{\rho, p, v^i\}$ from evolved conservative variables $\{D, \varepsilon, \Pi_i\}$ in order to evaluate numerical flux at each time steps. To reconstruct primitive variables, we define new variables,

$$\varepsilon' = \varepsilon - p_{em}, \tag{6.32}$$

$$\Pi'_i = \Pi_i - \epsilon_{ijk}E^j B^k, \tag{6.33}$$

where ε' and Π' are the energy density and the momentum of fluid, respectively. The set of the variables $\{D, \varepsilon', \Pi'_i\}$ corresponds to the relativistic ideal fluid conservative variables. Therefore, we can use the ordinal primitive reconstruction method of relativistic hydrodynamic numerical simulation [182] for these variables. We get a one-dimensional equation about the gas pressure as,

$$f(p) := [e(p,\rho) + p]\gamma^2(p) - \varepsilon' - p = 0, \tag{6.34}$$

where,

$$\frac{1}{\gamma^2(p)} = 1 - \frac{\Pi'^i \Pi'_i}{(\varepsilon' + p)^2}, \rho = D/\gamma(p). \tag{6.35}$$

The p and ρ dependence of e is determined by EoS. We solve this equation by the Newton-Raphson algorithm. The other primitive variables are reconstructed as,

$$v^i = \frac{\Pi'^i}{\varepsilon' + p}, \tag{6.36}$$

$$\gamma = \frac{1}{\sqrt{1 - v^i v_i}}, \tag{6.37}$$

$$\rho = D/\gamma, \tag{6.38}$$

$$e = (\varepsilon' + p)/\gamma^2 - p. \tag{6.39}$$

We take into account the ideal gas EoS $p = (\Gamma - 1)(e - \rho)$ in this paper. We note that we set the non-zero ρ in Secs. 7.1, 7.2, 7.3, 7.4, and 7.5.1. In Secs. 7.5.2, 7.6, and 7.7, we take $\rho = 0$.

6.6 Numerical algorithm

Our numerical simulation code is based on finite difference schemes. The advection equation with source term $\boldsymbol{S}_e$ is numerically solved by explicit time integration with second-order TVD Runge-Kutta algorithm [183]. The primitive variables are reconstructed from the cell center to the cell surface by using the second-order accurate scheme [180]. The numerical flux is evaluated by the HLL flux [181]. The stiff part is integrated by the analytic solutions explained in Sec. 6.4. We employ the GLM method to guarantee these conditions [177–179] as keeping two Gauss's laws. The primitive recovery is performed by solving Eq. (6.34) by the Newton-Raphson algorithm explained in Sec. 6.5 [182]. We summarize our numerical algorithm as follows:

- the values of the primitive variables are interpolated from cell center to cell surfaces by using the second-order accurate scheme [180].
- conservative variables $\boldsymbol{U}$ and fluxes $\boldsymbol{F}$ on the cell surface in Eq. (6.13) are evaluated.
- the Riemann problem for numerical fluxes at cell surfaces is solved using the HLL flux [181]
- Equation (6.20) is explicitly integrated using HLL flux.
- the stiff equation (6.21) is integrated by using the analytic solutions expressed by Eqs. (6.28)-(6.29).
- the new primitive variables are reconstructed from the evolved conservative variables by solving Eqs. (6.34)-(6.39).

Chapter 7

Test problem

In this section, several numerical bench-mark tests are performed as the verification of our numerical simulation code. We will take the Minkowski (t, x, y, z) coordinates in Secs. 7.1, 7.2, 7.3 and 7.5.1. The Milne (τ, x, y, η_s) coordinates will be employed in Secs. 7.5.2, 7.6 and 7.7. The CFL constant is taken to be $C_{\rm CFL} = 0.1$ for all test problems. This chapter is also based on the associated paper of this thesis [100].

7.1 Shock tube test problem

In order to test the shock-capturing features of our numerical simulation code, we take into account the simple MHD version of the Brio-Wu test in Ref. [184]. The initial left and right states are taken to be,

$$(\rho^L, p^L, (B^y)^L) = (1.0, 1.0, 1.0) \text{ for } x < 0.5, \tag{7.1}$$

$$(\rho^R, p^R, (B^y)^R) = (0.125, 0.1, -1.0) \text{ for } x \geq 0.5, \tag{7.2}$$

and all the other variables are set to 0.

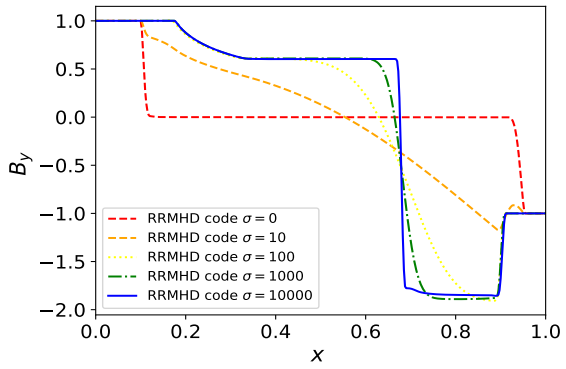

Figure 7.1: (color online) We display the magnetic field B_y at $t = 0.4$ in the Brio-Wu type shock tube test problem.

Figure 7.1 gives the results at $t = 0.4$ for different values of electrical conductivity, $\sigma = 0, 10, 10^2, 10^3, 10^4$. The number of computational grid points is 400. In the solu-

tion with $\sigma = 10^4$, the left-going rarefaction and right-going shock, and a tangential discontinuity between them are found. Our numerical solution with $\sigma = 10^4$ is in good agreement with the solution of relativistic ideal MHD simulations [185]. In addition, our numerical solutions with poor conductivity are similar to the other RRMHD numerical simulations [184, 186]. Especially, the electromagnetic field does not interact with fluid for $\sigma = 0$, so that the electromagnetic waves propagate with light speed. The fronts of the wave should locate at 0.1 and 0.9 for left and right-going waves, respectively. Our results reproduce these analytic ones, although wavefronts slightly have a smooth profile because of the numerical diffusion.

7.2 Large amplitude circularly polarized Alfvén wave

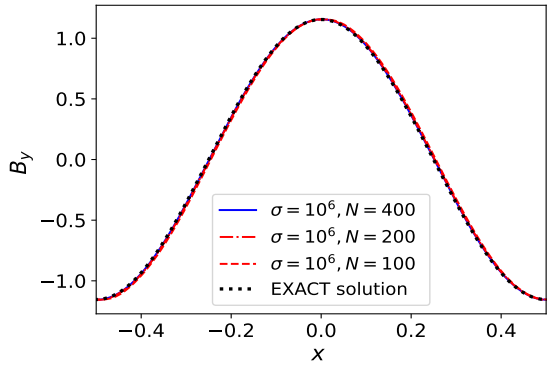

Figure 7.2: (color online) The magnetic field component B_y is shown at $t = 2$ in large amplitude circularly polarized Alfv́en waves.

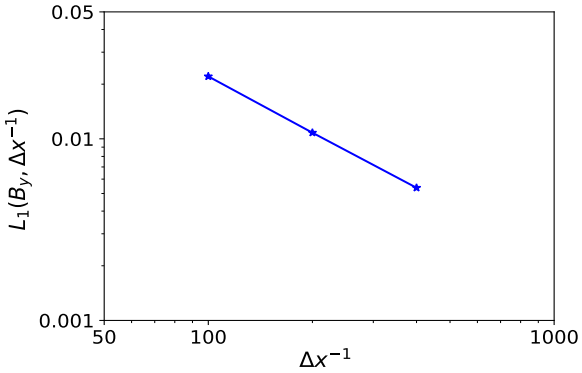

Figure 7.3: The L1 norm errors as a function of the inverse of grid-cell size are shown in large amplitude circularly polarized Alfv́en waves.

We present a test that consists of the propagation of a large amplitude circularly polarized Alfv́en waves along a uniform background magnetic field B_0. The analytical

solution of relativistic ideal MHD is proposed by Ref. [184], which is written by,

$$(B^y, B^z) = \eta_A B^0(\cos[k(x - v_A t)], \sin[k(x - v_A t)]), \tag{7.3}$$

$$(v^y, v^z) = -\frac{v_A}{B_0}(B^y, B^z), \tag{7.4}$$

where $B^x = B_0$, $v_x = 0$, k denotes the wave number and η_A stands for the amplitude of the wave. The special relativistic Alfv́en speed v_A is obtained by,

$$v_A^2 = \frac{2B_0^2}{h + B_0^2(1 + \eta_A^2)} \left[1 + \sqrt{1 - \left(\frac{2\eta_A B_0^2}{h + B_0^2(1 + \eta_A^2)}\right)}\right]^{-1}, \tag{7.5}$$

where $h = (e + p)/\rho$ is the specific enthalpy. We set to the initial variables, $\rho = p = \eta_A = 1$, and $B_0 = 1.1547$. We use an ultra-relativistic ideal gas EoS $p = (\Gamma - 1)(e - \rho)$ with $\Gamma = 2$ and $\rho = \rho_B m$ in this test. From these parameters, the Alfv́en speed is evaluated as $v_A = 1/2$. The computational domain is taken to be $x \in [-0.5, 0.5]$. We take a periodic boundary condition. Since the solution given by Eqs. (7.3) and (7.4) is presented by solving special relativistic ideal MHD equations, the electrical conductivity is taken to be a sufficiently large value, $\sigma = 10^6$, in this test problem.

Figure 7.2 represents our results at $t = 2.0$ (one Alfv́en wave crossing time) for three different numbers of grid points $N = \{100, 200, 400\}$ with the analytical solution. The blue solid and red long dashed-dotted and red dashed lines stand for results with $N = \{100, 200, 400\}$, respectively. The red dotted line denotes the analytical solution. This results with high conductivity σ indicate that our simulation code can handle the ideal MHD limit.

In this problem, we cannot achieve full second-order accuracy. Figure 7.3 shows the $L_1(u, \Delta x^{-1})$ norm errors of the tangential magnetic field B_y of this test as a function of the inverse of grid-cell size Δx^{-1},

$$L_1(u, \Delta x^{-1}) := \sum_i^N |u(x_i; N) - u_{\rm EXACT}(x_i)|\Delta x, \tag{7.6}$$

where $u_{\rm EXACT}(x_i)$ is an exact solution at $x = x_i$. This figure gives that our numerical simulation is nearly 1.3-order convergence. The main reason for this problem is that we perform the second-order Runge-Kutta algorithm with many operator splittings. It makes the time accuracy of our scheme worsen [186]. This is the most difficult to solve in RRMHD since this is the case of large electrical conductivity.

7.3 Self-similar current sheet

We perform the self-similar current sheet test as a highly resistive test problem [178,184] for verification of our simulation code. In this test problem, the magnetic pressure is taken to be much smaller than the pressure of the fluid. The magnetic field has only a tangential component $\mathbf{B} = (0, B(x, t), 0)$ and B(x,t) changes the opposite sign within this current sheet. The background fluid is set to initialize an uniform, $p = const.$ We assume the high conductivity σ, and the diffusion timescale is much longer than the

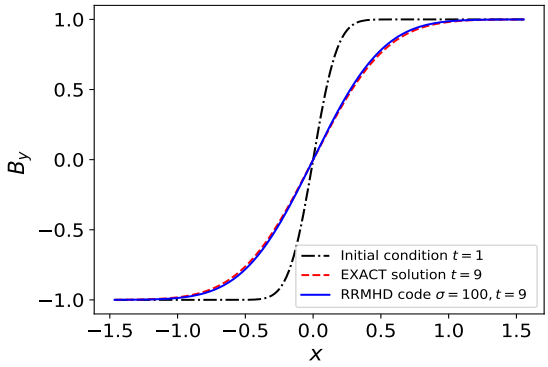

Figure 7.4: (color online) We display the magnetic field component B_y at $t = 9$ in the self-similar current sheet test problem.

light propagation timescale. In this assumption, the evolution equation of the magnetic field becomes simply,

$$\partial_t B - \frac{1}{\sigma}\partial_x^2 B = 0. \tag{7.7}$$

The analytic solution of this equation is written by,

$$B(x,t) = B_0 \mathrm{erf}\left(\frac{1}{2}\sqrt{\frac{\sigma}{\xi}}\right), \tag{7.8}$$

$$\xi = \frac{t}{x^2}, \tag{7.9}$$

where erf denotes the error function. We take the initial condition at $t = 1$ with $p = 50$, $\rho = 1$, $\mathbf{E} = \mathbf{v} = 0$, and $\sigma = 100$. The computational domain is taken to be $x \in [-1.5, 1.5]$, and the number of grid points is set to $N = 200$. Figure 7.4 shows the numerical result at $t = 9$. The red long dashed-dotted line represents the initial condition of B_y at $t = 1$. The blue solid and red dotted lines stand for the numerical result of B_y and the analytical solution at $t = 9$, respectively. This result means that the result of our simulation code is in good agreement with the analytical solution and captures the diffusion of the magnetic field in a highly resistive medium.

7.4 Cylindrical explosion

The symmetric explosions are one of the useful standard tests for RRMHD codes even if there are no exact solutions because the shocks in all possible angles both to the grid and magnetic field are generated. It allows to detection of well-hidden bugs and potential weaknesses. We take the same condition as Ref. [178]. In this test problem, the Cartesian computational domain is set to $x \in [-6.0, 6.0] \times y \in [-6.0, 6.0]$ with 200 equidistant grid points in each direction. The radius of the initial cylinder is taken to be $r = 1$ centered on the origin, where $r = \sqrt{x^2 + y^2}$. The pressure and density of fluid are assumed to be $p = 1$ and $\rho = 0.01$ for $r < 0.8$ and exponentially decay with an increasing radius for $0.8 < r < 1.0$. The fluid in the exterior of the initial

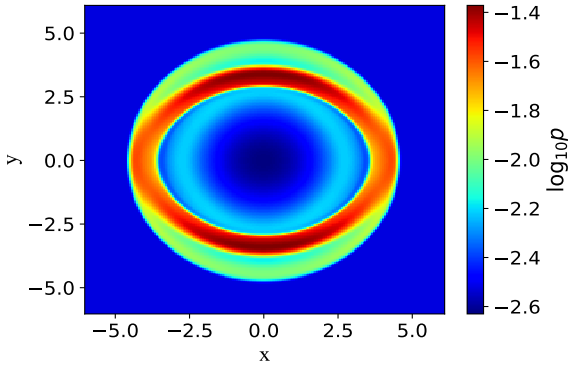

Figure 7.5: The pressure of the fluid is shown at $t = 4$ in the 2D cylindrical explosion test problem.

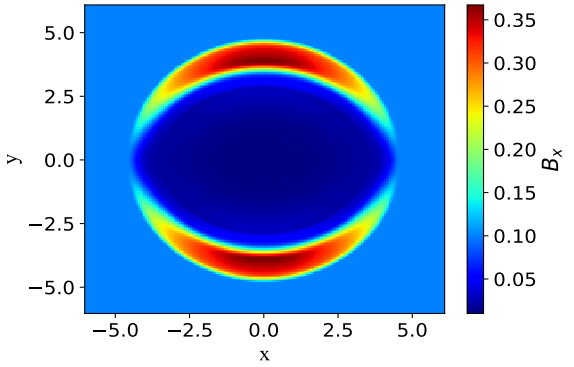

Figure 7.6: The magnetic field component B_x is shown at $t = 4$ in the 2D cylindrical explosion test problem.

cylinder is set to $p = \rho = 0.001$ for $r > 1.0$. We take the initial magnetic field uniform, $\mathbf{B} = (0.1, 0.0, 0.0)$, and the velocity $\mathbf{v} = \mathbf{0}$. The plasma resistivity and decay constant of variables, ψ and ϕ, are taken to be $\eta = 1/\sigma = 0.0018$ and $\eta_d = 1/\kappa = 0.18$. Figure 7.5 and 7.6 stand for the two dimensional solution at $t = 4$ of p and B_x, respectively. These results show that the configuration of P and B_x is consistent with the other RRMHD simulations of the same test problem [178]. We obtain the same results using instead $x - z$ and $y - z$ planes. One can find that there are no artificial waves.

7.5 Rotor test

The resistive rotor test is useful for a calibration multidimensional test for relativistic resistive magneto-hydrodynamic simulations as well as ideal MHD numerical multidimensional codes [187,188]. It allows to detection of the problem of angular momentum loss through torsional Alfv́en waves. We will present the resistive rotor test both of

the Minkowski and the Milne coordinates.

7.5.1 Minkowski coordinates

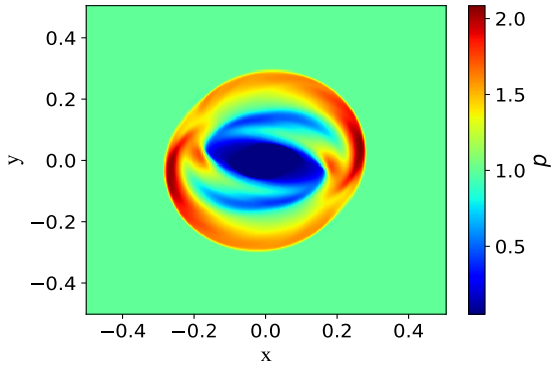

Figure 7.7: The pressure of the fluid is displayed at $t = 0.3$ in the 2D resistive rotor test in the Minkowski coordinates.

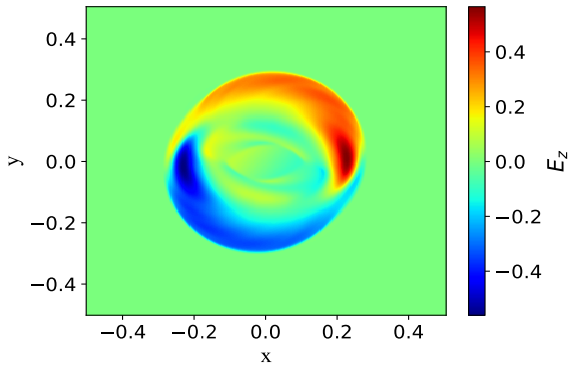

Figure 7.8: The electric field component E_z is shown at $t = 0.3$ in the 2D resistive rotor test in the Minkowski coordinates.

In the resistive rotor test, the Minkowski computational domain is set to $x \in [-6.0, 6.0] \times y \in [-6.0, 6.0]$ with 300 equidistant grid points in each direction. It consists of an initial 2D state where, in a region of radius $r < 0.1$ around the domain center, the density is taken to be $\rho = 10$, and the fluid is rotated with constant angular velocity $\Omega = 8.5$. Outside this region ($r > 0.1$), the medium at rest is uniform ($\rho = 1$). Both the pressure ($p = 1$) and the magnetic field $\mathbf{B} = (1.0, 0, 0)$ are constant in the whole region. The initial electric field is assumed to be the ideal condition, $-\mathbf{v} \times \mathbf{B}$ and the adiabatic index is taken to be $\Gamma = 4/3$.

Figure 7.7 and 7.8 represent snapshots of the gas pressure p and the electric field component E_z at $t = 0.3$ with electrical conductivity $\sigma = 10^6$. These results are consistent with that of other simulation code [187–189]. The same results are reproduced by switching from $x - y$ plane to $x - z$ and $y - z$ planes.

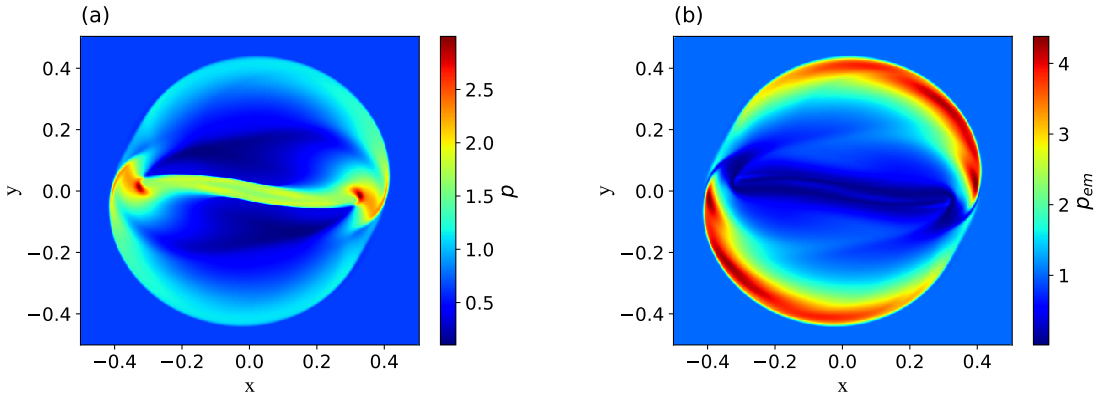

Figure 7.9: (color online) The pressure of fluid (a) and the energy density of the electromagnetic fields (b) are shown at $t = 1.4$ in the 2D resistive rotor test in the Milne coordinates with $\sigma = 10^3$.

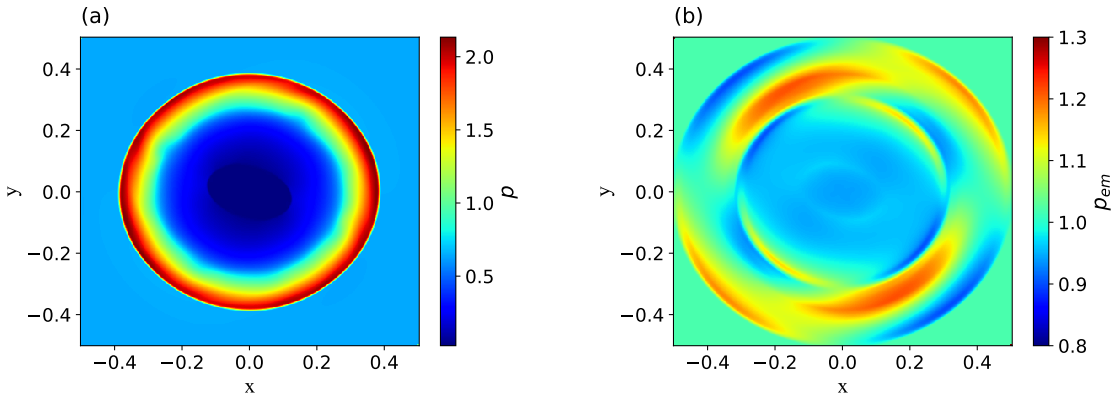

Figure 7.10: (color online) The pressure of fluid (a) and the energy density of the electromagnetic fields (b) are shown at $t = 1.4$ in the 2D resistive rotor test in the Milne coordinates with $\sigma = 10$.

7.5.2 Milne coordinates

In the Milne coordinates, the resistive rotor test is supposed in ECHO-QGP simulation [89].

The computational domain in the Milne coordinates is taken to be $x \in [-6.0, 6.0] \times y \in [-6.0, 6.0]$ with 400 equidistant grid points in each direction. In this test, the EoS is assumed to be the ultra-relativistic ideal gas EoS, $p = e/3$ and we take the fluid density $\rho = 0$ whole computational domain. Then, in this case, the density does not have any influence on the dynamics of the system. Because the EoS is independent of the fluid density, the region inside the disk has an initial pressure of the fluid, $p = 5$, larger than the region outside, $p = 1$, instead of the fluid density. The initial transverse velocity (v_x, v_y) has angular speed $\Omega = 9.7$. The initial longitudinal velocity is taken to be $v_\eta = 0$, which amounts to assuming a longitudinal Bjorken expansion $v^z = z/t$. The initial magnetic field is set to $\mathbf{B} = (2.0, 0, 0)$ and the electric field is assumed to

be $-\mathbf{v} \times \mathbf{B}$.

Figure 7.9 (a) and (b) give the results of p and p_{em} of our simulation code at $t = 1.4$ with $\sigma = 10^3$, respectively. In the Milne coordinates, we find the decay of the pressure of the fluid and magnetic pressure, which appears in the whole computational domain because of the Bjorken expansion of the system. An asymmetrically shaped compression wave by the magnetic field is observed in our results because of the larger initial pressure inside the radius $r < 0.1$ and the motion of rotation of the disk. Our result with $\sigma = 10^3$ has a similar configuration to the result in ECHO-QGP simulation [89]. In the high conductive case, our results capture the features of relativistic ideal MHD. Figure 7.10 (a) and (b) represent the results of p and p_{em} of our simulation code at $t = 1.4$ with $\sigma = 10$, respectively. Our result with $\sigma = 10$, which represents a low conductive case, is less the anisotropy of the azimuthal angle. It indicates that the fluid and electromagnetic fields are weekly coupled. The fluid vorticity does not affect the dynamics of electromagnetic fields. Our result with $\sigma = 10$ is consistent with electromagnetic waves in a poor conductive medium.

7.6 Magnetized Bjorken flow

This test is performed by a comparison with the analytical solution for the evolution of a one-dimensional boost invariant flow, obtained the extension of the model by Bjorken [173] to the case of the transverse ideal MHD [175].

Figure 7.11 and 7.12 give the results of our simulation code in a comparison with analytic solutions. These results reproduce the analytic solutions explained in Subsection 5.2,

$$e(\tau) = e_0 \left(\frac{\tau_0}{\tau}\right)^{4/3}, \tag{7.10}$$

$$b(\tau) = b_0 \frac{\tau_0}{\tau}. \tag{7.11}$$

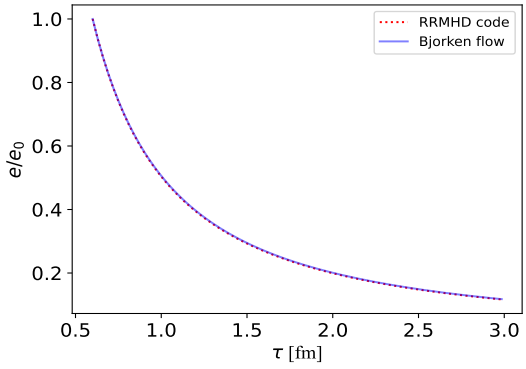

Figure 7.11: (color online) The energy density of the fluid is displayed as a function of τ in the magnetized Bjorken flow.

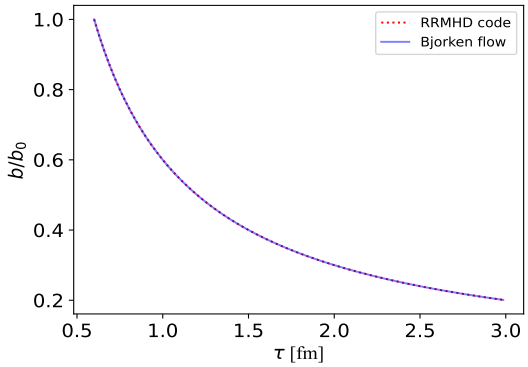

Figure 7.12: (color online) The magnetic field strength as a function of τ is displayed in the magnetized Bjorken flow.

7.7 Accelerating longitudinal expansion

This test problem is supposed in Ref. [101]. This is a resistive version of the magnetized Bjorken flow [175]. The detailed derivation of the semi-analytic solutions is shown in subsection 5.3, but we here show the results. In this problem, we do not suppose the boost invariant flow. We assume that the fluid velocity is facing in direction tof the longitudinal (z-) direction, and the fluid is taken to be uniform on the transverse (x-y) plane. Let us parametrize the four-velocity in the Milne coordinates as follows:

$$\begin{aligned} u^\mu &= \left(\cosh(Y-\eta_s), 0, 0, \frac{1}{\tau}\sinh(Y-\eta_s)\right) \\ &= \bar{\gamma}\left(1, 0, 0, \frac{1}{\tau}\bar{v}\right), \end{aligned} \tag{7.12}$$

where Y is the rapidity with $\bar{\gamma} = \cosh(Y-\eta_s)$ and $\bar{v} = \tanh(Y-\eta_s)$.

The electric and magnetic fields are taken into account in the transverse plane and orthogonal to each other,

$$\begin{aligned} e^\mu &= (0, e^x, 0, 0), \\ b^\mu &= (0, 0, b^y, 0). \end{aligned} \tag{7.13}$$

In Ref. [101], electromagnetic fields are taken to be the following forms,

$$e_x(\tau, \eta_s) = -\frac{c(\eta_s)}{\tau}\sinh(Y-\eta_s), \tag{7.14}$$

$$b_y(\tau, \eta_s) = \frac{c(\eta_s)}{\tau}\cosh(Y-\eta_s). \tag{7.15}$$

The solutions for the rapidity and electromagnetic fields are obtained by,

$$Y = \eta_s + \sinh^{-1}\left(\frac{1}{\sigma\tau}\frac{\partial_{\eta_s}c(\eta_s)}{c(\eta_s)}\right), \tag{7.16}$$

$$u^\tau = \sqrt{1+\left(\frac{1}{\sigma\tau}\frac{\partial_{\eta_s}c(\eta_s)}{c(\eta_s)}\right)^2}, \tag{7.17}$$

$$u^{\eta_s} = \frac{1}{\sigma\tau^2}\frac{\partial_{\eta_s}c(\eta_s)}{c(\eta_s)}, \tag{7.18}$$

$$e_x(\tau,\eta_s) = \frac{1}{\sigma\tau^2}\frac{\partial c(\eta_s)}{\partial\eta_s}, \tag{7.19}$$

$$b_y(\tau,\eta_s) = \frac{c(\eta_s)}{\tau}\times\sqrt{1+\left(\frac{1}{\sigma\tau}\frac{\partial_{\eta_s}c(\eta_s)}{c(\eta_s)}\right)^2}. \tag{7.20}$$

Here $c(\eta_s)$ is an arbitrary function. In this paper, we suppose,

$$c(\eta_s) = c_0\cosh(\alpha\eta_s), \tag{7.21}$$

which is the same as that in Ref. [101]. Here α is defined as an arbitrary constant. The arbitrary constant c_0 is taken to be $0.0018\tau_0$, which is determined by the initial laboratory frame magnetic field strength in the Minkowski coordinates $B^y_L(\tau_0,0) = 0.0018\ \mathrm{GeV}^2/e$.

The energy density is determined by solving the following equations,

$$\partial_\tau e(\tau,\eta_s) + \frac{1+\kappa}{\tau}A(\tau,\eta_s)e(\tau,\eta_s) = B(\tau,\eta_s), \tag{7.22}$$

$$\partial_{\eta_s} e(\tau,\eta_s) + H(\tau,\eta_s)e(\tau,\eta_s) = G(\tau,\eta_s), \tag{7.23}$$

where,

$$A(\tau,\eta_s) = \left(\frac{\partial_{\eta_s}Y(\bar{v}-\kappa) - (\kappa-1)\tau\bar{v}\partial_\tau Y}{\kappa(\bar{v}^2-1)}\right) \tag{7.24}$$

$$B(\tau,\eta_s) = \frac{\sigma(e_x b_y\bar{v} - \kappa e_x^2)}{\kappa\bar{\gamma}(\bar{v}^2-1)}, \tag{7.25}$$

$$H(\tau,\eta_s) = \frac{1}{\kappa}((1+\kappa)(\tau\partial_\tau Y + \bar{v}\partial_{\eta_s}Y)) - (1+\kappa)\bar{v}A(\tau,\eta_s), \tag{7.26}$$

$$G(\tau,\eta_s) = \frac{(\sigma\tau)e_x b_y}{\bar{\gamma}\kappa} - \tau\bar{v}B(\tau,\eta_s). \tag{7.27}$$

Here, we employ the ultra-relativistic ideal gas EoS, $p = \kappa e$ and $\kappa = 1/3$. We numerically solve these differential equations on a grid of points on the (τ,η_s) plane. First, we give the arbitrary function $c(\eta_s)$, which is taken to be a form given in Eq. (7.21). Then the rapidity, four-velocity, and electromagnetic fields are given by Eqs. (7.16)-(7.20). The function $A(\tau,\eta_s)$, $B(\tau,\eta_s)$, $H(\tau,\eta_s)$, and $G(\tau,\eta_s)$ are obtained from Eqs. (7.24)-(7.27). We solve Eq. (7.22) as an ordinary differential equation (ODE) to determine the τ-dependence of the function e, keeping constant as the variable η_s. Then, we solve Eq. (7.23) with the solution of Eq. (7.22) in each τ as an initial condition of the ODE.

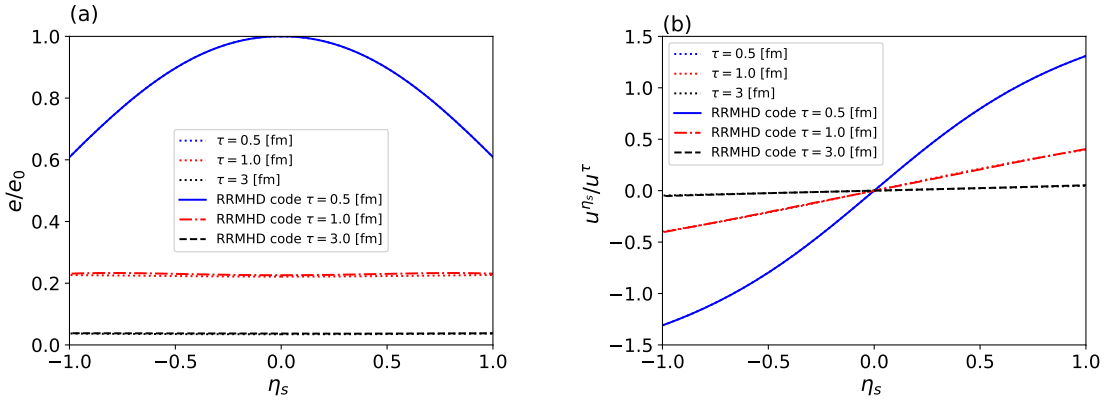

Figure 7.13: (color online) We display (a) the ratio of the energy density of the fluid to the initial energy density and (b) the fluid velocity component v^{η}, respectively. The blue solid, red long dashed-dotted and black dashed lines show the numerical results at $t = 0.5, 1.0$, and 3 fm, respectively. The blue, red, and black dotted lines show the semi-analytic solutions of the Eqs. (7.22) and (7.23) at $t = 0.5, 1.0$ and 3.0 fm, respectively.

The energy density is given as numerical solutions of two ODEs with the initial value of the $e(\tau_0, 0) = e_0$.

Here, we present the RRMHD simulation using the numerical solution of the above ODEs as the initial condition. Since the resistive effect is dominated with small α [101], we take the initial energy density $e_0 = 1.0$ GeV/fm^3, $\alpha = 0.1$, and the electrical conductivity $\sigma = 0.023$ fm^{-1}. The number of grid points in the computational domain $\eta_s \in [-3.0, 3.0]$ is taken to be $N = 200$. We adopt free boundary conditions at $\eta_s = \pm 3.0$. The waves are, however, sometimes reflected at the boundaries and they affect the numerical results. To avoid this problem, we take the boundaries far away from the central region $\eta_s \in [-1.0, 1.0]$ and stop the calculation before the reflected waves reach the central region.

Figures 7.13 and 7.14 show the results of our simulation code in comparison with the semi-analytic solution. Our results are consistent with the semi-analytic solutions. In Fig. 7.13 (a), the energy density decays and expands to the longitudinal direction by the resistive effects. In Fig. 7.13 (b), the fluid velocity in the Milne coordinates has a finite value in the forward and backward rapidity regions and it decays with time. The resistive effect described in Eq. (7.18) is reflected in these features. Our results reproduce this behavior of the longitudinal expansion with acceleration. In Fig. 7.14 (a), the magnetic field component in the comoving frame b^y as a function of η_s is shown. The magnetic field decays with time by the longitudinal expansion similar to the magnetic Bjorken flow in Subsection. 7.6. However, the magnetic field has a non-uniform profile in the η_s direction by the resistive effect, which is different from the magnetic Bjorken flow. Figure 7.14 (b) represents the electric field component measured in the coming frame e^x as a function of η_s. The electric field is a positive value in the backward rapidity region and it decays with rapidity. The electric field changes its sign at $\eta_s = 0$. This feature describes that the electric field is produced by

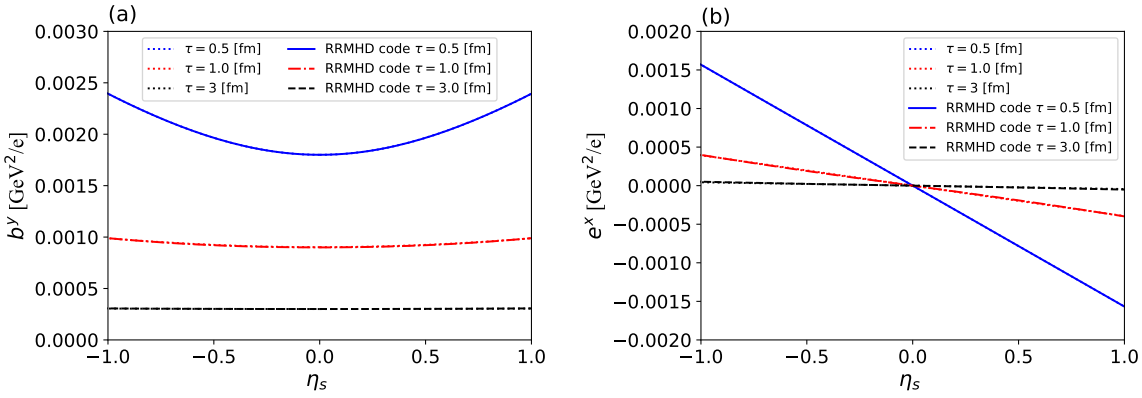

Figure 7.14: (color online) We display (a) the magnetic field component b^y and (b) the electric field component measured in the comoving frame e^x, respectively. The blue solid, red long dashed-dotted and black dashed lines show the numerical results at $t = 0.5, 1.0$, and 3 fm, respectively. The blue, red, and black dotted lines show the semi-analytic solutions of the Eqs. (7.23) and (7.23) at $t = 0.5, 1.0$ and 3.0 fm, respectively.

the two colliding nuclei in high-energy heavy-ion collisions. Our results capture these features and their diffusion which is consistent with the semi-analytic solutions.

7.8 Short summary

We constructed a new RRMHD simulation code in the Milne coordinates which is suitable for study on high-energy heavy-ion collisions. We divide the system of RRMHD equations into two parts, a non-stiff and a stiff part. The primitive variables were reconstructed from the cell center to the cell surface by using the second-order accurate scheme [180]. For the non-stiff part, we computed the numerical flux using the HLL approximated Riemann solver and explicitly integrated the equations in time by the second-order of Runge-Kutta algorithm [183]. For the stiff part in Ampere's law, we performed time integration using semi-analytic solutions to avoid unexpected small time steps. Though Maxwell equations keep that the divergence-free constraints are satisfied at all times, in numerical simulation, the integration of Maxwell equations in a not well-designed scheme does not preserve these conditions because of the numerical error. In order to avoid this problem, we adopted the generalized Lagrange multiplier method to guarantee these conditions [177–179].

We verified the correctness of our algorithm from the comparison between numerical calculations and analytical solutions or the other RMHD simulations such as Brio-Wu type shock tubes, propagation of the large amplitude circularly polarized Alfv́en waves, self-similar current sheet, cylindrical explosion, resistive rotor, and Bjorken flow. In these test problems, our numerical solutions were consistent with analytic solutions or results of the other RRMHD simulations. Furthermore, we studied the accelerating longitudinal expansion of relativistic resistive magneto-hydrodynamics in high-energy heavy-ion collisions in comparison with semi-analytic solutions [101]. Our numerical results were in good agreement with these solutions. We conclude that our numerical simulations capture the characteristic features of dynamics in high-energy heavy-ion collisions.

Chapter 8

Application to Heavy-Ion collsions

We simulate the space-time evolution of the hot and dense medium with electromagnetic fields produced in high-energy heavy-ion collisions, utilizing the RRMHD framework in the Milne coordinates $(\tau, \mathbf{x}_\mathrm{T}, \eta_\mathbf{s})$, which are described by the specific time $\tau = \sqrt{t^2 - z^2}$, the coordinates in the transverse plane $\mathbf{x}_\mathrm{T} = (x, y)$, and the space rapidity $\eta_s = \frac{1}{2} \ln \frac{t+z}{t-z}$. This chapter is based on the associated paper of this thesis [102].

8.1 Initial conditions

8.1.1 medium

The initial conditions for the relativistic magneto-hydrodynamic equations are built up with the Optical Glauber model [190]. Basically, the initial condition of our models is based on the ECHO-QGP simulation [90]. In this model, we assume the initial energy density distribution takes the form,

$$e(\mathbf{x}_\perp, \eta_s) = e_0 M(\mathbf{x}_\perp) f_\mathrm{tilt}(\eta_s), \tag{8.1}$$

where $f_\mathrm{tilt}(\eta_s)$ is a longitudinal profile function with the tilted sources [191]. The energy density distribution in the transverse plane $M(\mathbf{x}_\perp; \mathbf{b})$ is written by,

$$M(\mathbf{x}_\perp; \mathbf{b}) = \frac{(1-\alpha_\mathrm{H}) n_\mathrm{part}(\mathbf{x}_\perp; \mathbf{b}) + \alpha_\mathrm{H} n_\mathrm{coll}(\mathbf{x}_\perp; \mathbf{b})}{(1-\alpha_\mathrm{H}) n_\mathrm{part}(\mathbf{0}; \mathbf{0}) + \alpha_\mathrm{H} n_\mathrm{coll}(\mathbf{0}; \mathbf{0})}, \tag{8.2}$$

where $e_0 = 55$ [GeV/fm^3] [90] is the value of e at $\mathbf{x}_\perp = \mathbf{0}$, $\mathbf{x}_\perp$ is a coordinate in the transverse plane, $\mathbf{b}$ is an impact parameter and $\alpha_\mathrm{H} = 0.05$ [90] is a collision hardness parameter. In the Glauber model, the nuclear thickness function is defined as,

$$T_{A/B}(\mathbf{x}_\perp) = \int_{-\infty}^{\infty} dz \rho_{A/B}(\mathbf{x}_\perp, z), \tag{8.3}$$

and it is normalized,

$$\int_{-\infty}^{\infty} T_{A/B}(\mathbf{x}_\perp) dx_\perp = 1, \tag{8.4}$$

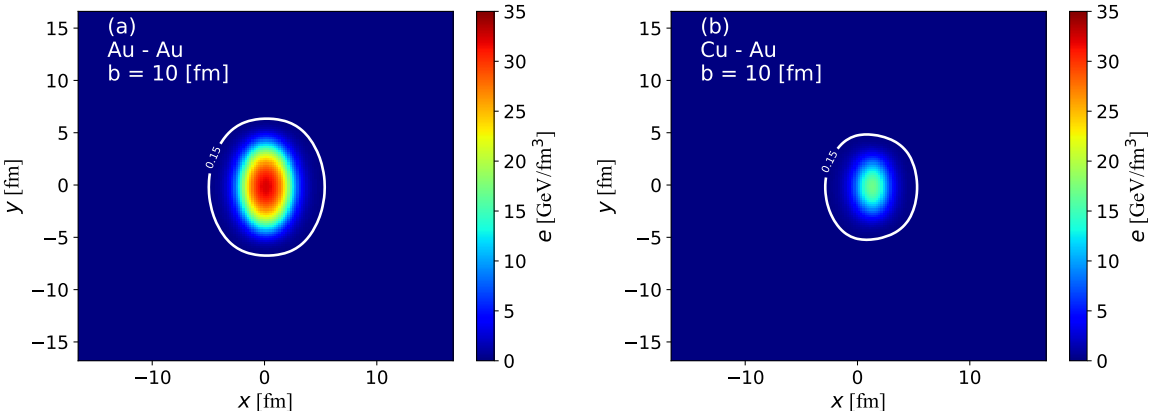

Figure 8.1: (color online) The initial spatial distribution of the energy density in the transverse plane at $\eta_s = 0$. We display the cases of Au-Au collisions (a) and Cu-Au collisions (b), respectively. The white line represents the iso-thermal curve at $e = 0.15$ GeV/fm^3.

where we employ the Woods-Saxon distribution as nuclear density distributions $\rho_{A/B}$,

$$\rho_{A/B} = \frac{\rho^0_{A/B}}{\exp\left\{(\sqrt{x2+y^2+z^2} - R_{A/B})/d_{A/B}\right\} + 1} \tag{8.5}$$

. The number of participant density is the sum of that of the nuclei A and B, $n_{\rm part}(\mathbf{x}_\perp;\mathbf{b}) = n^A_{\rm part}(\mathbf{x}_\perp;\mathbf{b}) + n^B_{\rm part}(\mathbf{x}_\perp;\mathbf{b})$. As the Glauber model, the participant densities of each nuclei are given by,

$$\begin{aligned} n^A_{\rm part} &= A\, T_A(\mathbf{x}_\perp + \mathbf{b}/2)\left[1 - \{1 - T_B(\mathbf{x}_\perp - \mathbf{b}/2)\sigma^{\rm inel}_{\rm NN}\}^B\right], \\ n^B_{\rm part} &= B\, T_B(\mathbf{x}_\perp - \mathbf{b}/2)\left[1 - \{1 - T_A(\mathbf{x}_\perp - \mathbf{b}/2)\sigma^{\rm inel}_{\rm NN}\}^A\right], \end{aligned} \tag{8.6}$$

where A/B is a number of nucleon in nuclei A/B, and $\sigma^{\rm inel}_{\rm NN} = 40$ [mb] [90] is the inelastic nucleon-nucleon cross-section. The number of nucleon-nucleon collision density in the transverse plane is obtained from,

$$n_{\rm coll}(\mathbf{x}_\perp;\mathbf{b}) = AB\ \sigma^{\rm inel}_{\rm NN}\ T_A(\mathbf{x}_\perp + \mathbf{b}/2)T_B(\mathbf{x}_\perp - \mathbf{b}/2). \tag{8.7}$$

In the longitudinal direction, we smoothly connect the energy density distributions to forward and backward rapidity regions from the central rapidity region by function $f_{\rm tilt}(\eta_s)$ with tilted directed flow sources.

For a tilted initial energy density distribution [191], we modify the function $M(\mathbf{x}_\perp;\mathbf{b})$ as below,

$$M(\mathbf{x}_\perp,\eta_s;\mathbf{b}) = \frac{(1-\alpha_{\rm H})W_N(\mathbf{x}_\perp,\eta_s;\mathbf{b}) + \alpha_{\rm H} n_{\rm coll}(\mathbf{x}_\perp;\mathbf{b})}{(1-\alpha_{\rm H})W_N(\mathbf{0},0;\mathbf{0}) + \alpha_{\rm H} n_{\rm coll}(\mathbf{0};\mathbf{0})}, \tag{8.8}$$

and we define the wounded nucleon's weight function W_N as,

$$W_N(\mathbf{x}_\perp,\eta_s;\mathbf{b}) = 2(n^A_{\rm part}(\mathbf{x}_\perp;\mathbf{b})f_-(\eta_s) + n^B_{\rm part}(\mathbf{x}_\perp;\mathbf{b})f_+(\eta_s)), \tag{8.9}$$

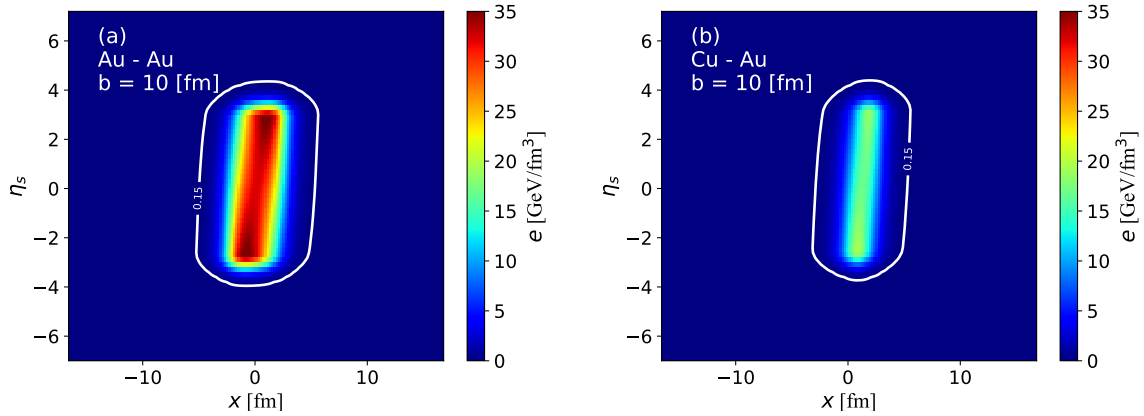

Figure 8.2: (color online) The initial spatial distribution of the energy density in the reaction plane at $y = 0$ fm. We show the cases of Au-Au collisions (a) and Cu-Au collisions (b), respectively. The white line represents the iso-thermal curve at $e = 0.15$ GeV/fm^3.

where,

$$f_-(\eta_s) = \begin{cases} 1 & (\eta_s < -\eta_m) \\ \frac{-\eta_s+\eta_m}{2\eta_m} & (-\eta_m \leq \eta_s \leq \eta_m), \\ 0 & (\eta_s > \eta_m) \end{cases} \tag{8.10}$$

and,

$$f_+(\eta_s) = \begin{cases} 0 & (\eta_s < -\eta_m) \\ \frac{\eta_s+\eta_m}{2\eta_m} & (-\eta_m \leq \eta_s \leq \eta_m), \\ 1 & (\eta_s > \eta_m) \end{cases} \tag{8.11}$$

where $\eta_m = 3.36$ [191] is a parameter. We define also the tilted longitudinal profile function $f_{\rm tilt}(\eta_s)$ as,

$$f_{\rm tilt}(\eta_s) = \exp\left(\frac{-(|\eta_s| - \eta_{\rm flat}/2)^2}{2w_\eta^2}\theta(|\eta_s| - \eta_{\rm flat}/2)\right), \tag{8.12}$$

where $w_\eta = 4.0$ [fm] [90] is a parameter as a width of the gauss function in $f_{\rm tilt}(\eta_s)$ and $\eta_{\rm flat} = 5.9$ [90] is a width of the plateau for the rapidity distribution.

The parameters, $\alpha_{\rm H}, e_0, w_\eta, \eta_{\rm flat}, \tau_0$ and $\sigma_{\rm NN}^{\rm inel}$ in the initial conditions are taken from the ECHO-QGP simulations [90]. We summarize the parameter set for the initial conditions of the energy density in Tab. 8.1. To extract the effects of the difference of the nucleon and charge distributions between symmetric and asymmetric collision systems, we take the same value of the parameters for both of Au-Au and Cu-Au collisions except for the parameters in the Woods-Saxon distribution.

Figure 8.1 (a) shows the initial condition of the energy density in the transverse plane at $\eta_s = 0$ for Au-Au collisions at the impact parameter 10 fm. In Figs. 8.1 (a) and (b), the white lines stand for the iso-thermal surface at $e(\eta_s, \mathbf{x}_{\rm T}) = 0.15$ GeV/fm^3 which corresponds to the freezeout hypersurface at the initial time $\tau_0 = 0.4$ fm [90]. The centers of the Au are located at the points $(x, y) = (\pm 5\text{ fm}, 0\text{ fm})$. The Au located

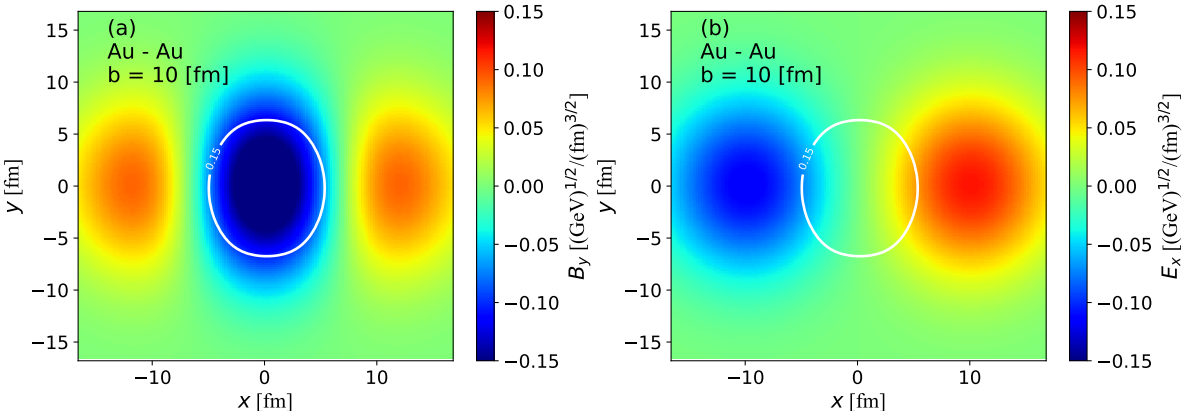

Figure 8.3: (color online) The initial electromagnetic field in the transverse plane at $\eta_s = 0$ for Au-Au collisions. We display the y-component of the magnetic field (a) and the x-component of the electric field (b), respectively. The white line represents the iso-thermal curve at $e = 0.15$ GeV/fm^3.

at $x = 5$ fm ($x = -5$ fm) moves to the forward (backward) rapidity. The almond-shaped hot medium is created by the collision geometry in Au-Au collisions. The initial condition of the energy density in the transverse plane for Cu-Au collisions is shown in Fig. 8.1 (b). The centers of Au and Cu are located at $(x, y) = (-5\text{ fm}, 0\text{ fm})$ and $(5\text{ fm}, 0\text{ fm})$, respectively. The effect of an asymmetric collision system appears in the deformation of the freezeout hypersurface. Figures 8.2 (a) and (b) represent the profiles of the initial energy density in the reaction plane at $y = 0$ fm for Au-Au and Cu-Au collisions, respectively. In Cu-Au collisions, the forward rapidity corresponds to the Cu-going direction. In the both of Au-Au and Cu-Au collisions, the tilted pressure gradient is the source of the directed flow [192].

8.1.2 The initial electromagnetic field

We compute initial electromagnetic fields based on Ref. [81]. We consider the electromagnetic fields produced by the electric charge e moving along parallel to the beam axis ($\hat{\mathbf{z}}$) with velocity v in the laboratory frame by an observer located at $\mathbf{r} = z\hat{\mathbf{z}} + \mathbf{x}_\perp$ in the Minkowski coordinates. Such a system follows the Maxwell equations with the source term of point-charged particles moving in the direction of the beam axis ($\hat{\mathbf{z}}$),

$$\nabla \cdot \boldsymbol{B} = 0, \quad \nabla \times \boldsymbol{E} = -\frac{\partial \boldsymbol{B}}{\partial t}, \tag{8.13}$$

$$\nabla \cdot \boldsymbol{D} = e\delta(z - vt)\delta(\boldsymbol{b}), \tag{8.14}$$

$$\nabla \times \boldsymbol{H} = \frac{\partial \boldsymbol{D}}{\partial t} + \sigma_0 \boldsymbol{E} + ev\hat{\boldsymbol{z}}\delta(z - vt)\delta(\boldsymbol{b}), \tag{8.15}$$

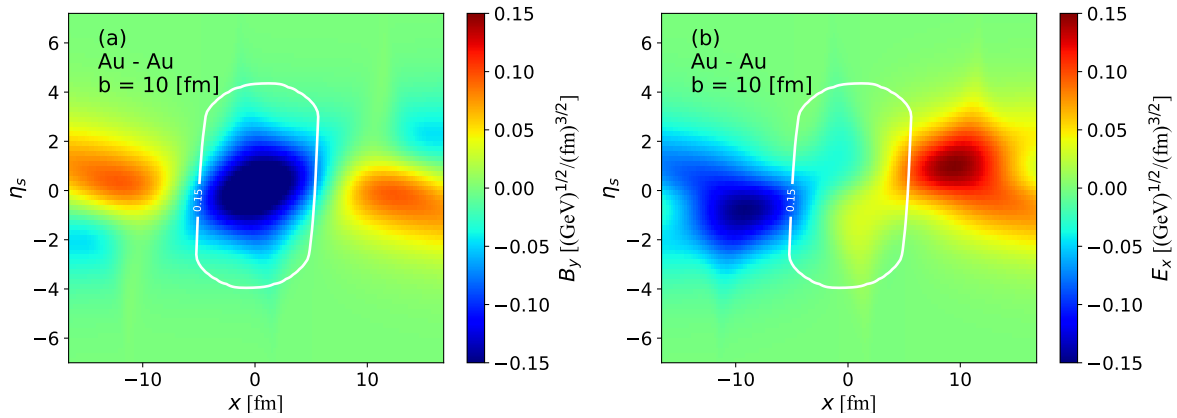

Figure 8.4: (color online) The initial electromagnetic field in the reaction plane at $y = 0$ fm for Au-Au collisions. We show the y-component of the magnetic field (a) and the x-component of the electric field (b), respectively. The white line represents the iso-thermal curve at $e = 0.15$ GeV/fm^3.

where $\boldsymbol{H} = \mu \boldsymbol{B}$ and $\boldsymbol{D} = \epsilon \boldsymbol{E}$. In the case of $\gamma_0 \sigma_0 \mathrm{b} \gg 1$, Maxwell equations reduce simple solutions by integration,

$$
\begin{aligned}
E_r = B_\phi &= \frac{e(\hbar c)^{3/2}}{2\pi} \frac{\mathrm{b}\sigma_0/(\hbar c)}{4x_\pm^2} \exp\left(-\frac{\mathrm{b}^2\sigma_0/(\hbar c)}{4x_\pm}\right), \\
E_z &= -\frac{e(\hbar c)^{3/2}}{4\pi} \frac{x_\pm - \mathrm{b}^2\sigma_0/(4\hbar c)}{\gamma_0^2 x_\pm^3} \exp\left(-\frac{\mathrm{b}^2\sigma_0/(\hbar c)}{4x_\pm}\right),
\end{aligned}
\tag{8.16}
$$

where we define $\gamma_0 = 1/\sqrt{1-v^2}$ and $x_\pm = t \pm v/z$. We assume a constant permittivity $\epsilon = 1$, a constant permeability $\mu = 1$ and a constant finite electrical conductivity $\sigma_0 = 5.8$ MeV [152, 153]. To clarify the dimension of electromagnetic fields, GeV$^{1/2}$/fm$^{3/2}$, we explicitly write $\hbar$ and c. We take the electric charge distribution inside two colliding nuclei as being uniform and spherical for simplicity. Then total electromagnetic fields are derived by integration over the interior of colliding nuclei in each point of our computational grid.

We show the profile of electromagnetic fields in the transverse and reaction planes for Au-Au collisions in Figs. 8.3 and 8.4, respectively. In Fig. 8.3 (a), the y-component of the magnetic field inside the freezeout hypersurface (white line) is stronger than that outside the freezeout hypersurface by the Biot-Savart law. In Fig. 8.3 (b), the x-component of the electric field created by the two nuclei cancels each other and becomes zero around $(x, y, \eta_s) = (0 \text{ fm}, 0 \text{ fm}, 0)$ by the symmetric charge distribution inside colliding nuclei. Figure 8.4 (a) shows the y-component of the magnetic field in the reaction plane. We can see that, inside the medium, the y-component of the magnetic field is finite. Figure 8.4 (b) represents the x-component of the electric field in the reaction plane. If we focus on the behavior of the x-component of the electric field as a function of η_s around $x \sim 0$ fm, it has a positive value in the backward rapidity, decreases with η_s, it becomes vanishing at $\eta_s = 0$, and has a negative value in the forward rapidity. This indicates that the electric field produced by two colliding

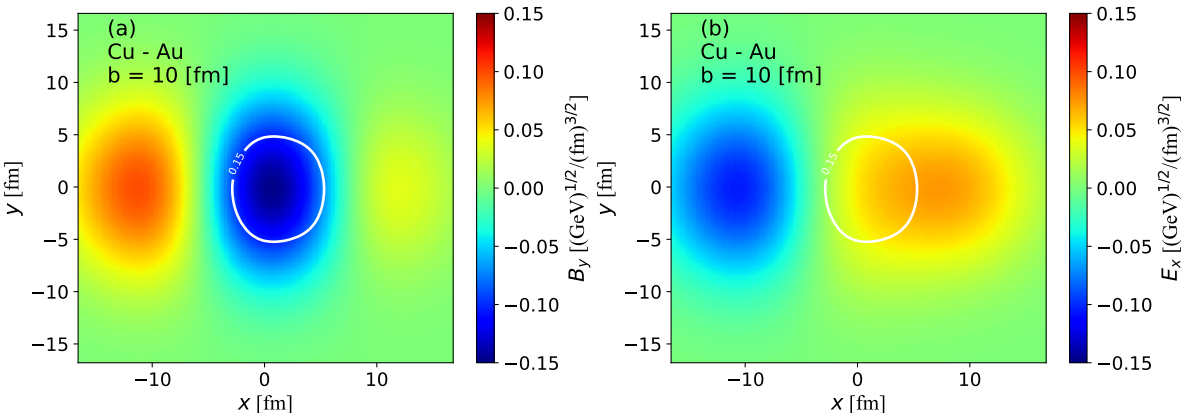

Figure 8.5: (color online) The initial electromagnetic field in the transverse plane at $\eta_s = 0$ for Cu-Au collisions. We show the y-component of the magnetic field (a) and the x-component of the electric field (b), respectively. The white line represents the iso-thermal curve at $e = 0.15$ GeV/fm^3.

nuclei is canceled out of each other at $\eta_s = 0$.

The profiles of electromagnetic fields for Cu-Au collisions are shown in Figs. 8.5 and 8.6. In Fig. 8.5 (a), the distribution of the y-component of the magnetic field is similar to that in Au-Au collisions. However, because of a difference between the charge density of Cu and that of Au, the magnetic field in the $x > 5$ fm region is smaller than that in $x < -5$ fm. In Fig. 8.5 (b), we observe the asymmetric profile of the x-component of the electric field which is different from the symmetric profile in Au-Au collisions in Fig. 8.3 (b). The non-zero x-component of the electric field exists inside the freezeout hypersurface. The magnitude of the electric field on the Cu side ($x > 0$ fm) is larger than that on the Au side ($x < 0$ fm). Figures 8.6 (a) and (b) show the y-component of the magnetic field and the x-component of the electric field in the reaction plane, respectively. The y-component of the magnetic field on the Au side ($x > 7$ fm) is larger than that on the Cu side ($x < -7$ fm) as shown in Fig. 8.5 (a). In Fig. 8.6 (b), the initial electric field in the Au-going ($\eta_s < 0$) side is larger than that in the Cu-going ($\eta_s > 0$) side because the electric field created by the Au is dominated. The characteristic features of the initial electromagnetic field in Cu-Au collisions may affect collective flows, in particular, asymmetric flows.

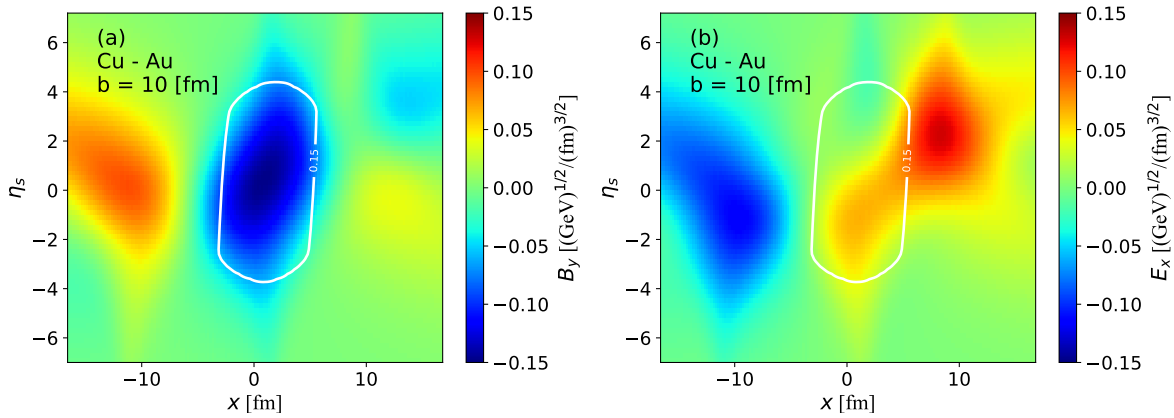

Figure 8.6: (color online) The initial electromagnetic field in the reaction plane at $y = 0$ fm for Cu-Au collisions. We display the y-component of the magnetic field (a) and the x-component of the electric field (b), respectively. The white line represents the iso-thermal curve at $e = 0.15$ GeV/fm^3.

Table 8.1: The values of parameters in the initial conditions for both of $\sqrt{s_{\rm NN}} = 200$ GeV Au-Au and Cu-Au collisions.

Parameter	Description	Value
$\alpha_{\rm H}$	Collision hardness	0.05
e_0	Energy density at $(\eta_s, \mathbf{x}_{\rm T}) = (0, \mathbf{0})$	55 [GeV/fm^3]
η_m	Slope of the tilted source	3.36
$\eta_{\rm flat}$	Width of the plateau	5.9
w_η	Width of the gauss function	0.4
τ_0	Initial time	0.4 [fm]
$\sigma_{\rm NN}^{\rm inel}$	Inelastic cross section	40 [mb]

Chapter 9

Numerical results

The RRMHD simulation have been performed with the tilted initial conditions and electromagnetic fields in Au-Au and Cu-Au collisions at $\sqrt{s_{\rm NN}} = 200$ GeV. We start the RRMHD simulation at initial time $\tau_0 = 0.4$ fm. We terminate the RRMHD simulation when the energy density of all fluid elements becomes below the freezeout energy density $e(\eta_s, \mathbf{x}_{\rm T}) = 0.15$ GeV/fm^3. Sections 9.1, 9.2, and 9.3 are based on the associated paper of this thesis [102]. Section 9.4 is based on the associated paper of this thesis [105].

9.1 Relativistic resistive magneto-hydrodynamic expansion

9.1.1 Fluid velocity

Figures 9.1 (a) and (b) represent the velocity profile ($\langle v_x \rangle$) as a function of η_s in the cases of $\sigma = 0, 1$ and 100 fm^{-1} at time $\tau = 3.0$ fm. The $\langle v_x \rangle$ is written by,

$$\langle v_x \rangle = \frac{\int dydx\gamma e(x, y, \eta_s) v_x(x, y, \eta_s)}{\int dydx\gamma e(x, y, \eta_s)}. \tag{9.1}$$

The blue solid, red dashed, and black dotted lines show $\langle v_x \rangle$ for $\sigma = 100, 1$, and 0 fm^{-1}, respectively. Our simulation with zero electrical conductivity corresponds to the relativistic ideal hydrodynamics simulation.

The case of Au-Au collisions is shown in Fig. 9.1 (a). The η_s-odd dependence of velocity from the tilted sources appeared in $|\eta_s| < 3$ is reflected in the initial conditions. There are only small deviations in the profile of the velocity among the different electrical conductivity. However, if we focus on the rapidity region $|\eta_s| < 2$, the fluid velocity slightly reduces in the forward and backward rapidity regions by the presence of electromagnetic fields with finite electrical conductivity. For example, $\langle v_x \rangle$ with $\sigma = 100$ fm^{-1} is less than that with $\sigma = 0$ fm^{-1}. The deviation of $\langle v_x \rangle$ is evaluated by $|\Delta\langle v_x \rangle| := |\langle v_x \rangle_{\sigma=100\ \text{fm}^{-1}} - \langle v_x \rangle_{\sigma=0\ \text{fm}^{-1}}| \sim 0.7 \times 10^{-3} c$ at $\eta_s = -1.0$.

In Fig. 8.4 (b), the x-component of the electric field is finite in the forward and backward rapidity regions inside the freezeout hypersurface. The energy of this electric field is converted to the fluid energy by the dissipation associated with Ohmic conduction current $\sigma \mathbf{E} \cdot \mathbf{E}$. After just one time step of RRMHD simulation ($\Delta\tau = 0.02$ fm)

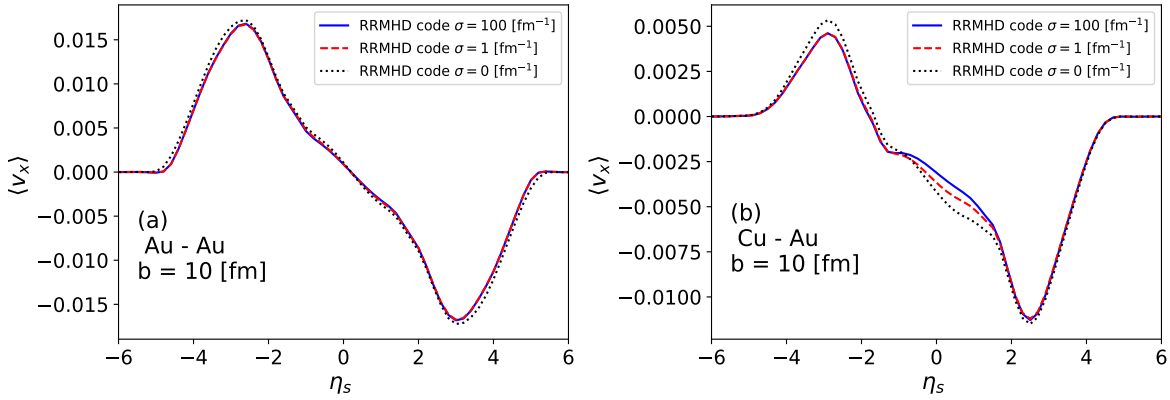

Figure 9.1: (color online) The space averaged flow in the x-direction as a function of space rapidity at $\tau = 3.0$ fm. The blue solid, red dashed, black dotted lines show $\sigma = 100, 1$ and 0 fm^{-1}, respectively. We show the cases of Au-Au collisions (a) and Cu-Au collisions (b) at $\sqrt{s_{\rm NN}} = 200$ GeV.

from the initial condition in Fig. 8.2 (a), this dissipation makes the pressure gradient of the medium around $(\eta_s, x) = (-1.0, 2.5$ fm$)$ with $\sigma = 100$ fm^{-1} flatter ($\sim 0.8 \times 10^{-3}$ GeV/fm^4) than that with $\sigma = 0$ fm^{-1}. If Maxwell's stress tensor is ignored, the RRMHD equations part in Eq. (6.13) contains the equation $\partial_\tau u_x = -\frac{1}{e+p}\partial_x p$. This indicates that $\Delta\langle v_x\rangle$ is proportional to the difference of the pressure gradient. Therefore, the reduction of the fluid velocity is in the same order of the difference of the pressure gradient between $\sigma = 100$ and 0 fm^{-1} cases. We note that the contribution of Maxwell's stress force is very small because the value of plasma beta ($\beta \sim 1000$) is very large in the freezeout hypersurface. Here, the plasma beta is given by the ratio of bulk pressure to magnetic pressure $\beta = p/p_{\rm em}$.

In the zero electrical conductivity case, the evolution of the fluid is completely decoupled with electromagnetic fields. The profile of velocity in the case of zero electrical conductivity (black dotted line) is consistent with the result of the relativistic ideal hydrodynamic simulation in the initial condition with the tilted sources which corresponds to Fig. 6 in Ref. [192].

The Cu-Au collision system case is shown in Fig. 9.1 (b). The clear electrical conductivity dependence of $\langle v_x\rangle$ is observed around $\eta_s = 0$; the amplitude of $\langle v_x\rangle$ reduces with electrical conductivity. Especially, at $\eta_s = 0$, $\langle v_x\rangle$ with $\sigma = 100$ fm^{-1} is less than that with $\sigma = 0$ fm^{-1}. The deviation between $\langle v_x\rangle$ with $\sigma = 100$ fm^{-1} and that with $\sigma = 0$ fm^{-1} is $|\Delta\langle v_x\rangle| \sim 0.0025c$. As shown in the initial condition of the electric field in Fig. 8.5 (b), the electric current is produced in the x-direction. Ohm's law converts the energy from the electric field to the QGP fluid. After just one time step from the initial condition, the pressure gradient of QGP medium around $(\eta_s, x) = (0, 1.5$ fm$)$ with $\sigma = 100$ fm^{-1} becomes flatter (~ 0.003 GeV/fm^4) than that with $\sigma = 0$ fm^{-1}. The deviation of the pressure gradient is in the same order of the reduction of the fluid flow. Furthermore, the effect of Maxwell's stress force is not visible since the plasma beta is also large in the asymmetric collision system.

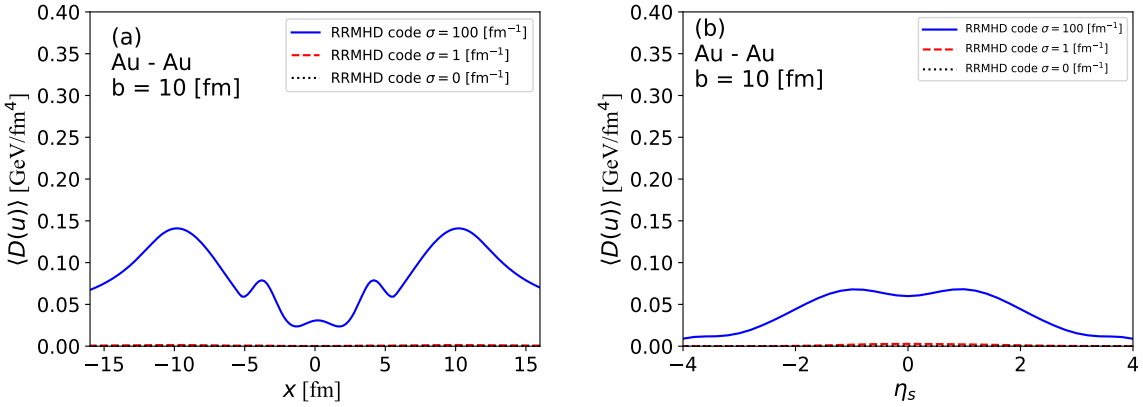

Figure 9.2: (color online) The weighted dissipation measure as a function of x (a) and as a function of η_s (b) for Au-Au collisions at initial time ($\tau = 0.4$ fm). The blue solid, red dashed, and black dotted lines show $\sigma = 100, 1$ and 0 fm^{-1}, respectively.

The electrical conductivity dependence is the consequence of the energy transfer from electromagnetic fields to the fluid by dissipation. This reduction is larger than that of Au-Au collisions. This is because, inside the freezeout hypersurface in Fig. 8.5, the electric field in Cu-Au collisions has a larger value than that in Au-Au collisions. It means that the large Ohmic conduction is induced in asymmetric collisions.

9.1.2 Dissipation measure

To make it clear that the energy transfer from electromagnetic fields to the fluid occurs, we discuss the entropy production by Ohm's law $D(u)$ GeV/fm^4 [193] defined as,

$$\begin{aligned} D(u) &= j^\mu e_\mu \\ &= \gamma[\mathbf{j}\cdot(\mathbf{E}+\mathbf{v}\times\mathbf{B}) - q(\mathbf{v}\cdot\mathbf{E})]. \end{aligned} \tag{9.2}$$

The dissipation measure was first supposed by Ref. [193] to detect the dissipation region in collisionless magnetic reconnection. This quantity denotes the conversion rate of the energy from the electromagnetic field to the QGP fluid by dissipation.

Figure 9.2 (a) represents the weighted spatial distributions of the dissipation measure $D(u)$ as a function of x in Au-Au collisions at $\tau_0 = 0.4$ fm,

$$\langle D(u)\rangle(x) = \frac{\int dyd\eta_s \gamma e(x,y,\eta_s) D(u)(x,y,\eta_s)}{\int dyd\eta_s \gamma e(x,y,\eta_s)}. \tag{9.3}$$

The blue solid, red dashed, and black dotted lines stand for $\langle D(u)\rangle$ in the cases of $\sigma = 100, 1$, and 0 fm^{-1}, respectively. Since the dissipation measure is proportional to the electrical conductivity, the magnitude of $\langle D(u)\rangle$ with $\sigma = 1$ fm^{-1} is 10^{-2} times smaller than that with $\sigma = 100$ fm^{-1}. The timescale of the entropy production by dissipation is determined by the electrical conductivity, $\tau_\sigma \sim 1/\sigma$. In other words, entropy production instantaneously occurs in the high conductive case, whereas it gradually occurs in the resistive case. The $\langle D(u)\rangle$ has a symmetric structure about

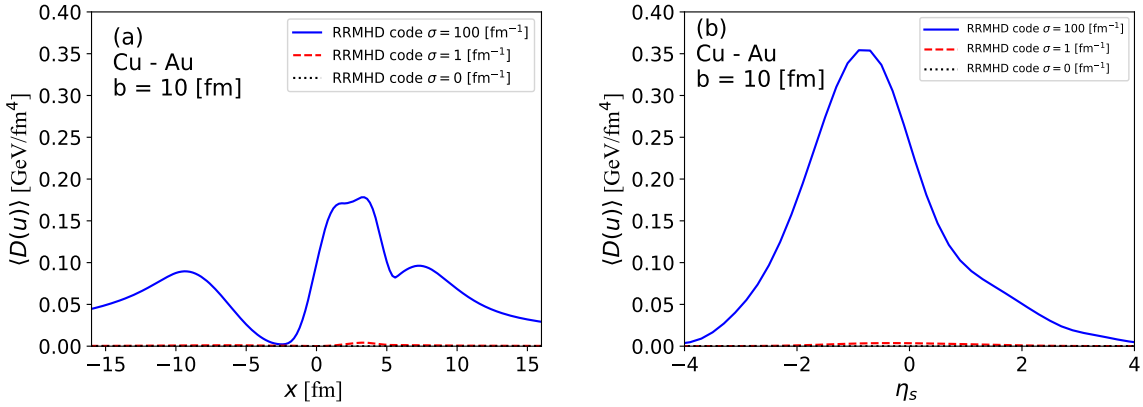

Figure 9.3: (color online) The weighted dissipation measure as a function of x (a) and as a function of η_s (b) for Cu-Au collisions at the initial time ($\tau = 0.4$ fm). The blue solid, red dashed, and black dotted lines show $\sigma = 100, 1$ and 0 fm^{-1}, respectively.

$x = 0$ fm. It becomes small in the region of $|x| < 3$ fm, which is reflected from the small initial electric fields around $x \sim 0$ in Fig. 8.3 (b). Near the freezeout hypersurface around $|x| \sim 5$ fm, there are two peaks. Outside the medium, $|x| \sim 10$ fm, two large peaks exist, however they do not give influence the time evolution of the fluid. The symmetric structure of $\langle D(u)\rangle$ suggests that the converted electromagnetic energy may not affect the directed flow, but may change the amplitude of elliptic flow. In Fig. 9.2 (b), the weighted spatial distributions of the dissipation measure $D(u)$ as a function of η_s,

$$\langle D(u)\rangle(\eta_s) = \frac{\int dydx\gamma e(x,y,\eta_s)D(u)(x,y,\eta_s)}{\int dydx\gamma e(x,y,\eta_s)}, \tag{9.4}$$

are represented. The profile of $\langle D(u)\rangle$ is explained by the integration of the initial electric fields over x in Fig. 8.4 (b).

Figure 9.3 (a) shows the weighted dissipation measure as a function of x in the Cu-Au collision case. In contrast to the symmetric collision, the symmetric structure about $x = 0$ fm is broken. There is the QGP medium in the region of $-2 < x < 5$ fm where $\langle D(u)\rangle$ has only one peak around $x \sim 3$ fm in the side of Cu nucleus. In addition, the value of the peak of $\langle D(u)\rangle$ is larger than the two peaks in the symmetric collision. The structure of the dissipation measure suggests that the energy transfer by Ohm's law alters the behavior of the directed flow. The η_s dependence of the weighted dissipation measure has the asymmetric profile as shown in Fig. 9.3 (b). The largest peak of the dissipation measure is located at $\eta_s \sim -1$.

9.1.3 The freezeout hypersurface

Figures 9.4 (a) and (b) represents the location of the freezeout hypersurface at $(y, \eta_s) = (0\text{fm}, 0)$ in Au-Au and Cu-Au collisions, respectively. The freezeout hypersurface contains the information of the velocity of the QGP medium and the location of the fluid elements of whole time steps at the freezeout process where the hydrodynamic picture

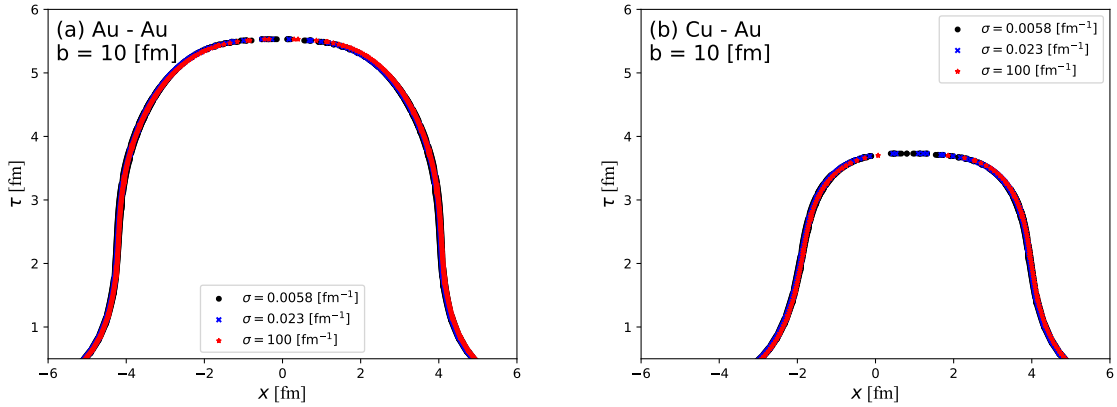

Figure 9.4: (color online) The space averaged flow in the x-direction as a function of space rapidity at $\tau = 3.0$ fm. The blue solid, red dashed, and black dotted lines show $\sigma = 100, 1$ and 0 fm^{-1}, respectively. We show the cases of Au-Au collisions (a) and Cu-Au collisions (b) at $\sqrt{s_{\rm NN}} = 200$ GeV.

is switched to the particle picture. Since the volume of Au nucleus is larger than that of Cu nucleus, the volume of freezeout hypersurface in Au-Au collisions is larger than that in Cu-Au collisions. The black point, the blue cross, and the red star denote the freezeout hypersurface in the cases of $\sigma = 0.0058, 0.023$ and 100fm^{-1}, respectively. These results show that the electrical conductivity dependence is invisible in both of Au-Au and Cu-Au collisions. In Cu-Au collisions, the center of the freezeout hypersurface is shifted to the positive x region. The asymmetry of the Cu-Au collision system is reflected in this behavior. This indicates that the dissipation and Maxwell's stress force do not affect the shape of the freezeout hypersurface. However, as we see in the deviation of the velocity profile, the other variables such as the electric charge density may be affected by electromagnetic fields.

9.2 The elliptic flow

We investigate the effect of electromagnetic fields on the observables. Here, we discuss the elliptic flow of hadrons,

$$v_2(\eta) = \frac{\int dp_{\rm T} d\phi \cos(2\phi) \frac{dN}{dp_{\rm T} d\phi}}{\int dp_{\rm T} d\phi \frac{dN}{dp_{\rm T} d\phi}}, \tag{9.5}$$

where $p_{\rm T} = \sqrt{p_x^2 + p_y^2}$ and ϕ is transverse momentum and an azimuthal angle with respect to the transverse plane, respectively. We terminate the hydrodynamic expansion at $e = 0.15$ GeV/fm^3. To extract the purely hydrodynamic response of electromagnetic fields, we neglect the final state interactions. We adopt the Cooper-Frye formula [139] for the calculation of the hadron distribution from the freezeout hypersurface.

Figures 9.5 (a) and (b) show the elliptic flow of the charged pion as a function of η_s in Au-Au and Cu-Au collisions, respectively. The blue solid, red dashed, and black dotted lines represent the cases of $\sigma = 100, 1$, and 0 fm^{-1}, respectively. The electrical

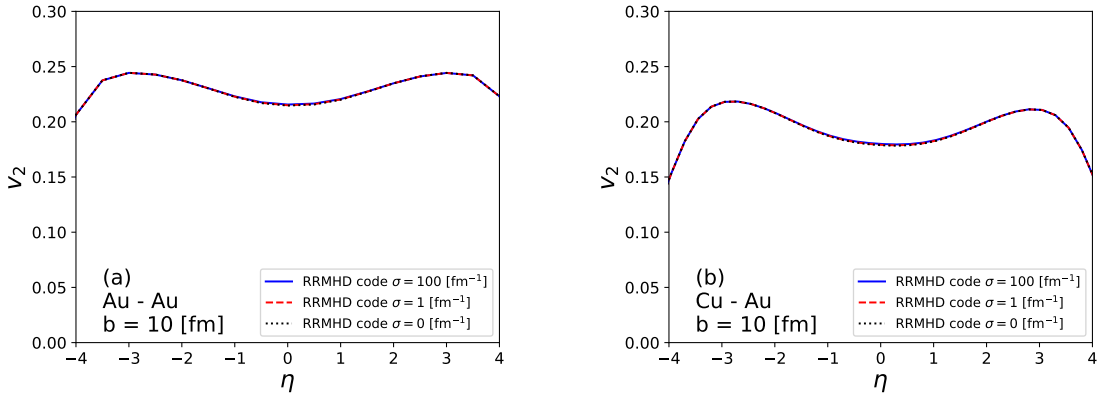

Figure 9.5: (color online) The elliptic flow as a function of rapidity for different electrical conductivities σ. The blue solid, red dashed, and black dotted lines show $\sigma = 100, 1$ and 0 fm^{-1}. We display the cases of (a) Au-Au collisions and (b) Cu-Au collisions at $\sqrt{s_{\rm NN}} = 200$ GeV.

conductivity dependence is invisible. The results with finite electrical conductivity are the same as that in the case of $\sigma = 0$. It indicates that the contribution of electromagnetic fields is very small. The amplitude of the elliptic flow is mainly determined by the pressure gradient of the fluids because the initial energy profile has strong pressure gradients and eccentricity.

9.3 The directed flow

Here, we focus on the directed flow of hadrons,

$$v_1(\eta) = \frac{\int dp_{\rm T} d\phi \cos(\phi) \frac{dN}{dp_{\rm T} d\phi}}{\int dp_{\rm T} d\phi \frac{dN}{dp_{\rm T} d\phi}}. \tag{9.6}$$

Figure 9.6 represents the directed flow for the charged π in Au-Au and Cu-Au collisions. The blue solid, red dashed, and black dotted lines show in the cases of the $\sigma = 100, 1$ and 0 fm^{-1}, respectively. In Fig. 9.6 (a), our results of the directed flow in Au-Au collisions are consistent with the STAR data in 30 - 60 % centrality class [83]. The clear electrical conductivity dependence of the directed flow is not observed. Our calculation in the high conductive case is consistent with the ECHO-QGP simulations with the magnetic field. In the zero conductivity case, the dynamics of the QGP fluid and electromagnetic fields are independent. The directed flow with the zero conductivity case corresponds to that in the relativistic ideal hydrodynamic calculation [192] and that without electromagnetic fields in ECHO-QGP simulations [90].

We show the directed flow for charged π in Cu-Au collisions in Fig. 9.6 (b). The directed flow of our RRMHD simulation exhibits a clear dependence of the electrical conductivity of the QGP. The magnitude of the directed flow decreases with the electrical conductivity. This is a result of the reduction of the velocity in Fig. 9.1 (b). In other words, the mechanism of the reduction of the directed flow is the same as

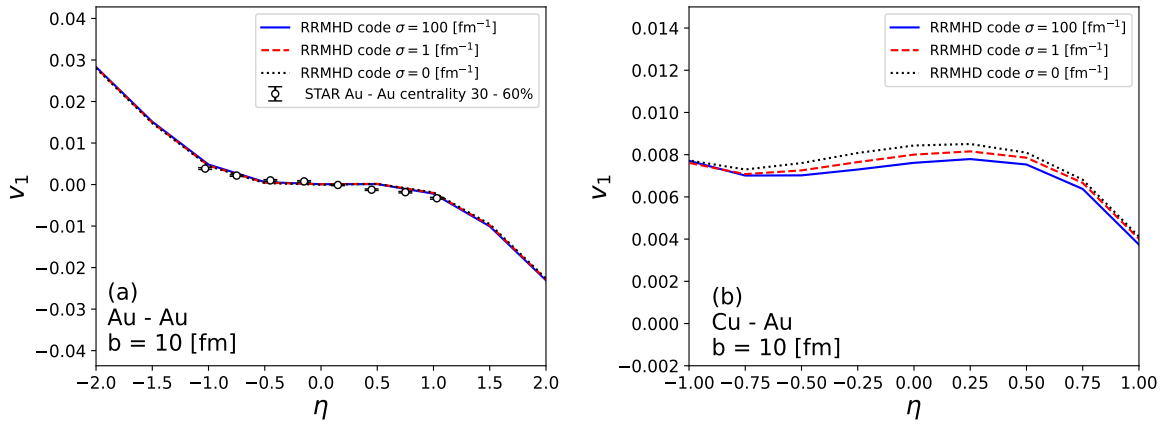

Figure 9.6: (color online) The directed flow as a function of rapidity for different electrical conductivities σ. The blue solid, red dashed, and black dotted lines show $\sigma = 100, 1$ and 0 fm^{-1}. We display the cases of (a) Au-Au collisions and (b) Cu-Au collisions at $\sqrt{s_{\rm NN}} = 200$ GeV.

the suppression of the velocity by entropy production by Ohm's law as shown in the dissipation measure.

We comment on the selection of parameters of the initial condition of the medium in Cu-Au collisions. To perform the simple comparison between the symmetric and asymmetric collision systems, we choose the same parameters of the initial condition as shown in Tab. 8.1. The parameter e_0 which is the energy density at the $\eta_s = 0$ and $\mathbf{x}_{\rm T} = \mathbf{0}$ in Au-Au collisions is larger than that expected in the realistic simulation for Cu-Au collisions. Also, in Cu-Au collisions, the plasma beta in our simulation is larger than that in the realistic case. This means that the effects of electromagnetic fields and the roles of dissipation in asymmetric collision systems are underestimated in this calculation. Moreover, since we assume the constant electrical conductivity in the initial electromagnetic fields, the intensity of initial magnetic fields at the collision time is smaller than that evaluated in vacuum, $|eB_y| \sim 3m_\pi^2$ at RHIC energy [78, 194–196]. For the construction of the realistic initial electromagnetic fields, we need to consider the early dynamics of QCD matter and electromagnetic fields produced by the colliding nuclei. We expect to observe the larger dependence of the electrical conductivity of the QGP with realistic parameter sets. Even though that, we show that the impact of electromagnetic response on the directed flow is the same order of the viscous effect [197]. Thus, the electromagnetic field and the dissipation associated with Ohm's law are important to understand phenomena in high-energy heavy-ion collisions.

The amplitude of the directed flow in our simulation is larger than the data of the STAR experiment. Also, in $-0.75 < \eta < 0.5$, our v_1 slightly increases with η, which is opposite behavior of $v_1(\eta)$ in the experimental data [84]. One of the reasons for the larger value is that, in our calculation, the viscous effects and the final state interactions are ignored. However, the viscous effect itself may not be enough to reduce the amplitude of the directed flow to the STAR data [198]. As a result, the directed flow in RRMHD simulation with finite viscosity of the QGP fluid may get close to the

experimental data. The final state interactions such as the hadron scattering and the resonance decay may smear the hydrodynamic response in the hadron distributions. For the opposite tendency of $v_1(\eta)$, we may find the reason in value of our parameter for η_m and $\eta_{\rm flat}$ which determine the rapidity profile of initial energy density and govern the behavior of the directed flow in the rapidity direction. For simplicity, they are taken to be the same values in Au-Au collisions. For the quantitative comparison with the STAR data, we need to adjust the parameters more carefully. We leave it for our future work. We conclude that the effects of the electromagnetic fields in asymmetric collision systems are sizable enough to be extracted from the experimental data.

9.4 Charge-dependent flow

In this section, we consider the effect of the electric charge distribution produced by the conducting current associated with Ohm's law. In the conducting medium, the electric field is canceled out by the electric charge induced by the Ohm's law. The electric charge is produced at the surface of the medium. It affects the flow near the freezeout hypersurface. Here, we show the charge-odd contribution to the anisotropic flow,

$$\Delta v_n(\eta) = v_n^{h^+}(\eta) - v_n^{h^-}(\eta), (n = 1, 2) \tag{9.7}$$

focusing on the difference between the anisotropic flow of h^+ and that of h^- where h^+ and h^- are the positively and negatively charged hadrons, respectively. The electric charge density distribution on the freezeout hypersurface is reflected in the charge-dependent anisotropic flows. Let us discuss the electric charge density on the freezeout hypersurface in the next subsection before the charge-dependent anisotropic flows. In this section, we take the electrical conductivity $\sigma = 0.023$, which corresponds to σ in three-flavor QGP at $T = 250$ MeV in the lattice QCD calculations in Refs. [152–154, 156]. In order to verify the lattice QCD estimate of the electrical conductivity, we will compare our results and the STAR experimental date. We take also $\sigma = 0.1$ and 0.0058 fm^{-1} as a reference of the relatively higher and lower conductive case, respectively.

9.4.1 Charge distribution on the freezeout hypersurface

Figure 9.7 represents the electric charge distribution on the freezeout hypersurface at $(y, \eta_s) = (0 \text{ fm}, 0)$ in Au-Au collisions. Since the fluid elements at small $|x|$ region have larger energy density than that at large $|x|$ region, they freeze out at a later proper time than that at large $|x|$ region as shown in Fig. 9.4 (a). Then, the electric charge density at small $|x|$ region stands for the electric charge density at a later time than that at large $|x|$ region. The black and blue dashed lines represent the results in the $\sigma = 0.0058, 0.023$ fm^{-1} cases, respectively. The negative charge has two local minimums at $x \sim 4$ fm and -4 fm in both of cases of the electrical conductivity of the QGP fluid. In Fig. 9.7, the negative charges are produced inside the freezeout hypersurface, since the electric field is facing outside the freezeout hypersurface. The location of the local minimums of the electric charge distribution is correlated with the shorter axis of the initial almond shape of the energy density of fluid in Fig. 8.1

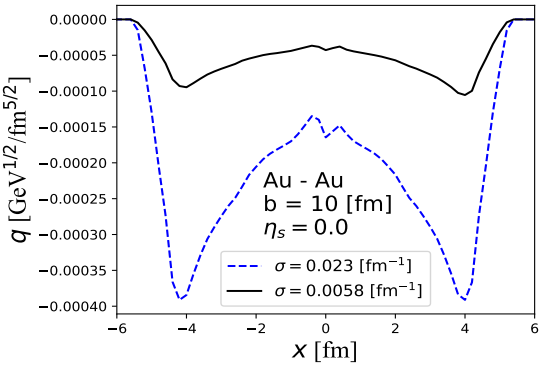

Figure 9.7: (color online) The charge distributions on the freezeout hypersurface as a function of x at $\eta_s = 0.0$ and $y = 0.0$ fm in Au-Au collisions. The black solid and blue dashed lines represent the cases of $\sigma = 0.0058$ and 0.023 fm^{-1}, respectively.

(a). As a result, the momentum of the negatively charged hadrons on the freezeout hypersurface is correlated with the elliptic momentum anisotropy of the fluid induced by the almond-shaped pressure gradient on the freezeout hypersurface. On the other hand, the production of positively charged hadrons reduces due to the negative chemical potential of electric charge on the freezeout hypersurface. Then, this structure of the electric charge distribution may enhance the charge-odd contribution to the elliptic flow of charged hadrons.

Figures 9.8 (a) and (b) represent the electric charge distribution on the freezeout hypersurface at $(y, \eta_s) = (0 \text{ fm}, -1)$ and $(0 \text{ fm}, +1)$ in Au-Au collisions, respectively. As shown in Fig. 8.4 (b), in $\eta_s > 0$, the electric field produced by the forward rapidity going nucleus is dominated. As a result, the negative charge density at the positive x side becomes larger than that at the negative x side. On the other hand, as shown in Fig. 8.4 (b), in $\eta_s < 0$, the electric field produced by the backward rapidity going nucleus has a strong influence on the electric charge distribution. The negative charge density at the negative x side is larger than that at the positive x side. The clear electrical conductivity dependence is observed in all space rapidity regions. Since the electric current is proportional to electrical conductivity, the electric charge density with high electrical conductivity becomes larger. The produced electric charge density is approximately proportional to the electrical conductivity. It is consistent with Ohm's law.

Figure 9.9 shows the electric charge distribution on the freezeout hypersurface at $(y, \eta_s) = (0 \text{ fm}, 0)$ in Cu-Au collisions. Since the asymmetric configuration of the electric field in Cu-Au collisions, the electric charge distribution has an asymmetric structure at $\eta_s = 0$. As shown in Fig. 8.5 (b), in the transverse plane, the non-zero electric field along with the center of Cu nucleus in the freezeout hypersurface produces the negative electric charge in the negative x region. Thus, the negative charge density at the negative x region becomes larger than that at the positive x region. This is different from that in Au-Au collisions in Fig. 9.7. It implies that the charge-dependent directed flow becomes finite at $\eta_s = 0$.

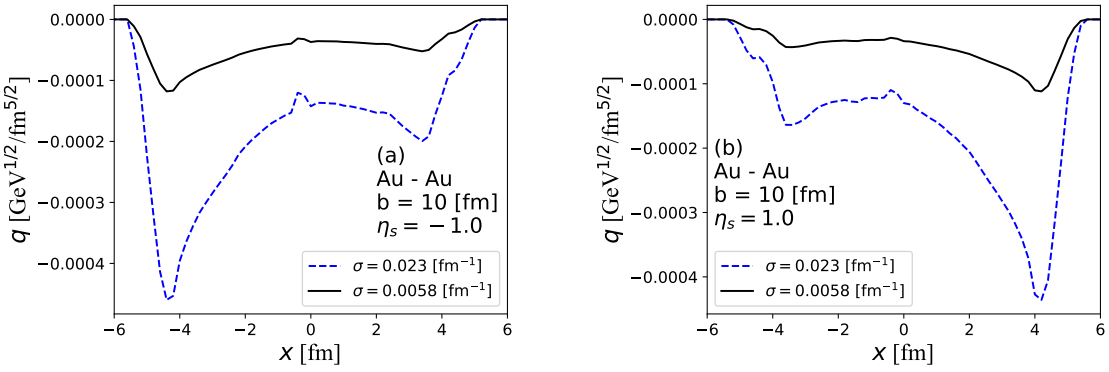

Figure 9.8: (color online) The charge distributions on the freezeout hypersurface as a function of x at $y = 0.0$ fm in the cases of (a) $\eta_s = -1.0$ and (b) $\eta_s = 1.0$ in Au-Au collisions. The black solid and blue dashed lines represent $\sigma = 0.0058$ and 0.023 fm^{-1} cases, respectively.

Figures 9.10 (a) and (b) represent the electric charge distribution on the freezeout hypersurface at $(y, \eta_s) = (0 \text{ fm}, -1)$ and $(0 \text{ fm}, +1)$ in Cu-Au collisions, respectively. In Cu-Au collisions, the electric charge density at $\eta_s = \pm 1$ has only one local minimum in the negative or positive x region. However, as shown in Fig. 9.10 (a), in $\eta_s < 0$, the slope of the electric charge distribution is steeper than that of Au-Au collisions. This reason is that as shown in Fig. 8.6 (b), in $\eta_s < 0$, the electric field in the positive x side rapidly decreases with increasing x. In addition, as shown in Fig. 9.10 (b), in $\eta_s > 0$, one can see the plateau structure in $x \in [-2, 1.5]$. The asymmetry of the configuration of the electric field in Fig. 8.6 (b) affects this plateau structure. The total absolute value of electric charge density at $\eta_s = 1.0$ in Fig. 9.10 (a) is larger than that at $\eta_s = -1.0$ in Fig. 9.10 (b). Since in Fig. 8.2 (b), the medium inside the freezeout hypersurface is close to the center of the Cu nucleus, the initial electric field produced by the Cu nucleus has strong influence on the electric density distributions in this region. The electrical conductivity dependence is the qualitatively same as in Au-Au collisions.

9.4.2 The velocity profile of the freezeout hypersurface

The electric charge density is carried by the fluid velocity on the freezeout hypersurface, which is the source of the charge-dependent anisotropic flow. We present the velocity profile on the freezeout hypersurface. Figures 9.11 (a) and (b) show the profile of the x-component of the space-averaged velocity on the freezeout hypersurface in Au-Au and Cu-Au collisions, respectively. Here, we define the x-component of the space-averaged velocity on the freezeout hypersurface as,

$$\langle v_x \rangle_{\Sigma_f} = \frac{\int_{\Sigma_f} dydx\gamma e(x, y, \eta_s) v_x(x, y, \eta_s)}{\int_{\Sigma_f} dydx\gamma e(x, y, \eta_s)}, \tag{9.8}$$

where Σ_f denotes the freezeout hypersurface. The initial tilted sources affect the profiles of the $\langle v_x \rangle_{\Sigma_f}$ in both of Au-Au and Cu-Au collisions. In both of Au-Au and

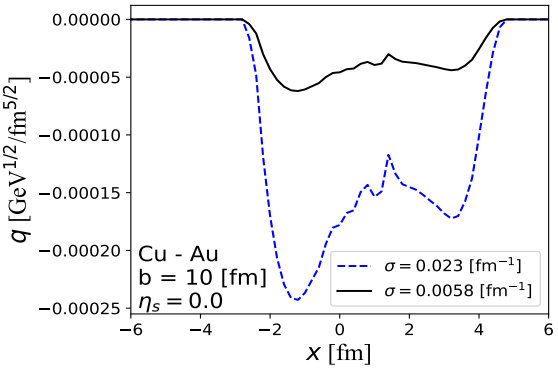

Figure 9.9: (color online) The charge distributions on the freezeout hypersurface as a function of x at $\eta_s = 0.0$ and $y = 0.0$ fm in Cu-Au collisions. The black solid and blue dashed lines represent the cases of $\sigma = 0.0058$ and 0.023 fm^{-1}, respectively.

Cu-Au collisions, the electrical conductivity dependence is not observed in the profile of the $\langle v_x \rangle_{\Sigma_f}$. In the lower electrical conductivity case, the profile of the $\langle v_x \rangle_{\Sigma_f}$ on the freezeout hypersurface is mainly determined by the pressure gradient of the QGP fluid. The contribution of electromagnetic fields is very small since the plasma beta, $\beta = p/p_{\rm em} \sim 10^3$, is large. Furthermore, in Au-Au collisions, the $\langle v_x \rangle_{\Sigma_f}$ has a negative value in $\eta_s > 0$ and a positive value in $\eta_s < 0$. On the other hand, in $\eta_s < 0$, the negative charges are mainly produced in $x < 0$ fm region which is the opposite direction of the $\langle v_x \rangle_{\Sigma_f}$. The magnitude of the directed flow of negatively charged hadrons has a smaller value than that of positively charged hadrons because of this anti-correlation between the electric charge distribution and the velocity profile.

In Au-Au collisions, the velocity profile has a symmetric structure about $\eta_s = 0$. In Cu-Au collisions, the velocity has a positive value at $\eta_s = 0$ and vanishes near $\eta_s \sim 0.5$. Since the initial asymmetric profile of the energy density provides the pressure gradients with respect to the direction of the Cu side, the velocity is finite even at $\eta_s = 0$.

9.4.3 The charge-dependent elliptic flow

Here, we consider the charge-odd contribution to the elliptic flow for π,

$$\Delta v_2(\eta) = v_2^{\pi^+}(\eta) - v_2^{\pi^-}(\eta), \tag{9.9}$$

focusing on the difference between the elliptic flow of π^+ and that of π^-. Figure 9.12 represents the charge-odd contribution to the elliptic flow for π as a function of η in Au-Au collisions. The black solid, blue dashed, red long-dashed dotted lines represent the cases of $\sigma = 0.0058, 0.023$, and 0.1 fm^{-1}. The electrical conductivity dependence is clearly observed. The Δv_2 in all electrical conductivity cases have negative values. It implies that the v_2 of π^- is enhanced by the electric current induced by Ohm's law. The behavior is also suggested by the electric charge distributions on the freezeout hypersurface in Fig. 9.7. The value of the Δv_2 at $\eta = 0$ is consistent with the previous study in Ref. [87]. However, the rapidity dependence of the Δv_2 has the different

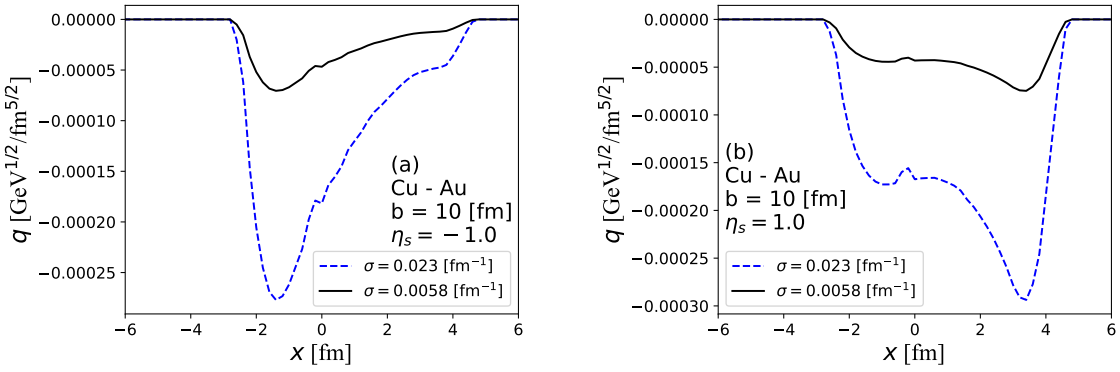

Figure 9.10: (color online) The charge distributions on the freezeout hypersurface as a function of x at $y = 0.0$ fm in the cases of (a) $\eta_s = -1.0$ and (b) $\eta_s = 1.0$ in Cu-Au collisions. The black solid and blue dashed lines represent $\sigma = 0.0058$ and 0.023 fm^{-1} cases, respectively.

behavior. Our results show that the $|\Delta v_2(\eta)|$ decreases with increasing $|\eta|$ but the result in Ref. [87] show that the $|\Delta v_2(\eta)|$ increases with $|\eta|$. This reason is that the magnetic field increases with $|\eta_s|$ in Ref. [87]. In our initial condition, electromagnetic fields decrease with increasing $|\eta_s|$ shown in Figs. 8.4 (a) and (b). Furthermore, as shown in Figs. 9.8 (a) and (b), the total absolute value of the electric charge density is relatively small at $\eta_s = \pm 1$ compared with that at $\eta_s = 0$ in Fig. 9.7. Hence, the value of the Δv_2 at the finite η_s becomes small.

Figure 9.13 stands for the Δv_2 for π as a function of η in Cu-Au collisions. The electrical conductivity dependence is clearly observed. As discussed in Figs. 9.9 and 9.10, the v_2 of the negatively charged hadrons is enhanced. On the other hand, the production of positively charged hadrons reduces due to the negative chemical potential of electric charge density. The Δv_2 of π becomes a negative value. In the forward rapidity region, the absolute value of the Δv_2 slightly increases in the cases of $\sigma = 0.023$ and 0.1 fm^{-1}. This reason is that, in $\eta_s > 0$, the distribution of electric charge density has a plateau structure because of the electric field produced by the Cu nucleus in Fig. 9.10 (b). This plateau makes the production of negatively charged hadrons in direction of an x-axis negative direction increase. Then, the elliptic momentum anisotropy of negatively charged hadrons becomes larger than that in $\eta_s < 0$ and at $\eta_s = 0$. In both collisions, the Δv_2 is approximately proportional to the electrical conductivity. The Δv_2 is sensitive to electrical conductivity.

9.4.4 The charge-dependent directed flow

Next we discuss the charge-odd contribution to the directed flow for π,

$$\Delta v_1(\eta) = v_1^{\pi^+}(\eta) - v_1^{\pi^-}(\eta). \tag{9.10}$$

Figure 9.14 shows the charge-odd contribution to the directed flow of π in Au-Au collisions. The black solid, blue dashed, and red long-dashed dotted lines represent the

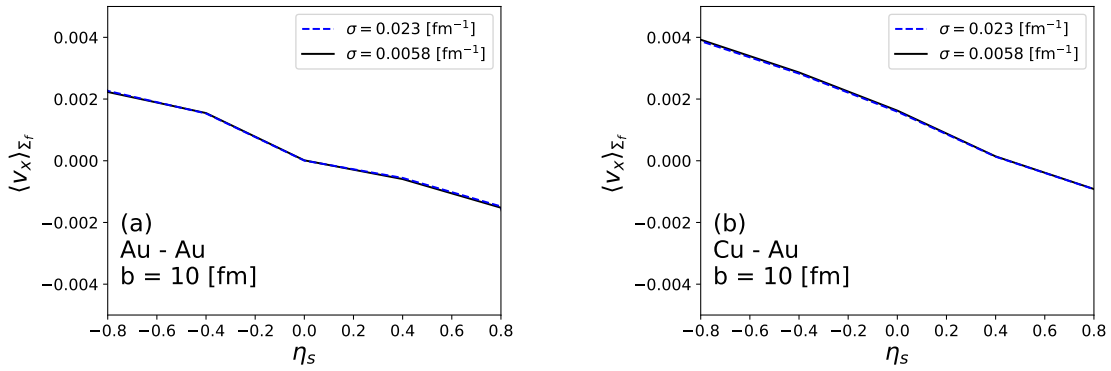

Figure 9.11: (color online) The weighted space-averaged x-component of velocity v_x profile on the freezeout hypersurface as a function of η_s in (a) Au-Au and (b) Cu-Au collisions. The black solid and blue dashed lines represent the cases of $\sigma = 0.0058$ and 0.023 fm^{-1}, respectively.

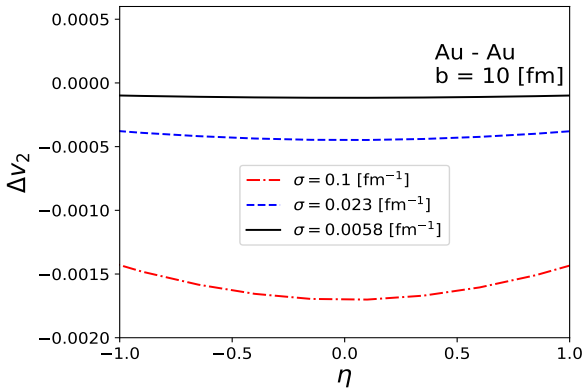

Figure 9.12: (color online) The charge-dependent elliptic flow Δv_2 as a function of η in Au-Au collisions. The black solid, blue dashed and red long dashed-dotted lines represent the cases of $\sigma = 0.0058$, 0.023, and 0.1 fm^{-1}, respectively.

cases of $\sigma = 0.0058, 0.023$, and 0.1 fm^{-1}. The tendency of the Δv_1 is similar to the charge-even contribution to the directed flow for π shown in Fig. 9.6 (a),

$$v_1(\eta) = v_1^{\pi^+}(\eta) + v_1^{\pi^-}(\eta). \tag{9.11}$$

This behavior is explained by the electric charge distribution on the freezeout hypersurface as discussed in Subsection 9.4.1. In Fig. 9.7, at $\eta_s = 0$, the electric charge density is symmetric about $x = 0$ fm. For this reason, Δv_1 vanishes at $\eta = 0$. In the forward rapidity region, as shown in Fig. 9.8 (b), the π^- is produced mainly in the positive x region, though the $\langle v_x \rangle_{\Sigma_f}$ has a negative value in the forward rapidity region. Hence, the contribution of the $|v_1|$ of the π^- is slightly smaller than that of the π^+. As a result, the Δv_1 becomes a negative value in the forward rapidity region. On the other hand, in the backward rapidity region, the π^- is emitted mainly in the negative x region. The $\langle v_x \rangle_{\Sigma_f}$ has a positive value in the backward rapidity region. Then, the v_1

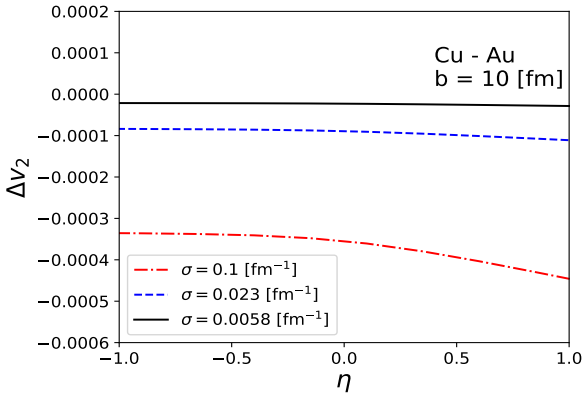

Figure 9.13: (color online) The charge-dependent elliptic flow Δv_2 as a function of η in Cu-Au collisions. The black solid, blue dashed and red long dashed-dotted lines represent the cases of $\sigma = 0.0058$, 0.023, and 0.1 fm^{-1}, respectively.

of the π^- has a slightly smaller value than that of the π^+. The Δv_1 becomes positive in the backward rapidity region.

The electrical conductivity dependence is clearly observed in the forward and backward rapidity regions. The Δv_1 is approximately proportional to electrical conductivity. This dependence is consistent with the previous study in Ref. [87]. Furthermore, we compare our results with the STAR data [199]. The result in the case of $\sigma = 0.023$ fm^{-1}, which corresponds to $\sigma = (5.8 \pm 2.9)/\hbar c$ fm^{-1} of the three-flavor QGP at $T = 250$ MeV in the lattice QCD calculations [152–154,156], is slightly larger than that of STAR data. In the low conductive medium with $\sigma = 0.0058$ fm^{-1}, our result is consistent with the STAR data within the error bar. It implies the possibility of the incomplete electromagnetic response of the QGP medium [103,104], though there is still ambiguity to the conclusive value of electrical conductivity in lattice QCD calculation. In our models, the relaxation process of the electric current is ignored. If the relaxation process of the electric current is considered, the effective electrical conductivity becomes small, because of the reduction of the electric current by the incomplete electromagnetic response associated with the relaxation process. To discuss quantitatively the effect of the incomplete electromagnetic response, we need to extend Ohm's law, including the relaxation time of the electric current. In more precise measurements of Δv_1, it can be detected in high-energy heavy-ion collisions.

Figure 9.15 represents the charge-odd contribution to the directed flow of π in Cu-Au collisions. The electrical conductivity dependence is clearly observed. The Δv_1 of π is approximately proportional to electrical conductivity at $\eta = 0$ in Cu-Au collisions. It is consistent with the straightforward estimate of the Δv_1 in Cu-Au collisions [99]. The electric charge density at $\eta_s = 0$ shown in Fig. 9.9 affects this electrical conductivity dependence. The Δv_1 has the non-zero value at $\eta = 0$ in finite electrical conductivity case. There are two reasons. The first one is that the $\langle v_x \rangle_{\Sigma_f}$ has the finite value at $\eta_s = 0$ in Fig. 9.11 (b) because of the stronger pressure gradient along with the impact parameter in the initial energy density profile of the QGP medium. The second one is that the asymmetric configuration of the electric charge distribution in Fig. 9.9 due to

the initial electric fields at $\eta_s = 0$ affects the Δv_1 at $\eta = 0$. In all electrical conductivity cases, Δv_1 is crossing zero point near $\eta = 0.5$. This reason is that the $\langle v_x \rangle_{\Sigma_f}$ is vanishing near $\eta_s = 0.5$ in Fig. 9.11 (b). Hence, there is no electrical conductivity dependence since the velocity profile has no difference in each electrical conductivity. Furthermore, in Cu-Au collisions, the Δv_1 may be easily detected since it has the non-zero value at $\eta = 0$ in finite electrical conductivity. Our result indicates that the precise measurement of the Δv_1 is suitable for the determination of the value of the electrical conductivity of the QGP. This measurement sheds light on the electromagnetic response of the QGP medium.

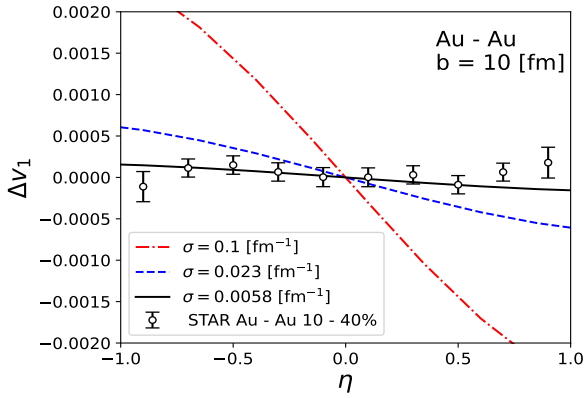

Figure 9.14: (color online) The charge-dependent directed flow Δv_1 as a function of η in Au-Au collisions. The black solid, blue dashed and red long dashed-dotted lines represent the cases of $\sigma = 0.0058$, 0.023, and 0.1 fm^{-1}, respectively.

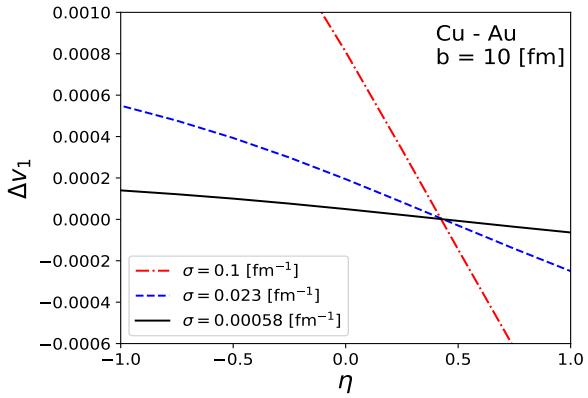

Figure 9.15: (color online) The charge-dependent directed flow Δv_1 as a function of η in Cu-Au collisions. The black solid, blue dashed and red long dashed-dotted lines represent the cases of $\sigma = 0.0058$, 0.023, and 0.1 fm^{-1}, respectively.

Chapter 10

Summary

In this thesis, we investigated the QGP bulk properties focused on the electromagnetic response of the QGP medium produced in high-energy heavy-ion collisions. In high-energy heavy-ion collisions, ultraintense electromagnetic fields are produced by two colliding nuclei. The magnitude of the magnetic field is reached the highest in our universe, e.g., $|eB| \sim 10^{15}$ T for $\sqrt{s_{\rm NN}} = 200$ GeV Au-Au collisions [75–79]. In order to study the electromagnetic response of the QGP, we need to construct the relativistic resistive magneto-hydrodynamic model for high-energy heavy-ion collisions.

In Chap. 1, we presented a brief introduction to quantum chromodynamics, the quark-gluon plasma, and high-energy heavy-ion collisions. After a brief introduction, we introduced basic variables and kinematics in high-energy heavy-ion collisions in Chap. 2. One of the current main purposes is to extract the transport coefficients of the QGP. The important observables related to the collective dynamics in high-energy heavy-ion collisions were also presented. The anisotropic flow coefficients are strongly correlated with the collective dynamics of the QGP phase. Then, by model-to-data comparison. the specific shear viscosity and bulk viscosity can be extracted from the experimental data. In particular, the charge-dependent anisotropic flow was interesting observables as a probe of the electromagnetic response of the QGP medium. In Chap. 3, we overviewed the properties of electromagnetic fields produced in high-energy heavy-ion collisions under simple assumptions. We saw the importance of the medium response such as the electrical conductivity of the QGP for the spacetime evolution of electromagnetic fields. In the pre-equilibrium stage, since the medium has not been formed, electromagnetic fields decay instantaneously into the vacuum, $B(t) \propto 1/t^3$. On the other hand, in the equilibrium stage, since the medium has been formed, the magnetic field is frozen in the plasma element if QGP has large electrical conductivity. In this case, the magnetic fields decay as $B(t) \propto 1/t$ in the expanding system into the transverse plane.

In Chap. 4, we reviewed basics of relativistic hydrodynamics. The equations of the relativistic hydrodynamics consist of the conservation law of the energy-momentum and conserved charges. The equation of the state which includes the properties of the matter is needed to close the system of differential equations. In ideal hydrodynamics which is no dissipation and no viscosity, the entropy current is conserved. In Chap. 5, we introduced the relativistic resistive magneto-hydrodynamic framework. In relativistic resistive magneto-hydrodynamics, entropy production occurs due to Ohm's law. If

we take the infinite electrical conductivity, the longitudinal boost invariant solutions, which are called magnetized Bjorken flow [175], exist. In this solution, the magnetic field decay as $B(t) \propto 1/t$ with longitudinal fluid's expansion. Furthermore, we reviewed the longitudinal expansion in the resistive case [101]. In the resistive case, the acceleration is induced by the resistive effect. Because of this acceleration, the decay of the magnetic field becomes faster than that in the ideal case.

To execute the analysis of high-energy heavy-ion collisions based on RRMHD framework, we develop the new numerical simulation code for RRMHD in the Milne coordinates in Chap. 6 [100]. In our newly developed RRMHD simulation code, the governing equations were split into the stiff parts and the non-stiff parts. For the non-stiff parts, the time integration was executed by the TVD Runge-Kutta algorithm [183]. The numerical flux was calculated by the HLL approximated Riemann solver. The primitive variables were interpolated from the cell center to the cell surface by using the second-order accurate scheme [180]. For the stiff parts, we integrated these equations using semi-analytic solutions to avoid unexpected small time steps. Though Maxwell equations ensure that the divergence-free constraints are satisfied at all times, in numerical simulation, the integration of Maxwell equations in a not well-designed scheme has violated these conditions because of the numerical error. In order to avoid this problem, we employed the generalized Lagrange multiplier method to guarantee these conditions [177–179].

In Chap. 7, we have verified the correctness of our algorithm from the comparison between numerical results and analytical solutions or results of the other RMHD simulations such as Brio-Wu type shock tubes, propagation of the large amplitude circularly polarized Alfv́en waves, self-similar current sheet, cylindrical explosion, resistive rotor, and Bjorken flow [100]. In these test problems, our numerical solutions were consistent with analytic solutions or results of the other RRMHD simulations. Furthermore, we investigated the accelerating longitudinal expansion of relativistic resistive magneto-hydrodynamics in high-energy heavy-ion collisions in comparison with semi-analytic solutions [101]. Our numerical code reproduced these solutions [100]. We conclude that our numerical simulations capture the characteristic features of dynamics in high-energy heavy-ion collisions and is applicable to the analysis of high-energy heavy-ion collisions.

In Chap. 8, we construct the initial condition of RRMHD equations for high-energy heavy-ion collisions both of Au-Au and Cu-Au collisions [100]. We employ the optical Glauber model [133] as the initial condition for the QGP medium. In order to include the source of the directed flow, we adopt the tilted source to the optical Glauber model [191]. We computed initial electromagnetic fields based on Ref. [81]. We considered the electromagnetic fields produced by the electric charge e moving along parallel to the beam axis ($\hat{\mathbf{z}}$) with velocity v in the laboratory frame by an observer located at $\mathbf{r} = z\hat{\mathbf{z}} + \mathbf{x}_\perp$ in the Minkowski coordinates.

In Chap. 9, we applied our newly developed relativistic resistive magneto-hydrodynamic model to high-energy-heavy-ion collisions [102]. First, we investigated the effect of electromagnetic fields on fluid flow. In symmetric collisions, there are only small contributions. On the other hand, in asymmetric collisions, the electromagnetic fields have significant contributions due to the existence of the finite electric field in freeze-out hypersurface. We found this contribution from the dissipation associated with

Ohm's law, calculating the dissipation measure. In both collisions, the volume of the freezeout hypersurface is not changed by electromagnetic fields. Next, we calculated the anisotropic flow using the hadron distribution produced by Cooper-Frye formula. In both collisions, the elliptic flow of π does not have the electrical conductivity dependence. The large plasma beta is reflected in the electrical conductivity dependence of the elliptic flow. It indicates that Maxwell's stress force does not affect the elliptic flow. In symmetric collisions, the directed flow is not changed in the different values of the electrical conductivity of the QGP medium. This reason is that the dissipation associated with Ohm's law has only the symmetric shape for the positive x region and the negative x region. In asymmetric collisions, since the dissipation measure has the asymmetric shape for the positive x region and the negative x region, the directed flow decrease with increasing electrical conductivity at $\eta_s = 0$. This result indicates that the energy transfer from electromagnetic fields to the fluid by the dissipation prevents the flow in direction of the Cu nucleus.

We found that the electric charge distribution is sensitive to the RRMHD evolution and the initial condition both of the QGP medium and electromagnetic fields. The electrical conductivity dependence of the electric charge distribution is clear. The electric charge distribution is approximately proportional to electrical conductivity. We have calculated the charge-odd contribution to the anisotropic flows in Au-Au and Cu-Au collisions. The charge-odd contribution to the elliptic flow and directed flow is sensitive to the electrical conductivity and the initial profile of electromagnetic fields. We confirmed that the elliptic flow of the π^- is enhanced by the conduction current associated with Ohm's law. As a result, the charge-odd contribution to the elliptic flow has a negative value in both of Au-Au and Cu-Au collisions. Besides, it is approximately proportional to electrical conductivity. In the charge-odd contribution to the directed flow, the electrical conductivity dependence is also clearly observed in both collisions. We compared our results and the STAR data [84] in Au-Au collisions. The result in the case of $\sigma = 0.023$ fm^{-1} was slightly larger than that of the STAR data. This value of the electrical conductivity corresponds to $\sigma = (5.8 \pm 2.9)/\hbar c$ fm^{-1} of the three-flavor QGP at $T = 250$ MeV in the Lattice QCD calculations [152–154, 156]. On the other hand, in the highly resistive case of $\sigma = 0.0058$ fm^{-1}, our result is in good agreement with the STAR data within the error bar. It implies that the incomplete electromagnetic response of the QGP medium [103, 104] appeared in STAR data [84]. In more precision measurements, it can be detected in high-energy heavy-ion collisions. In Cu-Au collisions, we observe that the charge-odd contribution to the directed flow is approximated proportional to electrical conductivity at $\eta = 0$. It is consistent with the straightforward estimate of the charge-odd contribution of directed flow in Cu-Au collisions [99]. Then, we conclude that the charge-dependent anisotropic flow is a good probe to extract the electrical conductivity of QGP medium.

For our future works, we needed to consider further development and analyses to extract the electromagnetic response of the QGP medium produced in high-energy heavy-ion collisions. Especially, one can be required to extend to our RRMHD model following point of view,

- One of the characteristic properties of high-energy heavy-ion collisions is the event-by-event fluctuations. This event-by-event fluctuation is caused by not only the quantum fluctuations in the interaction of quarks and gluons in the

early stage but also the thermodynamic fluctuations in the QGP phase. The former fluctuation is reflected in the initial condition of the hydrodynamic equations. In the present model, we used the event-averaged initial condition. In other words, the event-by-event fluctuation is neglected. As initial conditions included event-by-event fluctuations, there are MC-Glauber [133,134] and MC-KLN models [200,201]. In addition, the recent development of the initial condition of electromagnetic fields included event-by-event fluctuation also exists [80]. The latter fluctuation is related to hydrodynamic fluctuations. This depends on the dissipation by the transport coefficients. Then, we need to consider the relativistic viscous hydrodynamic framework. Nowadays, the relativistic hydrodynamic models with hydrodynamic fluctuation [202,203] are becoming the standard methods for the analysis of high-energy heavy-ion collisions. It is an interesting subject for further development of RMHD simulation.

- Another direction of the further development of the RMHD model for high-energy heavy-ion collisions is to include the relaxation process of the electric current [103, 104]. In the early stage dynamics, this relaxation process has the significant effect on the production of the electric current [104]. The dilepton production is also sensitive to the relaxation process of the electric current [103]. Recently, numerical RRMHD simulations with relaxation time of the electric current are developed [204–206]. To discuss the detailed dynamics of electromagnetic fields coupled with the QGP medium, we need to extend the simplest form of Ohm's law to the second-order Ohm's law.

- The RRMHD model is applicable for lower energy collisions. In lower energy collisions, the Λ hyperon's polarization is observed [207]. The coupling between the longitudinal vorticity and electromagnetic fields may allow the observation of non-trivial phenomena such as magneto-rotational instability. It indicates that longitudinal vorticity exists at the early stage of heavy-ion collisions. In lower energy collisions, the baryon number density does not vanish [208]. Then, we need to extend the EoS to that with the finite baryon density [209–211]. One of the purposes of the beam energy scan experiments is to explore the QCD critical point. The application of the RRMHD model for lower energy collisions can address this area and discuss the effect of background electromagnetic fields on the phase diagram of the QCD [212].

- Recently, the charge-dependent directed flow of the heavy mesons and dileptons has been proposed as a signature of the electromagnetic fields [195, 196]. It is possible to determine the initial electromagnetic fields. Furthermore, photons are one of the important observables to extract electromagnetic fields. In particular, the thermal photons give detailed information of electromagnetic fields in the QGP phase, since photons are not changed by strong interactions. The estimate of directed and elliptic flows of photons in electromagnetic fields is an important subject.

- The ultraintense electromagnetic fields may allow the observation of novel quantum phenomena such as the chiral magnetic effect (CME) [75,91] and the chiral

magnetic wave (CMW) [92]. The CME and CMW signals have been experimentally explored in iso-bar collisions, Zr-Zr, and Ru-Ru collisions at RHIC [97, 98]. However, there is no striking experimental evidence of these phenomena in the iso-bar experiments. According to the anomalous hydrodynamic calculation, the chiral magnetic effect can be found in the azimuthal anisotropy of charged hadrons [213]. For analytical studies, the initial condition of electromagnetic fields with CME in high-energy heavy-ion collisions has been investigated [160, 214], but the evolution of these fields has not been well understood. The comprehensive studies using RRMHD would shed light on these problems.

Acknowledgments

I have to acknowledge the comments on my work and my thesis by my supervisor, Prof. Chiho Nonaka from Hiroshima University. Prof. Nonaka spent much of her time reading my thesis and giving many useful comments. She introduce the physics of high-energy heavy-ion collisions and the method of analysis of it based on the relativistic hydrodynamic models to me. I would like to express my greatest appreciation to her. I also have to acknowledge the powerful support of my collaborator, Prof. Takahiro Miyoshi from Hiroshima University, and Prof. Hiroyuki Takahashi from Komazawa University. They introduced the numerical techniques of relativistic resistive magneto-hydrodynamics and its astrophysical application to me. I also thank to Prof. Masayasu Harada. Prof. Harada gave useful advice for my study and presentations in H-lab. activities. Without their advice, I would not complete this thesis.

The work of K.N. was supported in part by JSPS Grant-in-Aid for JSPS Research Fellow No. JP21J13651.

References

[1] C. N. Yang and R. L. Mills. Conservation of isotopic spin and isotopic gauge invariance. *Phys. Rev.*, 96:191–195, Oct 1954.

[2] Yoichiro Nambu. Systematics of hadrons in subnuclear physics. *Preludes in theoretical physics*, 1965.

[3] Moo-Young Han and Yoichiro Nambu. Three-triplet model with double su (3) symmetry. *Physical Review*, 139(4B):B1006, 1965.

[4] H. David Politzer. Reliable perturbative results for strong interactions? *Phys. Rev. Lett.*, 30:1346–1349, Jun 1973.

[5] David J. Gross and Frank Wilczek. Ultraviolet behavior of non-abelian gauge theories. *Phys. Rev. Lett.*, 30:1343–1346, Jun 1973.

[6] G. Baym and S.A. Chin. Can a neutron star be a giant mit bag? *Physics Letters B*, 62(2):241–244, 1976.

[7] Joseph I. Kapusta. Quantum chromodynamics at high temperature. *Nuclear Physics B*, 148(3):461–498, 1979.

[8] Edward V. Shuryak. Theory of Hadronic Plasma. *Sov. Phys. JETP*, 47:212–219, 1978.

[9] Frank R. Brown, Frank P. Butler, Hong Chen, Norman H. Christ, Zhihua Dong, Wendy Schaffer, Leo I. Unger, and Alessandro Vaccarino. On the existence of a phase transition for qcd with three light quarks. *Phys. Rev. Lett.*, 65:2491–2494, Nov 1990.

[10] Yasumichi Aoki, Zoltan Fodor, Sandor D. Katz, and Kalman K. Szabó. The equation of state in lattice qcd: with physical quark masses towards the continuum limit. *Journal of High Energy Physics*, 2006(01):089, jan 2006.

[11] Y. Aoki, G. Endrodi, Z. Fodor, S. D. Katz, and K. K. Szabo. The Order of the quantum chromodynamics transition predicted by the standard model of particle physics. *Nature*, 443:675–678, 2006.

[12] A. Bazavov et al. Equation of state and QCD transition at finite temperature. *Phys. Rev. D*, 80:014504, 2009.

[13] C. DeTar and U. M. Heller. QCD Thermodynamics from the Lattice. *Eur. Phys. J. A*, 41:405–437, 2009.

[14] M. Asakawa and K. Yazaki. Chiral Restoration at Finite Density and Temperature. *Nucl. Phys. A*, 504:668–684, 1989.

[15] A. Barducci, R. Casalbuoni, S. De Curtis, Raoul Gatto, and Giulio Pettini. Chiral Symmetry Breaking in QCD at Finite Temperature and Density. *Phys. Lett. B*, 231:463–470, 1989.

[16] A. Barducci, R. Casalbuoni, S. De Curtis, Raoul Gatto, and Giulio Pettini. Chiral Phase Transitions in QCD for Finite Temperature and Density. *Phys. Rev. D*, 41:1610, 1990.

[17] Frank Wilczek. Application of the renormalization group to a second order QCD phase transition. *Int. J. Mod. Phys. A*, 7:3911–3925, 1992. [Erratum: Int.J.Mod.Phys.A 7, 6951 (1992)].

[18] Juergen Berges and Krishna Rajagopal. Color superconductivity and chiral symmetry restoration at nonzero baryon density and temperature. *Nucl. Phys. B*, 538:215–232, 1999.

[19] Akihiko Monnai, Björn Schenke, and Chun Shen. Equation of state at finite densities for QCD matter in nuclear collisions. *Phys. Rev. C*, 100(2):024907, 2019.

[20] L. Adamczyk et al. Harmonic decomposition of three-particle azimuthal correlations at energies available at the BNL Relativistic Heavy Ion Collider. *Phys. Rev. C*, 98(3):034918, 2018.

[21] Philippe de Forcrand. Simulating QCD at finite density. *PoS*, LAT2009:010, 2009.

[22] Kenji Fukushima and Tetsuo Hatsuda. The phase diagram of dense QCD. *Rept. Prog. Phys.*, 74:014001, 2011.

[23] Bertrand C. Barrois. Superconducting Quark Matter. *Nucl. Phys. B*, 129:390–396, 1977.

[24] D. Bailin and A. Love. Superfluidity and Superconductivity in Relativistic Fermion Systems. *Phys. Rept.*, 107:325, 1984.

[25] Krishna Rajagopal and Frank Wilczek. *The Condensed matter physics of QCD*, pages 2061–2151. 11 2000.

[26] Mark G. Alford, Andreas Schmitt, Krishna Rajagopal, and Thomas Schäfer. Color superconductivity in dense quark matter. *Rev. Mod. Phys.*, 80:1455–1515, 2008.

[27] B.B. Back et al. The phobos perspective on discoveries at rhic. *Nuclear Physics A*, 757(1):28–101, 2005. First Three Years of Operation of RHIC.

[28] K. Adcox et al. Formation of dense partonic matter in relativistic nucleus–nucleus collisions at rhic: Experimental evaluation by the phenix collaboration. *Nuclear Physics A*, 757(1):184–283, 2005. First Three Years of Operation of RHIC.

[29] J. Adams et al. Experimental and theoretical challenges in the search for the quark–gluon plasma: The star collaboration's critical assessment of the evidence from rhic collisions. *Nuclear Physics A*, 757(1):102–183, 2005. First Three Years of Operation of RHIC.

[30] I. Arsene et al. Quark–gluon plasma and color glass condensate at rhic? the perspective from the brahms experiment. *Nuclear Physics A*, 757(1):1–27, 2005. First Three Years of Operation of RHIC.

[31] C. Adler et al. Identified particle elliptic flow in Au + Au collisions at s(NN)**(1/2) = 130-GeV. *Phys. Rev. Lett.*, 87:182301, 2001.

[32] C. Adler et al. Elliptic flow from two and four particle correlations in Au+Au collisions at s(NN)**(1/2) = 130-GeV. *Phys. Rev. C*, 66:034904, 2002.

[33] K. Adcox et al. Flow measurements via two particle azimuthal correlations in Au+Au collisions at s(NN)**(1/2) = 130-GeV. *Phys. Rev. Lett.*, 89:212301, 2002.

[34] S. S. Adler et al. Elliptic flow of identified hadrons in Au+Au collisions at s(NN)**(1/2) = 200-GeV. *Phys. Rev. Lett.*, 91:182301, 2003.

[35] B. B. Back et al. Pseudorapidity and centrality dependence of the collective flow of charged particles in Au+Au collisions at s(NN)**(1/2) = 130-GeV. *Phys. Rev. Lett.*, 89:222301, 2002.

[36] B. B. Back et al. Energy dependence of elliptic flow over a large pseudorapidity range in Au+Au collisions at RHIC. *Phys. Rev. Lett.*, 94:122303, 2005.

[37] B. B. Back et al. Centrality and pseudorapidity dependence of elliptic flow for charged hadrons in Au+Au collisions at s(NN)**(1/2) = 200-GeV. *Phys. Rev. C*, 72:051901, 2005.

[38] Larry D. McLerran and T. Toimela. Photon and Dilepton Emission from the Quark - Gluon Plasma: Some General Considerations. *Phys. Rev. D*, 31:545, 1985.

[39] Joseph I. Kapusta, P. Lichard, and D. Seibert. High-energy photons from quark - gluon plasma versus hot hadronic gas. *Phys. Rev. D*, 44:2774–2788, 1991. [Erratum: Phys.Rev.D 47, 4171 (1993)].

[40] Charles Gale and Kevin L. Haglin. Electromagnetic radiation from relativistic nuclear collisions. pages 364–429, 6 2003.

[41] Simon Turbide, Charles Gale, Evan Frodermann, and Ulrich Heinz. Electromagnetic radiation from nuclear collisions at RHIC energies. *Phys. Rev. C*, 77:024909, 2008.

[42] S. S. Adler et al. Centrality dependence of direct photon production in s(NN)**(1/ 2) = 200-GeV Au + Au collisions. *Phys. Rev. Lett.*, 94:232301, 2005.

[43] A. Adare et al. Enhanced production of direct photons in Au+Au collisions at $\sqrt{s_{NN}} = 200$ GeV and implications for the initial temperature. *Phys. Rev. Lett.*, 104:132301, 2010.

[44] S. Afanasiev et al. Enhancement of the dielectron continuum in s(NN)**(1/2) = 200-geV Au+Au collisions. 6 2007.

[45] Jie Zhao. Dielectron continuum production from $\sqrt{s_{NN}} = 200$ GeV p + p and Au + Au collisions at STAR. *J. Phys. G*, 38:124134, 2011.

[46] T. Matsui and H. Satz. J/ψ Suppression by Quark-Gluon Plasma Formation. *Phys. Lett. B*, 178:416–422, 1986.

[47] S. S. Adler et al. J / psi production in Au Au collisions at s(NN)**(1/2) = 200-GeV at the Relativistic Heavy Ion Collider. *Phys. Rev. C*, 69:014901, 2004.

[48] A. Adare et al. J/ψ Production vs Centrality, Transverse Momentum, and Rapidity in Au+Au Collisions at $\sqrt{s_{NN}} = 200$ GeV. *Phys. Rev. Lett.*, 98:232301, 2007.

[49] A. Adare et al. J/psi Production in s(NN)**(1/2) = 200-GeV Cu+Cu Collisions. *Phys. Rev. Lett.*, 101:122301, 2008.

[50] B. I. Abelev et al. J/psi production at high transverse momentum in p+p and Cu+Cu collisions at s(NN)**1/2 = 200GeV. *Phys. Rev. C*, 80:041902, 2009.

[51] Johann Rafelski and Berndt Muller. Strangeness Production in the Quark - Gluon Plasma. *Phys. Rev. Lett.*, 48:1066, 1982. [Erratum: Phys.Rev.Lett. 56, 2334 (1986)].

[52] Josef Sollfrank and Ulrich W. Heinz. The Role of strangeness in ultrarelativistic nuclear collisions. pages 555–634, 5 1995.

[53] A. Andronic, P. Braun-Munzinger, and J. Stachel. Hadron production in central nucleus-nucleus collisions at chemical freeze-out. *Nucl. Phys. A*, 772:167–199, 2006.

[54] F. Antinori et al. Enhancement of hyperon production at central rapidity in 158-A-GeV/c Pb-Pb collisions. *J. Phys. G*, 32:427–442, 2006.

[55] C. Alt et al. Pion and kaon production in central Pb + Pb collisions at 20-A and 30-A-GeV: Evidence for the onset of deconfinement. *Phys. Rev. C*, 77:024903, 2008.

[56] P. K. Kovtun, D. T. Son, and A. O. Starinets. Viscosity in strongly interacting quantum field theories from black hole physics. *Phys. Rev. Lett.*, 94:111601, Mar 2005.

[57] Laszlo P. Csernai, Joseph I. Kapusta, and Larry D. McLerran. Strongly interacting low-viscosity matter created in relativistic nuclear collisions. *Phys. Rev. Lett.*, 97:152303, Oct 2006.

[58] Harvey B. Meyer. Calculation of the shear viscosity in su(3) gluodynamics. *Phys. Rev. D*, 76:101701, Nov 2007.

[59] Harvey B. Meyer. Transport properties of the quark-gluon plasma from lattice qcd. *Nuclear Physics A*, 830(1):641c–648c, 2009. Quark Matter 2009.

[60] N. Astrakhantsev, Viktor Braguta, and Andrey Kotov. Temperature dependence of shear viscosity of $SU(3)$–gluodynamics within lattice simulation. *JHEP*, 04:101, 2017.

[61] Sz. Borsányi, Z. Fodor, M. Giordano, S. D. Katz, A. Pásztor, C. Ratti, A. Schäfer, K. K. Szabó, and B. C. Tóth. High statistics lattice study of stress tensor correlators in pure $su(3)$ gauge theory. *Phys. Rev. D*, 98:014512, Jul 2018.

[62] Madappa Prakash, Manju Prakash, Raju Venugopalan, and Gerd Welke. Nonequilibrium properties of hadronic mixtures. *Physics Reports*, 227(6):321–366, 1993.

[63] Peter Arnold, Guy D Moore, and Laurence G Yaffe. Transport coefficients in high temperature gauge theories, 2. beyond leading log. *Journal of High Energy Physics*, 2003(05):051–051, may 2003.

[64] Ulrich Heinz and Raimond Snellings. Collective flow and viscosity in relativistic heavy-ion collisions. *Annual Review of Nuclear and Particle Science*, 63(1):123–151, 2013.

[65] CHARLES GALE, SANGYONG JEON, and BJÖRN SCHENKE. Hydrodynamic modeling of heavy-ion collisions. *International Journal of Modern Physics A*, 28(11):1340011, 2013.

[66] R. Derradi de Souza, T. Koide, and T. Kodama. Hydrodynamic approaches in relativistic heavy ion reactions. *Progress in Particle and Nuclear Physics*, 86:35–85, 2016.

[67] Kazuhisa Okamoto and Chiho Nonaka. Temperature dependence of transport coefficients of qcd in high-energy heavy-ion collisions. *Phys. Rev. C*, 98:054906, Nov 2018.

[68] Jonah E. Bernhard, J. Scott Moreland, and Steffen A. Bass. Bayesian estimation of the specific shear and bulk viscosity of quark–gluon plasma. *Nature Phys.*, 15(11):1113–1117, 2019.

[69] D. Everett and otehrs. Multisystem bayesian constraints on the transport coefficients of qcd matter. *Phys. Rev. C*, 103:054904, May 2021.

[70] Govert Nijs, Wilke van der Schee, Umut Gürsoy, and Raimond Snellings. Bayesian analysis of heavy ion collisions with the heavy ion computational framework Trajectum. *Phys. Rev. C*, 103(5):054909, 2021.

[71] Govert Nijs, Wilke van der Schee, Umut Gürsoy, and Raimond Snellings. Transverse Momentum Differential Global Analysis of Heavy-Ion Collisions. *Phys. Rev. Lett.*, 126(20):202301, 2021.

[72] D. Everett et al. Phenomenological constraints on the transport properties of QCD matter with data-driven model averaging. *Phys. Rev. Lett.*, 126(24):242301, 2021.

[73] Jussi Auvinen, Kari J. Eskola, Pasi Huovinen, Harri Niemi, Risto Paatelainen, and Peter Petreczky. Temperature dependence of η/s of strongly interacting matter: Effects of the equation of state and the parametric form of $(\eta/s)(T)$. *Phys. Rev. C*, 102(4):044911, 2020.

[74] J. E. Parkkila, A. Onnerstad, and D. J. Kim. Bayesian estimation of the specific shear and bulk viscosity of the quark-gluon plasma with additional flow harmonic observables. *Phys. Rev. C*, 104(5):054904, 2021.

[75] Dmitri E. Kharzeev, Larry D. McLerran, and Harmen J. Warringa. The effects of topological charge change in heavy ion collisions: "event by event p and cp violation". *Nuclear Physics A*, 803(3):227–253, 2008.

[76] V. V. SKOKOV, A. YU. ILLARIONOV, and V. D. TONEEV. Estimate of the magnetic field strength in heavy-ion collisions. *International Journal of Modern Physics A*, 24(31):5925–5932, 2009.

[77] V. Voronyuk, V. D. Toneev, W. Cassing, E. L. Bratkovskaya, V. P. Konchakovski, and S. A. Voloshin. Electromagnetic field evolution in relativistic heavy-ion collisions. *Phys. Rev. C*, 83:054911, May 2011.

[78] L. McLerran and V. Skokov. Comments about the electromagnetic field in heavy-ion collisions. *Nuclear Physics A*, 929:184–190, 2014.

[79] Xu-Guang Huang. Electromagnetic fields and anomalous transports in heavy-ion collisions—a pedagogical review. *Reports on Progress in Physics*, 79(7):076302, jun 2016.

[80] Wei-Tian Deng and Xu-Guang Huang. Event-by-event generation of electromagnetic fields in heavy-ion collisions. *Phys. Rev. C*, 85:044907, Apr 2012.

[81] Kirill Tuchin. Time and space dependence of the electromagnetic field in relativistic heavy-ion collisions. *Phys. Rev. C*, 88:024911, Aug 2013.

[82] Adam Bzdak and Vladimir Skokov. Event-by-event fluctuations of magnetic and electric fields in heavy ion collisions. *Physics Letters B*, 710(1):171–174, 2012.

[83] B. I. Abelev et al. System-size independence of directed flow at the Relativistic Heavy-Ion Collider. *Phys. Rev. Lett.*, 101:252301, 2008.

[84] Leszek Adamczyk et al. Azimuthal anisotropy in Cu+Au collisions at $\sqrt{s_{NN}}$ = 200 GeV. *Phys. Rev. C*, 98(1):014915, 2018.

[85] S. Acharya et al. Probing the effects of strong electromagnetic fields with charge-dependent directed flow in pb-pb collisions at the lhc. *Phys. Rev. Lett.*, 125:022301, Jul 2020.

[86] Umut Gursoy, Dmitri Kharzeev, and Krishna Rajagopal. Magnetohydrodynamics, charged currents and directed flow in heavy ion collisions. *Phys. Rev. C*, 89(5):054905, 2014.

[87] Umut Gürsoy, Dmitri Kharzeev, Eric Marcus, Krishna Rajagopal, and Chun Shen. Charge-dependent Flow Induced by Magnetic and Electric Fields in Heavy Ion Collisions. *Phys. Rev. C*, 98(5):055201, 2018.

[88] Victor Roy, Shi Pu, Luciano Rezzolla, and Dirk H. Rischke. Effect of intense magnetic fields on reduced-MHD evolution in $\sqrt{s_{\rm NN}} = 200$ GeV Au+Au collisions. *Phys. Rev. C*, 96(5):054909, 2017.

[89] Gabriele Inghirami, Luca Del Zanna, Andrea Beraudo, Mohsen Haddadi Moghaddam, Francesco Becattini, and Marcus Bleicher. Numerical magneto-hydrodynamics for relativistic nuclear collisions. *Eur. Phys. J. C*, 76(12):659, 2016.

[90] Gabriele Inghirami, Mark Mace, Yuji Hirono, Luca Del Zanna, Dmitri E. Kharzeev, and Marcus Bleicher. Magnetic fields in heavy ion collisions: flow and charge transport. *Eur. Phys. J. C*, 80(3):293, 2020.

[91] Kenji Fukushima, Dmitri E. Kharzeev, and Harmen J. Warringa. Chiral magnetic effect. *Phys. Rev. D*, 78:074033, Oct 2008.

[92] Dmitri E. Kharzeev and Ho-Ung Yee. Chiral magnetic wave. *Phys. Rev. D*, 83:085007, Apr 2011.

[93] Sergei A. Voloshin. Parity violation in hot QCD: How to detect it. *Phys. Rev. C*, 70:057901, 2004.

[94] B. I. Abelev et al. Observation of charge-dependent azimuthal correlations and possible local strong parity violation in heavy ion collisions. *Phys. Rev. C*, 81:054908, 2010.

[95] B. I. Abelev et al. Azimuthal Charged-Particle Correlations and Possible Local Strong Parity Violation. *Phys. Rev. Lett.*, 103:251601, 2009.

[96] Jaroslav Adam et al. Charge-dependent flow and the search for the chiral magnetic wave in Pb-Pb collisions at $\sqrt{s_{\rm NN}} = 2.76$ TeV. *Phys. Rev. C*, 93(4):044903, 2016.

[97] Jie Zhao and Fuqiang Wang. Experimental searches for the chiral magnetic effect in heavy-ion collisions. *Progress in Particle and Nuclear Physics*, 107:200–236, 2019.

[98] M. S. Abdallah et al. Search for the chiral magnetic effect with isobar collisions at $\sqrt{s_{NN}} = 200$ gev by the star collaboration at the bnl relativistic heavy ion collider. *Phys. Rev. C*, 105:014901, Jan 2022.

[99] Yuji Hirono, Masaru Hongo, and Tetsufumi Hirano. Estimation of electric conductivity of the quark gluon plasma via asymmetric heavy-ion collisions. *Phys. Rev. C*, 90(2):021903, 2014.

[100] Kouki Nakamura, Takahiro Miyoshi, Chiho Nonaka, and Hiroyuki R. Takahashi. Relativistic resistive magneto-hydrodynamics code for high-energy heavy-ion collisions. arXiv: 2211.02310 [nucl-th].

[101] M. Haddadi Moghaddam, W. M. Alberico, Duan She, A. F. Kord, and B. Azadegan. Accelerating longitudinal expansion of resistive relativistic magnetohydrodynamics in heavy ion collisions. *Phys. Rev. D*, 102:014017, Jul 2020.

[102] Kouki Nakamura, Takahiro Miyoshi, Chiho Nonaka, and Hiroyuki R. Takahashi. Directed flow in relativistic resistive magneto-hydrodynamic expansion for symmetric and asymmetric collision systems. *Phys. Rev. C*, 107(1):014901, 2023.

[103] Yukinao Akamatsu, Hideki Hamagaki, Tetsuo Hatsuda, and Tetsufumi Hirano. Low-mass dilepton production through transport process in quark-gluon plasma. *Phys. Rev. C*, 85:054903, 2012.

[104] Zeyan Wang, Jiaxing Zhao, Carsten Greiner, Zhe Xu, and Pengfei Zhuang. Incomplete electromagnetic response of hot qcd matter. *Phys. Rev. C*, 105:L041901, Apr 2022.

[105] Kouki Nakamura, Takahiro Miyoshi, Chiho Nonaka, and Hiroyuki R. Takahashi. Charge-dependent anisotropic flow in high-energy heavy-ion collisions from relativistic resistive magneto-hydrodynamic expansion. arXiv: 2212.02124 [nucl-th].

[106] Kenneth Aamodt et al. Centrality dependence of the charged-particle multiplicity density at mid-rapidity in Pb-Pb collisions at $\sqrt{s_{NN}} = 2.76$ TeV. *Phys. Rev. Lett.*, 106:032301, 2011.

[107] A. Adare et al. Measurements of Higher-Order Flow Harmonics in Au+Au Collisions at $\sqrt{s_{NN}} = 200$ GeV. *Phys. Rev. Lett.*, 107:252301, 2011.

[108] Paul Sorensen. Higher Flow Harmonics in Heavy Ion Collisions from STAR. *J. Phys. G*, 38:124029, 2011.

[109] K. Aamodt et al. Higher harmonic anisotropic flow measurements of charged particles in Pb-Pb collisions at $\sqrt{s_{NN}}$=2.76 TeV. *Phys. Rev. Lett.*, 107:032301, 2011.

[110] Georges Aad et al. Measurement of the azimuthal anisotropy for charged particle production in $\sqrt{s_{NN}} = 2.76$ TeV lead-lead collisions with the ATLAS detector. *Phys. Rev. C*, 86:014907, 2012.

[111] Serguei Chatrchyan et al. Measurement of Higher-Order Harmonic Azimuthal Anisotropy in PbPb Collisions at $\sqrt{s_{NN}} = 2.76$ TeV. *Phys. Rev. C*, 89(4):044906, 2014.

[112] John Adams et al. Particle type dependence of azimuthal anisotropy and nuclear modification of particle production in Au + Au collisions at s(NN)**(1/2) = 200-GeV. *Phys. Rev. Lett.*, 92:052302, 2004.

[113] J. Adams et al. Azimuthal anisotropy in Au+Au collisions at s(NN)**(1/2) = 200-GeV. *Phys. Rev. C*, 72:014904, 2005.

[114] P. F. Kolb, P. Huovinen, Ulrich W. Heinz, and H. Heiselberg. Elliptic flow at SPS and RHIC: From kinetic transport to hydrodynamics. *Phys. Lett. B*, 500:232–240, 2001.

[115] P. Huovinen, P. F. Kolb, Ulrich W. Heinz, P. V. Ruuskanen, and S. A. Voloshin. Radial and elliptic flow at RHIC: Further predictions. *Phys. Lett. B*, 503:58–64, 2001.

[116] D. Teaney, J. Lauret, and Edward V. Shuryak. Flow at the SPS and RHIC as a quark gluon plasma signature. *Phys. Rev. Lett.*, 86:4783–4786, 2001.

[117] Tetsufumi Hirano. Is early thermalization achieved only near mid-rapidity at RHIC? *Phys. Rev. C*, 65:011901, 2002.

[118] Tetsufumi Hirano, Ulrich W. Heinz, Dmitri Kharzeev, Roy Lacey, and Yasushi Nara. Hadronic dissipative effects on elliptic flow in ultrarelativistic heavy-ion collisions. *Phys. Lett. B*, 636:299–304, 2006.

[119] Chiho Nonaka and Steffen A. Bass. Space-time evolution of bulk QCD matter. *Phys. Rev. C*, 75:014902, 2007.

[120] Hannu Holopainen, Harri Niemi, and Kari J. Eskola. Event-by-event hydrodynamics and elliptic flow from fluctuating initial state. *Phys. Rev. C*, 83:034901, 2011.

[121] Bjoern Schenke, Sangyong Jeon, and Charles Gale. (3+1)D hydrodynamic simulation of relativistic heavy-ion collisions. *Phys. Rev. C*, 82:014903, 2010.

[122] B. B. Back et al. Energy dependence of directed flow over a wide range of pseudorapidity in Au + Au collisions at the bnl relativistic heavy ion collider. *Phys. Rev. Lett.*, 97:012301, Jul 2006.

[123] J. Adams et al. Directed flow in au+au collisions at $\sqrt{s_{NN}} = 62.4$ gev. *Phys. Rev. C*, 73:034903, Mar 2006.

[124] B. I. Abelev et al. System-size independence of directed flow measured at the bnl relativistic heavy-ion collider. *Phys. Rev. Lett.*, 101:252301, Dec 2008.

[125] V. Voronyuk, V. D. Toneev, S. A. Voloshin, and W. Cassing. Charge-dependent directed flow in asymmetric nuclear collisions. *Phys. Rev. C*, 90:064903, Dec 2014.

[126] Sergei A. Voloshin and Takafumi Niida. Ultrarelativistic nuclear collisions: Direction of spectator flow. *Phys. Rev. C*, 94:021901, Aug 2016.

[127] L. Adamczyk and et al. Azimuthal anisotropy in cu+au collisions at $\sqrt{s_{NN}} = 200$ gev. *Phys. Rev. C*, 98:014915, Jul 2018.

[128] A. Adare et al. Measurements of directed, elliptic, and triangular flow in cu + au collisions at $\sqrt{s_{NN}} = 200$ gev. *Phys. Rev. C*, 94:054910, Nov 2016.

[129] L. Adamczyk et al. Charge-dependent directed flow in Cu + Au collisions at $\sqrt{s_{NN}} = 200$ GeV. *Phys. Rev. Lett.*, 118:012301, Jan 2017.

[130] P.F Kolb, P Huovinen, U Heinz, and H Heiselberg. Elliptic flow at sps and rhic: from kinetic transport to hydrodynamics. *Physics Letters B*, 500(3):232–240, 2001.

[131] D. Teaney, J. Lauret, and E. V. Shuryak. Flow at the sps and rhic as a quark-gluon plasma signature. *Phys. Rev. Lett.*, 86:4783–4786, May 2001.

[132] Tetsufumi Hirano. Is early thermalization achieved only near midrapidity in au + au collisions at $\sqrt{s_{\rm NN}} = 130$GeV?. *Phys. Rev. C*, 65:011901, Dec 2001.

[133] R. J. Glauber and G. Matthiae. High-energy scattering of protons by nuclei. *Nucl. Phys. B*, 21:135–157, 1970.

[134] A. Bialas, M. Bleszynski, and W. Czyz. Multiplicity Distributions in Nucleus-Nucleus Collisions at High-Energies. *Nucl. Phys. B*, 111:461–476, 1976.

[135] Larry D. McLerran and Raju Venugopalan. Green's functions in the color field of a large nucleus. *Phys. Rev. D*, 50:2225–2233, 1994.

[136] Larry D. McLerran and Raju Venugopalan. Gluon distribution functions for very large nuclei at small transverse momentum. *Phys. Rev. D*, 49:3352–3355, 1994.

[137] Larry D. McLerran and Raju Venugopalan. Computing quark and gluon distribution functions for very large nuclei. *Phys. Rev. D*, 49:2233–2241, 1994.

[138] Long-Gang Pang, Gergely Endrődi, and Hannah Petersen. Magnetic-field-induced squeezing effect at energies available at the BNL Relativistic Heavy Ion Collider and at the CERN Large Hadron Collider. *Phys. Rev. C*, 93(4):044919, 2016.

[139] Fred Cooper and Graham Frye. Comment on the Single Particle Distribution in the Hydrodynamic and Statistical Thermodynamic Models of Multiparticle Production. *Phys. Rev. D*, 10:186, 1974.

[140] L. A. Winckelmann et al. Microscopic calculations of stopping and flow from 160-A/MeV to 160-A/GeV. *Nucl. Phys. A*, 610:116C–123C, 1996.

[141] S. A. Bass et al. Microscopic models for ultrarelativistic heavy ion collisions. *Prog. Part. Nucl. Phys.*, 41:255–369, 1998.

[142] M. Bleicher et al. Relativistic hadron hadron collisions in the ultrarelativistic quantum molecular dynamics model. *J. Phys. G*, 25:1859–1896, 1999.

[143] Y. Nara, N. Otuka, A. Ohnishi, K. Niita, and S. Chiba. Study of relativistic nuclear collisions at AGS energies from p + Be to Au + Au with hadronic cascade model. *Phys. Rev. C*, 61:024901, 2000.

[144] M. Isse, A. Ohnishi, N. Otuka, P. K. Sahu, and Y. Nara. Mean-field effects on collective flows in high-energy heavy-ion collisions from AGS to SPS energies. *Phys. Rev. C*, 72:064908, 2005.

[145] J. Weil et al. Particle production and equilibrium properties within a new hadron transport approach for heavy-ion collisions. *Phys. Rev. C*, 94(5):054905, 2016.

[146] Anna Schäfer, Iurii Karpenko, Xiang-Yu Wu, Jan Hammelmann, and Hannah Elfner. Particle production in a hybrid approach for a beam energy scan of Au+Au/Pb+Pb collisions between $\sqrt{s_{\rm NN}} = 4.3$ GeV and $\sqrt{s_{\rm NN}} = 200.0$ GeV. 12 2021.

[147] Peter Brockway Arnold. Quark-Gluon Plasmas and Thermalization. *Int. J. Mod. Phys. E*, 16:2555–2594, 2007.

[148] F. Gelis. Color Glass Condensate and Glasma. *Int. J. Mod. Phys. A*, 28:1330001, 2013.

[149] Xu-Guang Huang and Jinfeng Liao. Kinetic evolution of the glasma and thermalization in heavy ion collisions. *Int. J. Mod. Phys. E*, 23:1430003, 2014.

[150] Jurgen Berges. Nonequilibrium Quantum Fields: From Cold Atoms to Cosmology. 3 2015.

[151] Sourendu Gupta. The electrical conductivity and soft photon emissivity of the qcd plasma. *Physics Letters B*, 597(1):57–62, 2004.

[152] Gert Aarts, Chris Allton, Justin Foley, Simon Hands, and Seyong Kim. Spectral functions at small energies and the electrical conductivity in hot, quenched lattice QCD. *Phys. Rev. Lett.*, 99:022002, 2007.

[153] H. T. Ding, A. Francis, O. Kaczmarek, F. Karsch, E. Laermann, and W. Soeldner. Thermal dilepton rate and electrical conductivity: An analysis of vector current correlation functions in quenched lattice QCD. *Phys. Rev. D*, 83:034504, 2011.

[154] A. Francis and O. Kaczmarek. On the temperature dependence of the electrical conductivity in hot quenched lattice qcd. *Progress in Particle and Nuclear Physics*, 67(2):212–217, 2012. From Quarks and Gluons to Hadrons and Nuclei.

[155] Heng-Tong Ding, Olaf Kaczmarek, and Florian Meyer. Vector spectral functions and transport properties in quenched QCD. *PoS*, LATTICE2014:216, 2015.

[156] Bastian B. Brandt, Anthony Francis, Harvey B. Meyer, and Hartmut Wittig. Thermal Correlators in the \rho\ channel of two-flavor QCD. *JHEP*, 03:100, 2013.

[157] Alessandro Amato, Gert Aarts, Chris Allton, Pietro Giudice, Simon Hands, and Jon-Ivar Skullerud. Electrical conductivity of the quark-gluon plasma across the deconfinement transition. *Phys. Rev. Lett.*, 111:172001, Oct 2013.

[158] Gert Aarts, Chris Allton, Alessandro Amato, Pietro Giudice, Simon Hands, and Jon-Ivar Skullerud. Electrical conductivity and charge diffusion in thermal QCD from the lattice. *JHEP*, 02:186, 2015.

[159] Kirill Tuchin. Particle production in strong electromagnetic fields in relativistic heavy-ion collisions. *Adv. High Energy Phys.*, 2013:490495, 2013.

[160] Kirill Tuchin. Electromagnetic field and the chiral magnetic effect in the quark-gluon plasma. *Phys. Rev. C*, 91:064902, Jun 2015.

[161] Kirill Tuchin. Electromagnetic fields in high energy heavy-ion collisions. *International Journal of Modern Physics E*, 23(01):1430001, 2014.

[162] B.G. Zakharov. Electromagnetic response of quark–gluon plasma in heavy-ion collisions. *Physics Letters B*, 737:262–266, 2014.

[163] Jean-Yves Ollitrault. Relativistic hydrodynamics for heavy-ion collisions. *European Journal of Physics*, 29(2):275, jan 2008.

[164] L. Ladau and E. Lifschitz. *Fluid Mechanics*. Pergamon Press, New York, 1959.

[165] Carl Eckart. The thermodynamics of irreversible processes. i. the simple fluid. *Phys. Rev.*, 58:267–269, Aug 1940.

[166] I.G Bearden et al. Charged particle densities from au+au collisions at snn=130 gev. *Physics Letters B*, 523(3):227–233, 2001.

[167] I. G. Bearden et al. Pseudorapidity distributions of charged particles from Au + Au collisions at the maximum rhic energy, $\sqrt{s_{NN}} = 200$GeV. *Phys. Rev. Lett.*, 88:202301, May 2002.

[168] B. B. Back et al. Significance of the fragmentation region in ultrarelativistic heavy-ion collisions. *Phys. Rev. Lett.*, 91:052303, Aug 2003.

[169] B. Alver et al. Charged-particle multiplicity and pseudorapidity distributions measured with the phobos detector in Au + Au, Cu + Cu, $\mathbf{d}$ + Au, and $\mathbf{p} + \mathbf{p}$ collisions at ultrarelativistic energies. *Phys. Rev. C*, 83:024913, Feb 2011.

[170] Serguei Chatrchyan et al. Dependence on pseudorapidity and centrality of charged hadron production in PbPb collisions at a nucleon-nucleon centre-of-mass energy of 2.76 TeV. *JHEP*, 08:141, 2011.

[171] G. Aad et al. Measurement of the centrality dependence of the charged particle pseudorapidity distribution in lead–lead collisions at snn=2.76 tev with the atlas detector. *Physics Letters B*, 710(3):363–382, 2012.

[172] E. Abbas et al. Centrality dependence of the pseudorapidity density distribution for charged particles in pb–pb collisions at snn=2.76 tev. *Physics Letters B*, 726(4):610–622, 2013.

[173] J. D. Bjorken. Highly relativistic nucleus-nucleus collisions: The central rapidity region. *Phys. Rev. D*, 27:140–151, Jan 1983.

[174] Eric G. Blackman and George B. Field. Ohm's law for a relativistic pair plasma. *Phys. Rev. Lett.*, 71:3481–3484, 1993.

[175] Victor Roy, Shi Pu, Luciano Rezzolla, and Dirk Rischke. Analytic bjorken flow in one-dimensional relativistic magnetohydrodynamics. *Physics Letters B*, 750:45–52, 2015.

[176] Piotr Bożek. Viscous evolution of the rapidity distribution of matter created in relativistic heavy-ion collisions. *Phys. Rev. C*, 77:034911, Mar 2008.

[177] C.-D. Munz, P. Omnes, R. Schneider, E. Sonnendrücker, and U. Voß. Divergence correction techniques for maxwell solvers based on a hyperbolic model. *Journal of Computational Physics*, 161(2):484–511, 2000.

[178] S. S. Komissarov. Multi-dimensional Numerical Scheme for Resistive Relativistic MHD. *Mon. Not. Roy. Astron. Soc.*, 382:995, 2007.

[179] Oliver Porth, Hector Olivares, Yosuke Mizuno, Ziri Younsi, Luciano Rezzolla, Monika Moscibrodzka, Heino Falcke, and Michael Kramer. The Black Hole Accretion Code. 11 2016.

[180] Bram Van Leer. Towards the ultimate conservative difference scheme. iv. a new approach to numerical convection. *Journal of Computational Physics*, 23(3):276–299, 1977.

[181] Amiram Harten, Peter D. Lax, and Bram van Leer. On upstream differencing and godunov-type schemes for hyperbolic conservation laws. *SIAM Review*, 25(1):35–61, 1983.

[182] Yukinao Akamatsu, Shu ichiro Inutsuka, Chiho Nonaka, and Makoto Takamoto. A new scheme of causal viscous hydrodynamics for relativistic heavy-ion collisions: A riemann solver for quark–gluon plasma. *Journal of Computational Physics*, 256:34–54, 2014.

[183] Chi-Wang Shu and Stanley Osher. Efficient implementation of essentially non-oscillatory shock-capturing schemes. *Journal of Computational Physics*, 77(2):439–471, 1988.

[184] Carlos Palenzuela, Luis Lehner, Oscar Reula, and Luciano Rezzolla. Beyond ideal MHD: towards a more realistic modelling of relativistic astrophysical plasmas. *Monthly Notices of the Royal Astronomical Society*, 394(4):1727–1740, 04 2009.

[185] BRUNO GIACOMAZZO and LUCIANO REZZOLLA. The exact solution of the riemann problem in relativistic magnetohydrodynamics. *Journal of Fluid Mechanics*, 562:223–259, 2006.

[186] Makoto Takamoto and Tsuyoshi Inoue. A NEW NUMERICAL SCHEME FOR RESISTIVE RELATIVISTIC MAGNETOHYDRODYNAMICS USING METHOD OF CHARACTERISTICS. *The Astrophysical Journal*, 735(2):113, jun 2011.

[187] Michael Dumbser and Olindo Zanotti. Very high order pnpm schemes on unstructured meshes for the resistive relativistic mhd equations. *Journal of Computational Physics*, 228(18):6991–7006, 2009.

[188] N. Bucciantini and L. Del Zanna. A fully covariant mean-field dynamo closure for numerical 3 + 1 resistive GRMHD. *Monthly Notices of the Royal Astronomical Society*, 428(1):71–85, 10 2012.

[189] S Miranda-Aranguren, M A Aloy, and T Rembiasz. An HLLC Riemann solver for resistive relativistic magnetohydrodynamics. *Monthly Notices of the Royal Astronomical Society*, 476(3):3837–3860, 02 2018.

[190] R. J. Glauber. Lecture on Theoritical Physics. *(WE Brittin and LG Dunham, New York, 1959)*.

[191] Piotr Bozek and Iwona Wyskiel. Directed flow in ultrarelativistic heavy-ion collisions. *Phys. Rev. C*, 81:054902, 2010.

[192] Piotr Bożek and Iwona Wyskiel. Directed flow in ultrarelativistic heavy-ion collisions. *Phys. Rev. C*, 81:054902, May 2010.

[193] Seiji Zenitani, Michael Hesse, Alex Klimas, and Masha Kuznetsova. New measure of the dissipation region in collisionless magnetic reconnection. *Phys. Rev. Lett.*, 106:195003, May 2011.

[194] Umut Gürsoy, Dmitri Kharzeev, and Krishna Rajagopal. Magnetohydrodynamics, charged currents, and directed flow in heavy ion collisions. *Phys. Rev. C*, 89:054905, May 2014.

[195] Yifeng Sun, Salvatore Plumari, and Vincenzo Greco. Probing the electromagnetic fields in ultrarelativistic collisions with leptons from z0 decay and charmed mesons. *Physics Letters B*, 816:136271, 2021.

[196] Ze-Fang Jiang, Shanshan Cao, Wen-Jing Xing, Xiang-Yu Wu, C. B. Yang, and Ben-Wei Zhang. Probing the initial longitudinal density profile and electromagnetic field in ultrarelativistic heavy-ion collisions with heavy quarks. *Phys. Rev. C*, 105:054907, May 2022.

[197] Piotr Bożek. Event-by-event viscous hydrodynamics for cu–au collisions at snn=200 gev. *Physics Letters B*, 717(1):287–290, 2012.

[198] Piotr Bożek. Event-by-event viscous hydrodynamics for Cu–Au collisions at $\sqrt{s_{NN}}$=200 GeV. *Phys. Lett. B*, 717:287–290, 2012.

[199] L. Adamczyk et al. Beam-energy dependence of the directed flow of protons, antiprotons, and pions in au+au collisions. *Phys. Rev. Lett.*, 112:162301, Apr 2014.

[200] Hans-Joachim Drescher and Yasushi Nara. Eccentricity fluctuations from the color glass condensate in ultrarelativistic heavy ion collisions. *Phys. Rev. C*, 76:041903, Oct 2007.

[201] Hans-Joachim Drescher and Yasushi Nara. Effects of fluctuations on the initial eccentricity from the color glass condensate in heavy ion collisions. *Phys. Rev. C*, 75:034905, Mar 2007.

[202] Azumi Sakai, Koichi Murase, and Tetsufumi Hirano. Rapidity decorrelation of anisotropic flow caused by hydrodynamic fluctuations. *Phys. Rev. C*, 102:064903, Dec 2020.

[203] Azumi Sakai, Koichi Murase, and Tetsufumi Hirano. Effects of hydrodynamic and initial longitudinal fluctuations on rapidity decorrelation of collective flow. *Physics Letters B*, 829:137053, 2022.

[204] Gabriel S. Denicol, Xu-Guang Huang, Etele Molnár, Gustavo M. Monteiro, Harri Niemi, Jorge Noronha, Dirk H. Rischke, and Qun Wang. Nonresistive dissipative magnetohydrodynamics from the boltzmann equation in the 14-moment approximation. *Phys. Rev. D*, 98:076009, Oct 2018.

[205] Gabriel S. Denicol, Etele Molnár, Harri Niemi, and Dirk H. Rischke. Resistive dissipative magnetohydrodynamics from the boltzmann-vlasov equation. *Phys. Rev. D*, 99:056017, Mar 2019.

[206] Ashutosh Dash, Masoud Shokri, Luciano Rezzolla, and Dirk H. Rischke. Charge diffusion in relativistic resistive second-order dissipative magnetohydrodynamics. 11 2022.

[207] L. Adamczyk et al. Global Λ hyperon polarization in nuclear collisions: evidence for the most vortical fluid. *Nature*, 548:62–65, 2017.

[208] Gabriel S. Denicol, Charles Gale, Sangyong Jeon, Akihiko Monnai, Björn Schenke, and Chun Shen. Net baryon diffusion in fluid dynamic simulations of relativistic heavy-ion collisions. *Phys. Rev. C*, 98(3):034916, 2018.

[209] Chiho Nonaka and Masayuki Asakawa. Hydrodynamical evolution near the qcd critical end point. *Phys. Rev. C*, 71:044904, Apr 2005.

[210] Akihiko Monnai, Björn Schenke, and Chun Shen. Qcd equation of state at finite chemical potentials for relativistic nuclear collisions. *International Journal of Modern Physics A*, 36(07):2130007, 2021.

[211] Akihiko Monnai, Björn Schenke, and Chun Shen. Equation of state at finite densities for qcd matter in nuclear collisions. *Phys. Rev. C*, 100:024907, Aug 2019.

[212] Brett McInnes. A rotation/magnetism analogy for the quark–gluon plasma. *Nuclear Physics B*, 911:173–190, 2016.

[213] Yannis Burnier, Dmitri E. Kharzeev, Jinfeng Liao, and Ho-Ung Yee. Chiral magnetic wave at finite baryon density and the electric quadrupole moment of the quark-gluon plasma. *Phys. Rev. Lett.*, 107:052303, Jul 2011.

[214] Irfan Siddique, Shanshan Cao, Uzma Tabassam, Mohsin Saeed, and Muhammad Waqas. Electromagnetic anomaly in the presence of electric and chiral magnetic conductivities in relativistic heavy-ion collisions. *Phys. Rev. C*, 105:054909, May 2022.